Magnetic Resonance Velocimetry for Unsteady Flows

Vom Fachbereich Maschinenbau
an der Technischen Universität Darmstadt
zur
Erlangung des Grades eines Doktor-Ingenieurs (Dr.-Ing.)
genehmigte

Dissertation

vorgelegt von

Daniel Kim Freudenhammer, M.Sc.

aus Rosbach v.d.H.

Berichterstatter:	Prof. Dr.-Ing. Cameron Tropea
Mitberichterstatter:	Prof. Dr. Dr. h.c. Jürgen Hennig
Tag der Einreichung:	02. August 2016
Tag der mündlichen Prüfung:	16. November 2016

Darmstadt 2017

D 17

Erklärung

Hiermit erkläre ich, Daniel Kim Freudenhammer, dass ich die vorliegende Dissertation, abgesehen von den in ihr genannten Hilfen, selbstständig verfasst habe.

Darmstadt, 02. August 2016 Daniel Kim Freudenhammer

Abstract

Magnetic Resonance Imaging (MRI) is an established tool for clinical diagnostics. The measurement technique can be used to measure blood flow, then denoted *Flow MRI* or *Magnetic Resonance Velocimetry* (MRV). MRV has in recent years also found increasing consideration in the field of fluid mechanics, where it is esteemed for its unique capabilities of measuring fully volumetric velocity fields without the need for optical access and without manipulating the flow under investigation. MRV is typically used for the acquisition of mean velocity fields in water flows. This study deals with the possibility of acquiring velocity fields in steady, unsteady and turbulent flows. Besides the application of the different MR techniques in selected test cases, validation of the acquired measurement data is a main topic of this thesis.

Mean flow measurements are acquired within steady flow model of a modern IC engine. The acquired flow data is validated by means of PIV data and excellent agreement is found. The three-dimensional nature of the acquired flow field enables new insights into the volumetric flow field distribution. Unsteady periodic flows are analyzed by means of the *4D MRV* measurement sequence, which acquires phase-averaged, volumetric velocity fields. The acquired flow data is extensively validated by means of *Particle Image Velocimetry* (PIV) and *Laser Doppler Velocimetry* (LDV) data and valid flow regions are identified. A comprehensive understanding of the unsteady, periodic flow field evolution during intake stroke is enabled for the measurements inside the modified engine flow model. *MR turbulence* measurements, for the acquisition of normal and shear stresses within the flow field, are conducted within a Backward Facing Step (BFS) geometry, which provides optical access for comparative LDV validation measurements through a perspex insert. MR turbulence measurements inside the engine flow model demonstrate the potential of the measurements regarding their application in complex geometries. Validation of the measurements shows a reasonable agreement for normal stresses, while the determination of shear stresses remains still rather inaccurate.

Zusammenfassung

Magnetresonanztomographie (MRT, englisch MRI) ist eine bewährte Messtechnik im Bereich der klinischen Diagnose. MRI ermöglicht das Vermessen von Geschwindigkeitsfeldern, dann *Flow MRI* bzw. *Magnetic Resonance Velocimetry* (MRV) genannt. MRV findet zunehmend Anwendung im Bereich der Strömungsmechanik, wo es aufgrund seiner Besonderheit geschätzt wird: Die Ermittlung dreidimensionaler Geschwindigkeitsfelder ohne Strömungsbeeinflussung und ohne Notwendigkeit eines optischen Zugangs.

Gegenstand dieser Arbeit ist die Anwendung von MRV in stationären sowie in instationären periodischen Strömungen. Außerdem soll MRV zur Quantifizierung turbulenter Strömungen dienen. Zu diesem Zweck werden unterschiedliche MRV Sequenzen verwendet und in ausgewählten Strömungsgeometrien appliziert. Die Validierung dieser Sequenzen steht dabei im Vordergrund und wird durch Validationsmessungen mittels etablierter Messtechnik realisiert.

Stationäre Messungen werden in einem Modell eines Viertakt Ottomotors durchgeführt. Die Validierung mittels *Particle Image Velocimetry* (PIV) Messungen ergibt eine sehr gute Übereinstimmung beider Messtechniken. Die ermittelten dreidimensionalen Strömungsfelder bieten neue Möglichkeiten der Strömungsanalyse. Für ein tiefgreifendes Verständnis instationärer periodischer Strömungendes, können Diese mit Hilfe von *4D MRV Messungen* aufgenommen werden. Die Messdaten werden mit optischer Messtechnik (PIV und LDV) validiert. Bereiche guter Übereinstimmung werden identifiziert, auftretende Differenzen erläutert. Die Ermittlung von Komponenten des Reynoldsschen Spannungstensors in turbulenten Strömungen wird durch *MR Turbulenzmessungen* ermöglicht. Diese Messungen werden in zwei unterschiedlichen Strömungsmodellen präsentiert. Die Validierung dieser Messungen ergibt eine recht gute Übereinstimmung in der Bestimmung der Normalspannungskomponenten, während die Bestimmung von Schubspannungen noch fehlerbehaftet ist. Potentielle Fehlerquellen werden diskutiert.

Danksagung

Zunächst möchte ich mich bei Prof. Dr.-Ing. Sven Grundmann bedanken. Er infizierte mich mit seiner Begeisterung für die Magnetic Resonance Velocimetry und ihm habe ich die Chance zur Anfertigung einer Promotion ganz wesentlich zu verdanken. Viele Ideen für die Inhalte dieser Arbeit entwickelten sich zudem innerhalb einer der zahlreichen fachlichen Diskussionen, bei welchen der Spaß auch nie zu kurz kam. Danke Sven.
Ganz herzlich bedanken möchte ich mich bei Prof. Dr.-Ing. Cameron Tropea, der mir die Promotion am Fachgebiet Strömungslehre und Aerodynamik an der Technischen Universität Darmstadt ermöglicht hat. Wichtige Anliegen konnten oftmals auf kurzem Dienstweg bei gemeinsamen Waldläufen besprochen werden, dafür bin ich sehr dankbar. Bei Prof. Dr. Dr. h.c. Jürgen Hennig, Wissenschaftlicher Direktor am Universitätsklinikum Freiburg, möchte ich mich vielmals für die Übernahme des Koreferats dieser Arbeit bedanken.
Die unzähligen gemeinsamen Messfahrten nach Freiburg mit Dr. Martin Bruschewski und Dr. Florian Wassermann waren teilweise nervenaufreibend, meist erfolgreich aber stets sehr unterhaltsam. Die vielen gemeinsamen Stunden werden mir in guter Erinnerung bleiben - Danke Jungs! Auch bei meinen Freiburger Kollegen, Dr. Waltraud Buchenberg und Dr. Robin Simpson möchte ich mich für die Unterstützung und die vielen gemeinsamen Stunden “unter Erde” am Tomographen bedanken.
Die ausgezeichneten Stimmung am Windkanal in Griesheim ist auf die dortigen Arbeitskollegen zurückzuführen. Dazu zählen/zählten Andreas Bauer, Alex Beck, Jan Breitenbach, Dr. Ulrike Cordes, Johannes Feldmann, Maximilian Kuhnhenn, Dr. Armin Kurz, Dr. Imdat Maden, Timotheus Nemitz, Dr. Lars Opfer, Dr. Andreas Reeh, Klaus Schiffmann, Patrick Seiler, Bernhard Simon, Fabian Tenzer und Dr. Alexander Widmann. Regelmäßige gemeinsame Kochaktionen und Heiterkeiten diverser Art führten zu einem exzellenten Arbeitsklima und halfen so den Arbeitsalltag gut zu meistern.

Ein riesiges Dankeschön gilt der Mechanischen Werkstatt um Ilona Kaufhold und ihren Jungs Tim Geelhaar, Joachim Heyl, Manolo Vaca Schwinkendorf und Florian Vogt. Ohne eure Expertise und euren Einsatz wäre diese Arbeit nicht möglich gewesen. Ich weiß die viele Mühe für die Umsetzung meiner Ideen, teilweise auch mit sehr wenig Vorlaufzeit, sehr zu schätzen. Auch Martin Weiß von der Elektronik-Werkstatt möchte ich für wertvolle Ratschläge danken.
Der größte Dank gilt meinen Eltern und meiner gesamten Familie, die mich auf diesem Weg begleitet haben und deren voller Unterstützung ich mir stets gewiss sein konnte.

Contents

1 Introduction

1.1 Motivation

In experimental fluid mechanics a multitude of techniques are available for measuring flow velocity. These techniques are generally classified according to the number of velocity components which are acquired and over how many dimensions the measurement is made. Understandably a strong demand exists to acquire all three velocity components (in a Cartesian system, u, v and w) over three, or with temporal resolution, four dimensions (x, y, z and t). Few techniques offer this possibility and those that do, such as time-resolved tomographic TR-PIV, are complex and require inordinate post-processing times. Therefore, the recent development of *Magnetic Resonance Velocimetry* (MRV) is a welcome addition to the repertory of available techniques, offering not only a three-dimensional, three-component (3D3C) capability, but also exhibiting further advantages over conventional techniques. These include non-invasiveness, no requirement for optical access, and minimal post-processing effort. The present state-of-the-art of MRV technology does not permit time-resolved measurements of the flow; hence the study of unsteady flows is only possible under restricted conditions and involving dedicated equipment. It is the objective of this work, partly already published or presented [30–34], to explore to what extent such flows can be studied using MRV.

Magnetic Resonance Imaging (MRI) has been a well-established diagnostic tool in clinical studies since the 1980's and first use of this technique to measure local flow velocity involved the visualization of blood flow in patients with the purpose of identifying potential diseases or abnormalities. More recently, existing clinical scanners have been used to also study engineering flow geometries. This necessitates special considerations, since the magnetic fields involved are strong and any ferrous metals in the system lead to significant distortion of the magnetic field and falsification of the measurement.

Thus the flow systems must be compatible with the magnetic environment. Furthermore, MRV, relying on proton spins, requires a certain atomic structure of the flow medium and most commonly water is used; hence Reynolds number scaling also becomes an issue, together with the dimensions of the scanner, leading to constraints on the geometry and size of the flow system. Undoubtedly the advent of rapid prototyping, such as direct laser sintering, is one explanation why MRV has only recently been more widely used for engineering flow applications. Also these aspects must been considered when attempting to extend the technique to unsteady flows.

Having resolved the above-mentioned issues, the question of measurement accuracy and precision still remains, especially in the case of unsteady flows. Although instantaneous snapshots of the flowfield can be acquired in principle, the variability of such a measurement is unacceptably large; hence, the extension of MRV to unsteady flows involves either phase-averaged or ensemble averaged statistics. This leads directly to the question of obtainable accuracy - a central point addressed in this thesis.

1.2 Objectives and outline of the thesis

The present thesis is intended to provide a contribution towards the application of MR measurement techniques in both steady and unsteady engineering flow geometries. For this purpose, three different MR acquisition techniques, denoted *MR sequences*, are reviewed and applied in selected test cases. The acquired measurement data is qualitatively and quantitatively validated by means of other data sets. These are produced with the help of conventional measurement techniques, namely *Laser Doppler Velocimetry* (LDV) and *Particle Image Velocimetry* (PIV). Existing deviations between the MR and the validation data sets are discussed and, where possible, physically explained. It is emphasized, that the development and the improvement of the MR sequences is not the subject of this thesis, but have been developed at the Department of Radiology, Medical Physics, Medical Center Freiburg under the directorship of Prof. Jürgen Hennig.

The structure of this thesis is organized as follows:

An overview of conventional measurement techniques used in experimental fluid mechanics is provided in *Chapter 2*. The measurements techniques are

reviewed in terms of their suitability for application in steady and unsteady flows. Features of MR measurement techniques are introduced and highlighted against conventional techniques.

The working principle and commonalities of different MR measurement techniques are outlined in *Chapter 3*. The peculiarities of the different MR techniques regarding their intended use are discussed.

Important background information regarding the measurement procedure and the facilities used to conduct the measurements are specified in *Chapter 4*.

The measurement results are presented in three individual chapters, corresponding to the different flows under consideration: steady flows, periodic flows and turbulent flows.

Chapter 5 presents mean flow measurements conducted in a *steady flow* model of a single cylinder direct injection spark ignition (DISI) engine. In particular the flow near the intake valve has been studied. The capabilities of the MR techniques in acquiring volumetric (3D3C) velocity fields are highlighted. The influence of geometrical changes on the volumetric flow field is investigated.

The possibility of analyzing unsteady, *periodic flows* by means of MR techniques is the subject of *Chapter 6*. Phase-averaged MR measurements, denoted *4D MRV*, where the fourth dimension indicates the "temporal resolution", are presented for two test cases, differing in their source of triggering for the phase averaging. The first test case is again the single cylinder engine head, but now with periodic movement of the valves. The second test case is the wake flow behind a cylinder, in which the unsteadiness arises due to the von Kármán vortex street.

In *Chapter 7* a MR technique is presented which enables the measurement of normal and shear stresses in *turbulent flows*. The measurements are performed on two test cases: 1) A Backward Facing Step (BFS) geometry, which also provides optical access for comparative LDV validation measurements; 2) Measurements inside the engine flow model mentioned above, in order to demonstrate the potential of turbulence measurements applied in complex flow geometries.

The thesis concludes with a summary and discussion of the main outcomes in *Chapter 8*.

2 Measurement techniques for steady & unsteady flows

State-of-the-art measurement techniques for the quantification of steady and unsteady flows are presented in this section. Invasive and non-invasive measurement techniques are considered individually. Some important characteristics of the MR measurement techniques are presented, the underlying working principle is subject of Chapter 3.

2.1 Invasive measurement techniques

Invasive techniques for the measurement of flow velocities are widespread, mainly due to their easy application and low costs. Because the sensor is placed inside the flow field, these techniques usually do not need additional equipment such as tracer particles or cameras. The extent of flow manipulation due to the existence of the invasive flow sensor is reduced to a minimum by small geometrical dimensions. A brief overview of standard invasive measurement techniques for technical flows is following.

2.1.1 Calculation from pressure difference

Prandtl tubes allow the measurement of total and static pressure (p_T and p_S, respectively) inside the flow. p_T and p_S can then be used to calculate the dynamic pressure $p_D = p_T - p_S$. A schematic of a Prandtl tube is shown in Fig. 2.1. Various types of pressure transducers exist to quantify the dynamic pressure p_D. In its simplest version, p_S and p_T are connected to both ends of a liquid column manometer which is filled with a liquid of density ρ_l. The emerging difference in liquid height is a direct measure of the pressure difference, which can be calculated to be $p_D = \rho_l \, \vec{g} \cdot (h_s - h_t)$. By using the Bernoulli equation and neglecting the hydrostatic pressure term, the local flow

velocity $\vec{u}$ can be calculated as

$$u = \sqrt{\frac{2\,p_D}{\rho_f}} \tag{2.1}$$

where ρ_f is the temperature-dependent density of the flow, which can be liquid or gaseous. In order to enable accurate velocity-measurements, the temperature of the fluid must therefore be measured, unless it is known and constant.

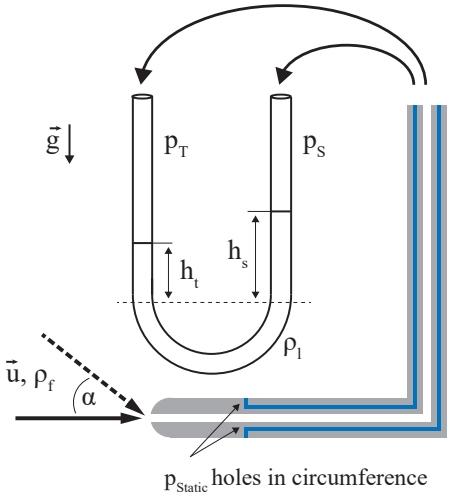

Figure 2.1: Schematic of a Prandtl tube. The total pressure p_T (= stagnation pressure) is measured with a tube that is aligned with the flow. A number of circumferentially arranged holes enable the measurement of the static pressure p_S. Various types of pressure transducers exist to quantify the dynamic pressure p_D, from which the flow velocity $\vec{u}$ can be calculated using Eq. 2.1.

However, regular pressure tubes only allow the quantification of the velocity magnitude, the flow direction can not be determined. Moreover, the calculation of the flow velocity magnitude is only accurate when the pressure tube is precisely aligned with the flow direction. If the angle of attack $\alpha \neq 0$, as

illustrated in Fig. 2.1 the flow measurement will be erroneous, since only the fraction of the incoming flow velocity in main flow direction ($\vec{u}_{\parallel} = \cos\alpha\,\vec{u}$) contributes to the total pressure p_T inside the pressure tube. For this reason Prandtl tubes are predominantly used in flows with small changes in the angle of attack (e.g. for air-speed measurements in airplanes) or in steady flows.

The dependency of the measured total pressure p_T on the angle of attack is exploited with multi-hole probes (MHP), that can be used to overcome the limitation of regular Prandtl tubes and thereby enable the determination of the flow direction. MHP consist of two to five total pressure sensors, depending on the application in 2D or 3D flow conditions, respectively.

Common to all pressure-based flow velocity measurements is a comparatively low temporal resolution, which is mainly caused by inertia of the flow medium in the connecting tubes and, in the case of gaseous fluids, compressibility effects. The temporal resolution generally does not exceed $\approx 100\,\mathrm{Hz}$. For that reason, pressure-based techniques are predominantly used in steady flows and are not well suited for the quantification of turbulence quantities, such as turbulent velocity fluctuations.

2.1.2 Calculation from thermoelectric signals

Hot-wire anemometry (HWA) exploits the pronounced temperature-dependent electrical resistance $R_S = f(T_S)$ of the hot wire. The sensor can have numerous designs and properties, depending on the intended application, and commonly consists of a platinum-plated electric wire made from tungsten with a diameter of $d \approx 2.5 - 5\,\mu\mathrm{m}$ and length $l \approx 1 - 2\,\mathrm{mm}$.

The sensor is heated above the expected temperature of the flow (T_F), i.e. $T_S/T_F \approx 1.5$ (Nitsche and Brunn [65]). A change in the flow velocity $\vec{u}$ results in a change of the sensor temperature T_S, predominantly due to heat convection[1] and, consequently, a change of the electrical resistance R_S.

Using a Constant Temperature Anemometry (CTA) configuration, the sensor temperature T_S can, through adaptation of the bridge voltage U_B, be kept constant. Fig. 2.2 illustrates the CTA configuration, which essentially consists of a wheatstone bridge electric circuit. An increase of the flow velocity u leads to increased heat convection of the sensor and a decline of T_S and R_S. The change in R_S produces error voltage. The bridge voltage U_B is

[1] Heat losses through radiation and conduction are small and usually ignored.

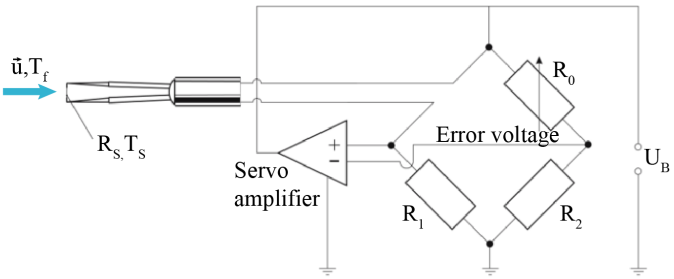

Figure 2.2: Sketch of the HWA working principle in CTA configuration. The wheatstone bridge electric circuit adjusts the bridge voltage U_B such that the sensor temperature T_S remains constant, independent of heat convection changes, caused by velocity fluctuations. (Adapted from Nitsche and Brunn [65]).

adapted, and the resistor R_0 adjusts such that the error voltage disappears and the bridge is again balanced. Provided that the temperature of the flow T_F remains constant throughout the measurement procedure, U_B is thus a measure of the flow velocity $\vec{u}$. The determination of the flow direction is not possible with a single hot-wire; however, this can be achieved with advanced designs (e.g. multiple wire probes). Because of its unique capability of measuring both mean velocity and velocity fluctuations in unsteady flows, HWA has become a standard tool for flow quantification in engineering sciences. A frequency response up to several kilohertz can be obtained in gas flows Bruun [13]. This technique can be applied also in liquid flows. The sensor type (then denoted *hot-film sensor*) has a more robust design and larger dimensions, leading to increased amount of flow intrusion. Moreover, the frequency response is reduced.

2.2 Non-invasive measurement techniques

Optical measurement techniques are used in disturbance sensitive flows or when flow sensors cannot be placed within the measurement section due to geometrical limitations. Instead, the flow is seeded with tracer particles that are chosen with characteristics matching the properties of the working fluid

and ideally following the flow. Optical access into the region of interest is necessary in order to trace the particles.

The tracer particles are homogeneously distributed within the flow and the flow velocity is measured through the signal of the reflected light by two different principles that are presented in the following sections.

2.2.1 Laser Doppler Velocimetry

Laser Doppler Velocimetry (LDV) is a pointwise measurement technique, i.e. it is possible but very time-consuming to acquire data inside an entire 2D- or 3D-volume point by point. Using the traverse system, convenient and accurate measurements at distinct points are possible and allow the acquisition with high spatial and temporal resolution. LDV is wide spread due to its versatility and its convenient and robust application. The working principle of LDV is based on a frequency shift which appears twice:

- when light with frequency f_l emitted by a stationary laser is received by a moving tracer particle inside the flow f_p
- when light emitted by the moving tracer particle (f_p) is registered by a stationary reveiver (f_r)

The frequency shift of the waves is a direct measure of the particle velocity u_p and can, for particle velocities $u_p \ll c$ be approximated by

$$f_r \approx f_l + \frac{\vec{u}_p \cdot (\vec{e}_{pr} - \vec{e}_{lp})}{\lambda_l} \tag{2.2}$$

where c is the speed of light, λ is the wavelength of the laser and $\vec{e}_{lp}$ and $\vec{e}_{pr}$ are the unit vectors from laser to particle and from particle to receiver, respectively.

As f_r lies in the order of 10^7 Hz and is therefore hard to detect and analyze, a dual beam configuration is predominantly used: Two laser-beams are directed at the same volume under an angle θ. Both laser frequencies are affected by the Doppler effect and experience frequency shifts f_{r1} and f_{r2} respectively (compare Eq. 2.2). The frequency difference, referred to as Doppler frequency $f_d = f_{r1} - f_{r2}$, is scattered by a particle traveling with velocity $u_\perp$ to the

superposition region and is a function of the particle velocity as given by

$$f_d = 2\,\frac{\sin(\theta/2)}{\lambda}\,u_\perp \tag{2.3}$$

Figure 2.3 shows a schematic of the dual beam configuration and illustrates the low-frequency signal wave, which is generated by the superposition of two high-frequency waves.

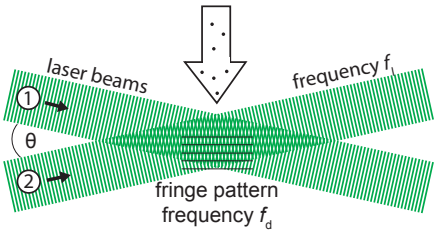

Figure 2.3: Schematic of two superimposed laser beams. Seeding particles within the flow are illuminated by the low-frequency fringe pattern.

Typical dimensions of a measurement volume lie in the order of 50 μm in diameter and 250 μm in length. Extensive explanation of the LDV working principle and applications can be found in Albrecht et al. [2].

2.2.2 Particle Image Velocimetry

The working principle of *Particle Image Velocimetry* (PIV) is based on a particle displacement between two instants in time. The gaseous or liquid working fluid is seeded with tracer particles that are homogeneously distributed in the flow and can be illuminated by a laser sheet. Two snapshots of the flow are taken at two consecutive time steps using high-speed cameras. The in-plane particle velocities (2D2C) can be calculated through a correlation of both snapshots. Using a *Stereo-PIV* system setup all three velocity components inside the illuminated sheet can be measured (2D3C) and a *Tomographic PIV* system enables the acquisition of a 3D3C velocity field. This setup however is usually restricted to small field of views (FOV), of the order of a few cm edge length. In addition, great effort is required to set up a Tomographic-PIV experiment. For extensive information, the reader referred to Adrian and

Westerweel [1] and Raffel et al. [72]. A precondition for the application of PIV is optical access into the region of interest. Optical access must be available for the illuminating laser-sheet as well as for the PIV cameras. Because the laser-sheet and the cameras are positioned orthogonal to each other, optical access into the region of interest from at least two orthogonal sides is required. A sketch of a PIV setup is visualized in Fig. 2.4. Due to its wide scope of applications and the large velocity vector fields that can be acquired, PIV is a wide spread tool for flow quantification.

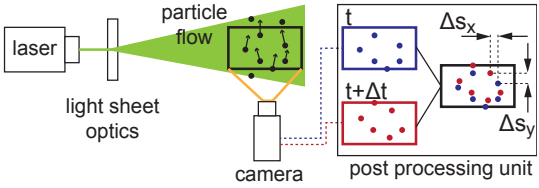

Figure 2.4: Schematic of the Particle-Image-Velocimetry for flow quantification. Figure taken from [80].

2.2.3 MR measurement techniques

Today *Magnetic Resonance Imaging* (MRI) is a state-of-the-art tool for clinical, non-invasive diagnostics of tissues and organs. Commonly sectional views within the region-of-interest (ROI) are made, which is why the technique is also denoted *Magnetic Resonance Tomography*[2]. The working principle of MRI is based on the phenomenon of *Nuclear Magnetic Resonance* (NMR) which was discovered independently by Felix Bloch and Edward Purcell in 1946 [9, 71]. *Magnetic Resonance Velocimetry* (MRV) is an advanced measurement technique based on MRI, which allows the acquisition of 3D3C velocity fields. The working principle of MRV differs from the acquisition techniques mentioned above: It is non-intrusive, meaning that the flow is not influenced by the measurements. No optical access is required and no tracer particles are added to the flow. Instead, the quantum mechanical spins of the atoms in the flow medium emit the flow information as RF waves. These waves are measured in receiver coils, which represent the *flow sensor*. Magnetic access

[2] ancient greek: "*tomos*" – slice, section, "*graphō*" – to write

into the flow domain is therefore required. Unlike the other techniques, the MR techniques cannot readily be realized in gaseous flows. The preferred medium is water. This will be elaborated in Chapter 3.

2.3 Quantitative comparison of measurement techniques

An overview over the measurement techniques outlined above is given in Tab. 2.1.

Data field dimension Besides MRV, a 3D3C flow data set can only be acquired by means of Tomographic PIV. Due to the large effort regarding the measurement setup, and subsequently smaller number of applications, this capability is restricted and placed in parentheses in Tab. 2.1. A bulk share of PIV experiments is conducted to acquire 2D2C and 2D3C velocity fields. Pressure measurements via multi-hole probes, hot-wire anemometry and Laser Doppler Velocimetry are p ointwise measurements enabling only the acquisition of a 1D2C / 1D3C velocity field.

Temporal resolution The highest temporal resolutions are obtained with optical measurement techniques (LDV, PIV) as well as for the intrusive HWA technique. No temporal resolution is specified for the MRV technique. The reason lies in the principle of data acquisition. A three-dimensional measurement volume is not acquired point by point, but rather all at once; with increasing measurement time the acquired data set becomes more accurate. The achieved temporal resolution therefore depends to a great extent on the selected measurement parameters. This will be elaborated in more detail in the corresponding MRV section.

Spatial resolution Regarding the spatial resolution, invasive measurement techniques are limited due to the size of sensor which is placed within the flow regime. Spatial resolution of the order of $\approx 1\,\mathrm{mm}$ can be achieved with the HWA, yet the MHP enables considerably lower spatial resolution of the order of few mm. The spatial resolution of LDV is mainly limited by the precision of the traverse system as well as by the size of the measurement

Table 2.1: Overview of measurement techniques for fluid flow.

	Data field dimension			temporal resolution (kHz)	spatial resolution (mm)	comments
	1D2C / 1D3C	2D2C / 2D3C	3D3C			
MHP	✓/ ✓			≤0.1	>1	intrusive
HWA	✓/ (✓)			>10	≈1	intrusive
LDV	✓/ (✓)			>10	≈0.1	min. 1× optical access
PIV		✓/ ✓	(✓)	>1	≈0.1	min. 2× optical access
MRV		✓/ ✓	✓		<1	magnetic access

volume. Resolutions in the order of 1/10 mm can be achieved. Typical spatial resolutions for the MRV measurements lie in the order of 1 mm in all three spatial directions. Higher spatial resolutions can be achieved (down to 0.3 mm or lower) through a higher main magnetic field B_0 and improved magnetic field gradient systems. Moreover, the selected spatial resolution is always a trade-off between the amount of necessary detail and the emerging decrease in overall signal magnitude and signal-to-noise (SNR) ratio.

3 The MR measurement techniques

This chapter briefly summarizes the principles of the MR technique. For a comprehensive and more detailed understanding of these measurement techniques, the reader is referred to textbooks on the subject, which give an excellent overview: Carr and Carroll [18], Haacke et al. [40], Hendrix [44], McRobbie D.W. et al. [61], and Weishaupt et al. [82]. In contrast to many textbooks, the MR working principles are explained from a classical mechanics perspective. The amount of quantum mechanics perspective is kept to a minimum. This topic will be elaborated in more detail in Sec. 3.2, which is based on Hanson [43].

To begin with, a literature review will give an overview of the different MR imaging techniques.

3.1 Literature review

Magnetic Resonance Imaging (MRI) is an established tool for clinical, non-invasive diagnostics of tissues and organs. Commonly sectional views within the region-of-interest (ROI) are made, which is why the technique is also denoted *Magnetic Resonance Tomography* [1]. The working principle of MRI is based on the phenomenon of *Nuclear Magnetic Resonance* (NMR) which was discovered independently by Felix Bloch and Edward Purcell in 1946 [9, 71]. One of the first documented 2D MRI images were produced by Lauterbur [54] in 1973 who proposed a possible application for the *in vivo* study of malignant tumors. Today, the technique is predominantly used in clinical routine for diagnostics, due to its excellent tissue contrast and the lack of ionizing radiation. A typical clinical examination lasts anywhere from several minutes to about one hour, depending on the type of examination and the size of the region of interest.

[1] greek: "*tomos*" – slice, section, "*graphō*" – to write

Furthermore, MRI can be used to measure blood flow velocity [56]. *Magnetic Resonance Velocimetry* (MRV) allows the acquisition of three velocity components (3C) for every voxel[2] in a three-dimensional measurement volume (3D). It is therefore also denoted *3D3C-MRV* and commonly also known under the synonyms *Flow MRI* and *Phase Contrast (PC) MRI*. For consistency reasons, the flow encoded MR imaging techniques are denoted MRV throughout the course of this work.

The first journal article using the MR techniques to acquire flow dates back to Hahn (1960) [41], who studied the possibility of detecting sea-water motion by using the earth's magnetic field. First in-vivo measurements were presented in 1984 and 1985, by Bryant et al. [14] and Moran et al. [63], respectively, who combined the velocity encoding with regular MR imaging. Since then numerous studies were published for the investigation of human artery or cardiovascular blood flow [10, 18, 51, 56] and the human proximal airways [73].

Different encoding strategies for flow quantification were reviewed by Johnson and Markl [48], Lee et al. [55], and Pelc et al. [66] and quantitative flow measurements were made possible [67]. Extensive studies of MR flow measurements and constraints are presented by Caprihan and Fukushima [16], Elkins and Alley [26], Fukushima [35], and Gladden and Sederman [38]. The accuracy and reproducibility of MR measurements is the subject of more recent puclications by Dyverfeldt et al. [22], Gao and Liu [37], Gladden and Sederman [38], and Wentland et al. [83].

First published MRV applications for engineering purposes emerged in 2003 & 2004 by Elkins et al. [24, 25] and Newling et al. [64], respectively. Since then, a constantly increasing number of publications demonstrates the growing interest into this measurement technique: Mean flow measurements through a *CANDU fuel bundle*[3] Piro et al. [69], concentration measurements in a two-stream mixing layer Benson et al. [7], or in a setup featuring distinct crossflow, Coletti et al. [19], are illustrations of such measurements.

MRV can be acquired in a time-resolved manner also known as *PC CINE MRI*, *Phase-averaged MRV* or *Time-resolved flow MRI*. The techniqe is denoted *4D measurements* in this work. The motivation of time-resolved flow measurements can be traced back to MR angiography measurements of small

[2] voxel: volumetric pixel
[3] CANadian Uranium Deuterium

vessels such as coronary arteries. These measurements were severly corrupted by artifacts caused by respiration, such as motion blur and ghosting artifacts [79]. To face this problem, sequences that allowed the acquisition of velocity vs. time profiles through echocardiographic gating were presented by Hennig *et al.* [45]. These are capable of temporally resolving a series of 3D data sets with velocity encoded data [78, 84]. This enables temporally resolved blood flow visualization [59, 60].

Advanced sequences for very fast data acquisitions, denoted *Real-time acquisitions*, allow the acquisition of flow encoded image slices within a total time for data acquisition, $TA < 50\,\text{ms}$ [49]. This is realized by using multiple receiver coils in parallel to significantly reduce scan-time, Pruessmann *et al.* [70].

The effect of turbulence on the signal magnitude is discussed by several authors (Evans et al. [28], Gao and Gore [36], Jou [50], Kuethe and Gao [52], and Urchuk and Plewes [77]). Quantitative MR turbulence measurements have recently been shown to have great potential for application both in clinical context and in technical flows. For clinical context, turbulent flows occur in many forms of cardiovascular diseases [20, 22], while healthy cardiovascular flow is predominantly laminar. The determination of turbulent kinetic energy can be a good indicator for pressure loss from aortic stenosis [21, 23]. Turbulence measurements were recently acquired in technical flows Elkins et al. [27], using a quantification approach presented by Gao and Gore [36]. Turbulence quanitfication by means of Bayesian probability theory is described by Binter et al. [8], Bretthorst [12], and Xing et al. [86]

Apart from the flow and turbulence quantities, the MR techniques also allow the measure of volumetric temperature information, denoted *MR Thermometry*. This information can, in clinical use, be used to monitor the tissue temperature during tumor treatment and can thus be used to prevent surrounding cells from temperature-induced damage. For engineering purposes, the knowledge about the temperature distribution allows the optimization of components (heat-exchangers, etc.) or can be used to design the flow field regarding optimized heat transfer. A comprehensive explanation of the technique can be found in Buchenberg et al. [15] and Wassermann [80].

3.2 Physical background of the MR-techniques

The focus of this work is the application of the MR techniques for engineering purposes, i.e. the evaluation of these measurement techniques for technical flows. It is therefore important to understand the underlying principles.

In contrast to many textbooks, the MR working principles are explained from a classical mechanics perspective and the amount of quantum mechanics perspective is kept to a minimum. Most aspects of MR can be perfectly understood from a classical perspective, at the same time, the underlying MR working principle is not overly simplified, Hanson [42, 43].

3.2.1 Nuclear magnetic resonance

The principle of the MR techniques is based on the effect of *Nuclear Magnetic Resonance* (NMR). In the presence of a strong magnetic field, atomic nuclei with a non-zero net spin $\vec{I}$ develop a resulting magnetization of the atomic nucleus and start a precession motion at a resonance frequency, namely the *Larmor frequency* ω_{L}. The axis of the precession motion is the direction of the main magnetic field B_0. The frequency ω_{L} is defined by [40]

$$\omega_{\mathrm{L}}(\vec{r},t) = \gamma \cdot \underbrace{(B_0 + \vec{r}(t) \cdot \vec{G}(t))}_{B_{local}} \tag{3.1}$$

where γ is the gyromagnetic ratio[4] and the local magnetic field strength B_{local} is composed of B_0 and additional magnetic field gradients, produced by the gradient system unit, that is an inherent part of clinical MR scanners (see also Sec. 4.3). A principle of the precession motion is illustrated in Fig. 3.1.

A non-zero spin of the atomic nucleus appears in the case of an odd mass number and/or odd atomic number.[5] In Tab. 3.1 resulting spin numbers of selected nuclei are listed. The most common working fluid for the MR techniques is water. While oxygen has zero net spin, the element hydrogen ($\vec{I} = 1/2$) makes water suitable for the MR techniques. The use of other fluids and gases is possible. Newling et al. [64] conducted MR experiments in SF_6 gaseous flow, Rochefort et al. [73] uses hyperpolarized He^3 gaseous flow. The

[4] Material-dependent constant. For hydrogen equivalent to $\gamma \approx 42\mathrm{MHz/T}$.

[5] For the element ${}^{\mathrm{A}}_{\mathrm{Z}}\mathrm{X}$: mass number (A) and atomic number (Z).

Table 3.1: Quantum spin numbers of selected elements.

Nuclide	Element	Spin Quantum number $\vec{I}$
${}^{1}_{1}H$	Hydrogen	1/2
${}^{16}_{8}H$	Oxygen	0
${}^{32}_{16}S$	Sulfur	0
${}^{19}_{9}F$	Fluorine	1/2

signal magnitude of gaseous flows is however significantly lower compared to water flow experiments, essentially due to the lower density. This is why gas flow MR experiments are scarce.

3.2.2 MR signal

Spins with a resulting nuclear spin number generate a longitudinal magnetization parallel to the external magnetic field B_0. This process is shown in Fig. 3.2. Visualized are spins that originate from an exemplary cube volume. In the initial condition (Fig. 3.2 left) the spins point in arbitrary directions, such that no net magnetization is created by the spin ensemble.[6] When the spin ensemble is placed inside an external magnetic field, the spins have a tendency to align with the external magnetic field. The spin distribution is no longer homogeneous and a resulting ensemble magnetization is created, which is illustrated by the red arrow. The total magnetization of the spin ensemble is denoted M_0 and is calculated via [9]

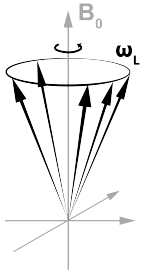

Figure 3.1: Sketch of the spin precession motion around the direction of the main magnetiic field B_0.

$$M_0 = \chi \cdot B_0 \tag{3.2}$$

where χ denotes the material's magnetic susceptibility and B_0 is the main magnetic field strength. The resulting magnetization M_0 corresponds to about

[6] Each spin in the ensemble can be imagined as a little bar magnet. Due to a homogeneous distribution of the spins, no magnetization is created.

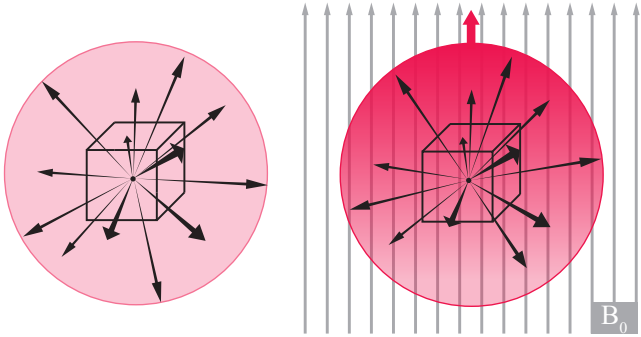

Figure 3.2: Snapshot visualization of spins within an arbitrary volume. Left: Initial condition. Spins point in arbitrary directions. Right: Situation when placed inside an external magnetic field. Spins tend to align with the B-field, resulting in a longitudinal magnetization, represented by the red arrow. Adapted from [43].

3 ppm of the total number of spins inside the volume. A water volume of a cube with 1 mm edge length, however, comprises $\approx 4 \cdot 10^{14}$ spins. M_0 is thus measurable.

The spin ensemble has the same characteristics as the single spin and precesses in the existence of an external magnetic field with the Larmor frequency ω_L, given in Eq. 3.1.

Through radio frequency (RF) pulses, the precession axis is tilted, causing the development of *transverse magnetization*. This procedure is visualized in Fig. 3.1 for a single spin that precesses at an angle α around the axis of the main magnetic field B_0. The established deflection angle α depends on the amplitude and duration of the applied RF-pulse (B_1-field) and the duration of the applied pulse. It can be described by [40]

$$\alpha = \gamma B_1 \tau \tag{3.3}$$

Note that any angle α can be produced by the B_1-pulse. Depending on α, the magnetization M_0 is decomposed into the fraction parallel to the main magnetic field, $M_{\parallel} = M_z$, and the fraction of magnetization perpendicular to the main magnetic field, the transverse magnetization $M_{\perp} = M_{xy}$, as illustrated in Fig. 3.3.

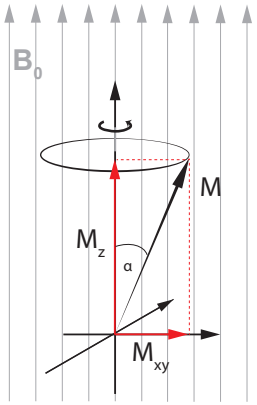

Figure 3.3: Decomposition of the magnetization M into the longitudinal magnetization M_z and transversal magnetization M_{xy} under the deflection angle α.

$$\begin{pmatrix} M_x \\ M_y \\ M_z \end{pmatrix} = -\gamma M_0 \begin{pmatrix} -\sin\alpha\cos\omega_L t \\ \sin\alpha\sin\omega_L t \\ \cos\alpha \end{pmatrix} \tag{3.4}$$

Eq. 3.4 describes the deflection of the magnetization vector by the angle α immediately after the application of the RF-pulse. The established transversal magnetization precesses in the x-y-plane and slowly dissipates, while at the same time the longitudinal magnetization vector $\vec{M}_z$ is recuperated. This process is called *relaxation* and the duration during which these processes take places are denoted *relaxation times*.

3.2.3 Relaxation times

Longitudinal relaxation After the RF-pulse the transverse magnetization starts to decay and the MR signal can be measured as an echo of the free induction-decay in receiver coils. However, the received MR signal decays rapidly, i.e. the transverse magnetization gradually diminishes and the spin ensemble moves back to its original state. The relaxation in the longitudinal direction, *spin-lattice relaxation* or T_1*-relaxation*, is the time it takes to

recreate a longitudinal magnetization $M_{\parallel}$ equivalent to 63% of the net magnetization M_0. Eq. 3.5 expresses the longitudinal magnetization as a function of time [61].

$$M_{\parallel}(t) = M_0 \left(1 - (1 - \cos\alpha)\, e^{-t/T_1}\right) \tag{3.5}$$

Transverse relaxation The *spin-spin relaxation* is a measure for the decay of *transverse magnetization* $M_{\perp}$. Local fluctuations in the magnetic field strength will eventually lead to a reduction of the phase coherence of a spin ensemble. These fluctuations are caused by the magnetic moments of neighboring spins. Through the decline in phase coherence, the transverse magnetization is effectively diminished. The time constant of this process is denoted T_2 time. Both T_1 and T_2 time constants are material dependent and temperature dependent. Typical relaxation times for water and fat are provided in Tab. 3.2.

Due to local B-field inhomogeneities, this results in locally varying Larmor frequencies (Eq. 3.1); the reduction of transversal magnetization procedes considerably faster than in a perfectly homogenic B-field. This effect is considered by the T_2' time constant. The effective time constant for the decay of the transverse magnetization can thus be described via the $T_2^{\star}$ time constant, which considers both processes and is given by

$$T_2^{\star} = \left(\frac{1}{T_2} + \frac{1}{T_2'}\right)^{-1}. \tag{3.6}$$

The transverse magnetization after a 90°RF excitation pulse can be calculated by [61]

$$M_{\perp}(t) = M_{\perp}(0) e^{-t/T_2^{\star}}. \tag{3.7}$$

The exponential behavior of both relaxation processes and their characteristic time constants T_1 and $T_2^{\star}$, are displayed in Fig. 3.4.

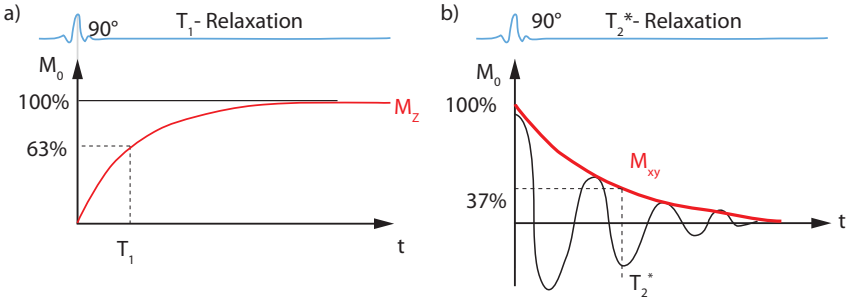

Figure 3.4: Illustration of the spin-lattice (left) and spin-spin (right) relaxation times after an RF-pulse excitation of a spin-ensemble. Graphic adapted from [80].

Table 3.2: Typical relaxation times for water and fat in a 1.5T magnetic field [44].

	T1	T2
water	3.0 s	1.5 s
fat	0.2 s	0.1 s

3.2.4 Creating the image

Image creation, i.e. the generation of a spatial resolution of the received MR signal, is covered in this section. The underlying principle: The received MR-signal is a composition of the signal that evolves from the entire field of view (FOV), where transverse magnetization has been established through RF excitation. The signal is stored as a magnitude distribution in the frequency domain, called *k-space*. It is transformed back into the spatial domain using a two-dimensional inverse Fourier transform. Assignment of a unique phase and frequency for each location within the FOV is used to spatially encode the image.

Spatial encoding

By a systematic spatial and temporal manipulation of ω_{L} within the measurement domain, the MR signal can be spatially encoded. This enables the adjustment of the signals frequency and phase angle of the spins depending on the position in the FOV and can be realized through the application of magnetic field gradients (see Eq. 3.1, page 18). The magnetic field gradients are superimposed onto the main magnetic field B_0 in any arbitrary direction, thus changing the local magnetic field B_{local}. The process of spatially encoding consists of three independent procedures that are consecutively performed during the MR measurements: *Slice selection* (SS), *Frequency encoding* (FE), and *phase encoding* (PE).

Slice selection A magnetic field gradient, denoted *slice select gradient* (SS-gradient), is applied in an arbitrary spatial direction.[7] This gradient manipulates the local magnetic field strength B_{local} (Eq. 3.8) and thereby also ω_{local} (Eq. 3.1) along the direction of the applied gradient.

$$B_{local}(z) = B_0 + z\frac{dB'_z}{dz} \tag{3.8}$$

The SS-gradient and its effect is illustrated in Fig. 3.5a. Displayed is an exemplary object. The local Larmor frequency ω_L varies in z-direction due to

[7] Slice direction can be chosen, however it is usually intended to orientate the slice direction along the axis of the measurement volume with the smallest extent in order to reduce the number of acquired slices.

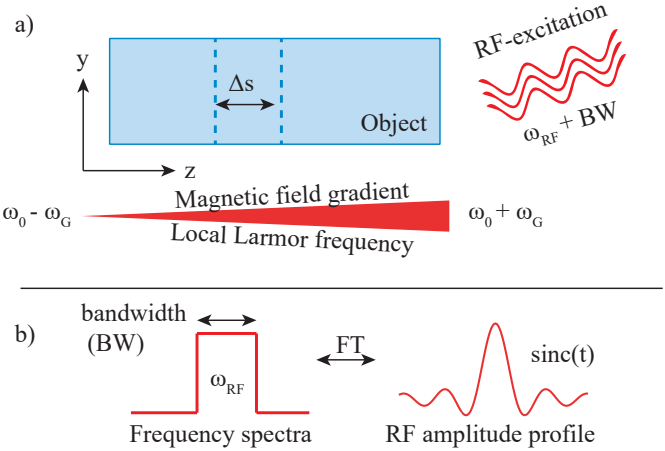

Figure 3.5: Representation of the slice selection process. A magnetic field gradient is superposed onto the main magnetic field, manipulating the local magnetic field strength along the z-direction. The RF-excitation pulse features a distinct frequency ω_{RF} and bandwidth BW, that directly influence location and thickness Δs of the excited slice.

the applied SS-gradient. Simultaneously, the RF-excitation pulse is played out with a distinct frequency ω_{RF} and bandwidth $\Delta\omega$. Only the spin ensembles in slice direction with a corresponding Larmor frequency ω_L are influenced by the RF-pulse and develop a transverse magnetization $M_\perp$. This region has a defined slice thickness Δs. The RF amplitude profile of the RF-pulse is depicted in Fig. 3.5b. The Fourier transform of the amplitude profile identifies the bandwidth of the RF-pulse. The thickness of the slice selection Δs can be set by the slope of the applied SS-gradient and the bandwidth of the emitted RF-pulse $\Delta\omega$.

The spin-ensembles within the selected slice of thickness Δs develop a transverse magnetization $M_\perp$ and generate the MR signal. The signal that is measured, is a combination of signals from the slice that is being imaged. However, the spatial encoding must be realized also within this slice. This process is performed by the combination of the *phase encoding* (PE) and the *frequency encoding* (FE) gradients which are applied consecutively.

Phase and Frequency encoding The following explanation is graphically illustrated in Fig. 3.6. The PE-gradient is applied along one direction within the excited slice for a distinct period of time, in the depicted case the PE-direction corresponds to the y-direction within the slice. Due to the increase in ω_L while the gradient is applied, the spin ensemble acquires a phase-shift $\Delta\phi$ along the gradient axis, which is equivalent to

$$\Delta\phi(y) = \int \gamma \vec{G_{PE}}\, \mathrm{d}\tau \tag{3.9}$$

and depends on the duration τ and the amplitude of the PE-gradient $\vec{G}$.

Subsequently, the FE-gradient is applied along the axis orthogonal to the PE-gradient. Since the MR signal is recorded while the FE-gradient is applied, it is also denoted *readout-gradient*. The received signal originates from the entire slice. It is read out while the FE-gradient is applied and is spatially encoded along the FE-gradient direction. In Fig. 3.6 this corresponds to the horizontal x axis. A 1D-Fourier transform (FT) converts the MR signal from the time domain into the frequency domain. After the FT along the FE-gradient direction, the signal is saved in the *raw data space*, also called *k-space*. (Fig. 3.6c). A inverse Fourier transformation would depict a projection

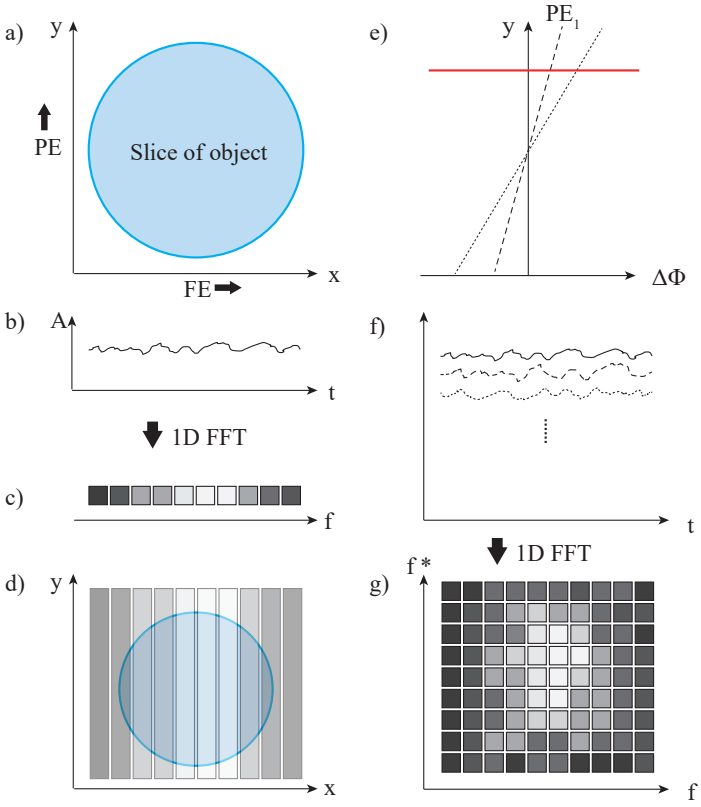

Figure 3.6: Frequency (FE) encoding and Phase (PE) encoding gradients are applied in order to spatially encode the received MR-signal.

of the image that is spatially encoded along the x direction, (Fig. 3.6d).

However, in y-direction the signal is not yet spatially encoded. The entire imaging procedure is repeated with the only difference being a change in amplitude of the applied PE-gradient (Fig. 3.6e). The change in PE-gradient amplitude provokes a different amount of phase dispersion along the y-direction, effectively resulting in a change of the received signal intensity. This process is repeated for the desired number of "spatial resolution steps" in PE-direction (Fig. 3.6f). A subsequent FT can establish a relationship between the "change of rate of phase"[8] and the change in signal intensity. The received MR-signal of the selected slice is spatially encoded (Fig. 3.6g). A 2D inverse Fourier Transform can reconstruct the local signal magnitude and phase angle of the signal at every voxel in the FOV.

3.3 Flow MRI

Two main techniques for flow acquisition using the MR techniques are presented in this section. The *Magnetic Resonance Velocimetry* technique is capable of measuring time-averaged mean flow velocities in a 3D domain. *4D MRV* measurements, also denoted *4D measurements*, allow also phase-resolved acquisitions of 3D velocity fields for periodic flows.

3.3.1 Magnetic Resonance Velocimetry

Working principle

In order to measure fluid flow with the MR techniques, the phase-image of the received MR-signal is used which can be manipulated by the gradient unit. Spins accumulate phase under the influence of a magnetic field gradient [20]:

$$\phi(\vec{r},t) = \phi_0 + \gamma \left(\vec{r} \underbrace{\int_0^T G(\vec{r},t)dt}_{M_0} + \vec{v} \underbrace{\int_0^T tG(\vec{r},t)dt}_{M_1} + \frac{1}{2}\vec{a} \underbrace{\int_0^T t^2 G(\vec{r},t)dt}_{M_2} \right) \tag{3.10}$$

[8] which corresponds to the frequency $f^\star$

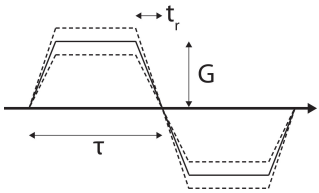

Figure 3.7: Bipolar pulse applied for the MRV measurement technique. The pulse is characterized by its amplitude G, the ramp time t_r and lobe duration τ.

where $\vec{r}$ is the position vector of the spins and $\vec{v}$ is the velocity of moving spins. The influence of the magnetic field gradient on the phase of stationary spins is described by the zeroth gradient moment M_0. Constantly moving spins contribute the amount of the first gradient moment M_1 to the accumulated phase. The second gradient moment M_2 describes the phase accumulation due to spins accelerating along the gradient direction. The idea is based on an established phase difference as a measure of the spins constant flow velocity. Therefore, the influence of the first gradient moment M_1 on the accumulated phase has to be isolated.

Fig. 3.7 shows a bipolar gradient, which can be applied in arbitrary directions by the gradient unit system. The bipolar gradient consists of two gradient lobes with equal gradient moments but opposite polarities that are applied consecutively.

During the first lobe of the bipolar gradient static spins gain phase, which they lose again during the second lobe. The resulting zeroth gradient moment is $M_0 = 0$. Spins, moving with a constant velocity along the gradient direction, lose more phase during the second lobe, than they acquired in the first half, since they move in the direction of a larger magnetic field strength. A resulting phase shift remains, according to

$$\phi = \phi_0 + \gamma \vec{v} M_1. \tag{3.11}$$

The contribution of the second gradient moment M_2 is usually neglected under the assumption of constant flow velocity during the duration of the bipolar gradient. However, the unknown background phase ϕ_0 must still be removed. This is achieved by a second measurement with zero moments M_0 and M_1 for

both static and moving spins, denoted *velocity compensated* reference scan. After subtracting both scan segments, a resulting phase difference $\Delta\phi$ of the two scans (superscribed with (1) and (2) for scans 1 and 2, respectively) is:

$$\Delta\phi = \phi_1^{(1)} - \phi_1^{(2)} = \gamma\vec{v}\Delta M_1 \tag{3.12}$$

The phase difference of Eq. 3.12 is generated by the spins, moving with constant velocity along the bipolar gradient direction. It is apparent, that the phase difference is influenced by the velocity $\vec{v}$ and the strength of the first gradient moment M_1. Rearranging Eq. 3.12 yields an expression for the flow velocity:

$$\vec{v} = \frac{\Delta\phi}{\pi}\mathrm{VENC} \tag{3.13}$$

Thus the velocity $\vec{v}$ can be calculated from the measured phase difference $\Delta\phi$ and the *velocity encoding value* (VENC) value. The VENC value relates the resulting phase difference to a velocity. The VENC must be chosen such that the highest velocities in the FOV lie below the VENC value in order to avoid aliasing effects. By setting the VENC value, the magnitude of bipolar magnetic field gradients mentioned above can be chosen.

$$\mathrm{VENC} = \frac{\pi}{\gamma\Delta M_1} \tag{3.14}$$

However, the VENC should be chosen as low as possible to provide highest signal-to-noise ratio (SNR). Large VENC values increase the standard deviation (SD) of the measured velocities as given by [40]:

$$SD(v_i) = \frac{\sqrt{2}\cdot\mathrm{VENC}}{SNR_{\mathrm{mag}}\cdot\pi}, \qquad i = x, y, z \tag{3.15}$$

$$SNR_{\mathrm{mag}} = \frac{\mathrm{mean(signal)}}{2\cdot SD(\mathrm{noise})} \tag{3.16}$$

SNR_{mag} is the signal-to-noise ratio of the magnitude image and not of the phase image that carries the velocity information. The noise in the magnitude image is considered to be representative noise of the phase image, which can be determined for the MRV data set (Haacke *et al.* [40]).

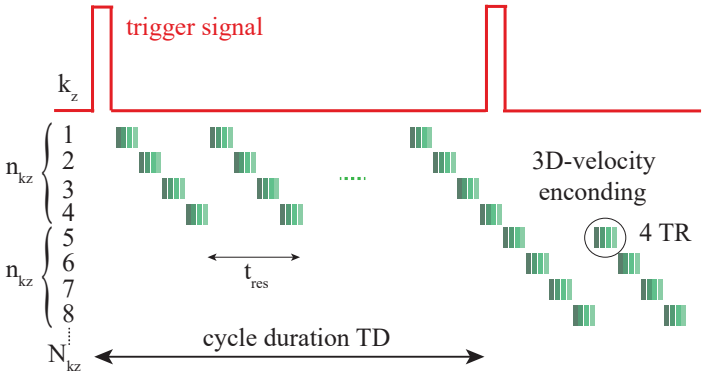

Figure 3.8: Phase-encoding scheme for 4D MRV acquisition with flow encoding along all spatial directions and a selected number of $n_{kz} = 4$ slice encodes for each cycle. Cycle duration TD. Quasi temporal resolution t_{res}. Graphic adapted from Markl et al. [58].

3.3.2 4D MRV

The *4D MRV measurement technique* allows the acquisition of phase-averaged 3D3C velocity fields in periodic flows, i.e. cardiovascular flows that are often acquired ECG-gated (electrocardiogram) [58, 59]. In that case the periodic cycle is subdivided into a certain number of phase angles yielding a "temporal resolution" t_{res}. A complex MR signal is acquired for each phase encoding step. A certain total number of phase encoding steps has to be collected to achieve the chosen spatial resolution of the MR image. Multiple phase encoding steps can be consecutively conducted per cycle to reduce the acquisition time. A scheme for 4D MRV acquisition is shown in Fig. 3.8.

The total acquisiton time (TA) can, in this case, be calculated via

$$TA = N_{PE} \cdot \frac{N_{kz}}{n_{kz}} TD \tag{3.17}$$

where N_{PE} denotes the number of phase encoding steps, N_{kz} is the total number of slice-encoding steps and TD is the cycle length. The denominator n_{kz} stands for the number of interleaved slice encodings. The selected number of $n_{kz} = 4$ reduces the acquisition time TA by 75%.

3.4 Measurement of turbulence quantities

Turbulent flows undergo increased turbulent diffusion compared to laminar flows, which results in a decrease in signal magnitude for flow encoded MR images. This effect is illustrated in Fig. 3.9. Displayed is the received signal magnitude of the Backward Facing Step (BFS) setup in gray scale values from white to black, representing high and low signal magnitudes, respectively. Displayed is the signal magnitude, under the same flow conditions, when no gradient is applied (S_0, top) and when a bipolar gradient with a gradient strength of $S_g = 40\,\mathrm{mT/m}$ is applied in the main flow direction x (S_{x40}, bottom). A significant decline in signal magnitude is visible in the shear layer downstream of the step (②) as well as in the turbulent mixing zone further downstream (③).

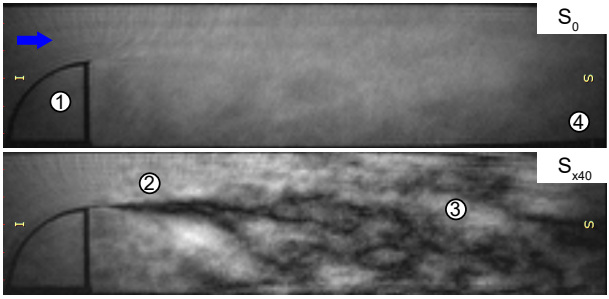

Figure 3.9: Magnitude intensity of the received MR signal (gray values from bright to black represent high and low signal magnitude, respectively). Top: Magnitude S_0, without applied gradient. Bottom: Magnitude S_g, when turbulence encoding gradient applied.

The decay in signal magnitude is due to intravoxel phase-dispersion within a voxel and is not desired, as it degrades the SNR. However, the amount of signal decay can be used as a quantitative measure for turbulence quantities. In contrast to the information of flow and temperature, turbulence is thus not encoded in the signal phase, but in the magnitude itself. This effect is depicted in Fig. 3.10. Two exemplary voxels are visualized, situated in nearly laminar flow (a) and highly turbulent flow (b).

The signal magnitude of the voxels, as detected in the receiver coil, is com-

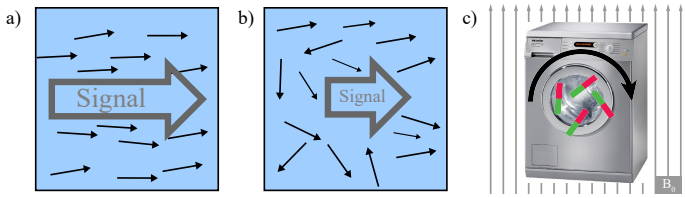

Figure 3.10: Visualization of the signal magnitude in nearly laminar flow (a) with respect to signal decay due to intravoxel phase dispersion inside a voxel in highly turbulent flow (b). (c) Illustration of the intravoxel phase dispersion due to turbulent flow. Spins are represented as little bar magnets, tumbling inside the washing machine and tend to align with the strong magnetic field. The tumbling motion in turbulent flow is considerably increased, provoking further signal loss.

posed of the integral over the spin ensemble present within this voxel. The exemplary voxels in Fig. 3.10 are geometrically identical and composed of the same number of spins.[9] Yet, the net signal originating from the voxel which is situated in the turbulent flow regime, is considerably lower than the signal of its counterpart situated in laminar flow. This is due to intravoxel phase dispersion. A vivid illustration of the increased intravoxel phase dispersion process in turbulent flow is displayed in Fig. 3.10c. The spins inside the voxel are represented as little bar magnets that are placed inside a "washing machine". The washing machine is in tumble mode, preventing the bar magnets from aligning with the external magnetic field. Here, the "tumble mode" is a representation for the thermal energy of the water, which provokes the chaotic movement of the spin ensemble and is responsible for the comparatively small magnetization of the ensemble (see Sec. 3.2.2, page 19). The "tumble speed" in turbulent flows is considerably increased. The consequence is a further decrease in signal amplitude.

Turbulent diffusion All models for turbulence measurements assume homogeneous turbulence as a random velocity which is superimposed on a steady flow velocity. Turbulent diffusion, which in the case of homogeneous, isotropic turbulence, is dependent on the standard deviation of the mean flow velocity

[9] $\approx$ 400 billion spins / cm^3 in water

v_{mean}, can be expressed as (Batchelor [3])

$$D_{turb}(t) = \left\langle u'^2 \right\rangle \int_{t_0}^{t} \underbrace{\frac{\langle u'(t)u'(t+t^*)\rangle}{u'^2}}_{R(t^*)} dt^* \tag{3.18}$$

where the integrand corresponds to the autocorrelation of the flow velocity R(t*). The turbulent diffusion lies some orders of magnitude higher than the rate of diffusion in laminar flows or in flows with zero flow velocity. The amount of molecular diffusion can therefore be neglected (Batchelor [3]). With the assumption, that the autocorrelation of the flow velocity $R(t^*) = 1$ Eq. 3.18 reduces to $D_{turb} = \left\langle u'^2 \right\rangle (t - t_0)$.

Approach for turbulence quantification One approach is based on the expression for the MR signal from a turbulent fluid, which is given by Carr and Purcell [17]

$$S = S_0\, e^{-\gamma^2 G^2 \left\langle u^2 \right\rangle T_0 \left[2/3\,\tau^3 - 2\,\tau\,T_0^2 + T_0^3 \left(3 - 4\,e^{-\tau/T_0} + e^{-2\tau/T_0}\right)\right]} \tag{3.19}$$

and which can be simplified to

$$S = S_0\, e^{-1/2\,\gamma^2 G^2 \left\langle u^2 \right\rangle \tau^4} \tag{3.20}$$

given that $\tau \ll T_0$, Gao and Gore [36]. This precondition holds true for most imaginable applications, since the lobe duration in modern MR scanners and sequences lies in the order of $\tau < 1\,ms$, while the integral time scale T_0 is usually $T_0 > 10\,ms$ [27, 36]. Elkins et al. [27] adapted this expression for a realistic bipolar gradient shape, describing it with the ramp time tr, single *lobe duration* τ and time varying amplitude $G(t)$ (see Fig. 3.7 on page 29 for a depicted shape of the gradient). They found the equation

$$S(G) = S_0\, e^{-\gamma^2 G^2 \left\langle u'^2 \right\rangle f(\tau, tr, T_0)} \tag{3.21}$$

where $f(\tau, tr, T_0)$ is the *timing function*. The timing function f can be approximated to [27]

$$f(\tau, tr, T_0) = \frac{1}{2} t_r^2 \tau^2 - t_r \tau^3 + \frac{1}{2} \tau^4. \tag{3.22}$$

Turbulence measurements are repeated with several different gradient amplitudes G, yielding different signals (Eq. 3.21). The velocity variance can then be determined as least-square fit from Eq. 3.23.

$$\sigma_u^2 = \left\langle u'^2 \right\rangle = \frac{\ln\left(S_0/S\right)}{\gamma^2 G^2 f\left(\tau, tr, T_0\right)} \tag{3.23}$$

A similar approach is based on the signal of a voxel in the presence of a first gradient moment, which can be expressed by [23]

$$S(\vec{k_v u}) = C \int_{-\infty}^{\infty} s(\vec{u}) e^{-i\vec{k_u}\vec{u}} du. \tag{3.24}$$

Here, C is a scaling factor which is influenced by the MR-measurement settings and the flow under investigation.[10] The spin velocity distribution $s(\vec{v})$ is assumed Gaussian [36], and can be written as

$$s(\vec{u}) = \frac{1}{\sigma\sqrt{2\pi}} e^{-\frac{1}{2\sigma^2}(\vec{u} - \vec{u_m})^2} \tag{3.25}$$

where σ denotes the standard deviation (SD) of the mean flow velocity $\vec{v_m}$. The combination of Eq. 3.24 and Eq. 3.25 leads to the expression of the received signal amplitude S as a function of $\vec{k_u}$, which is composed of the first gradient moment and the gyromagnetic ratio, $\vec{k_u} = \gamma M_1$

$$S(\vec{k_u}) = C e^{-\frac{\sigma^2 \vec{k_u}^2}{2} - i\vec{u_m}\vec{k_u}} \tag{3.26}$$

Two measurements with different first gradient moments can be obtained, yielding different signals (Eq. 3.26). The influence of the scaling factor C can

[10] relaxation parameters T1,T2*, spin density, receiver gain and more.

thus be removed and an expression for the SD can be found

$$\sigma_u = u_{rms} = \sqrt{\frac{2\ln\left(\frac{\left|S(\vec{k_{u2}})\right|}{\left|S(\vec{k_{u1}})\right|}\right)}{\vec{k_{u1}}^{\,2} - \vec{k_{u2}}^{\,2}}} \tag{3.27}$$

Eq. 3.23 and Eq. 3.27 yield very similar results for the SD (σ_u), the main difference being the amount of data required for calculation. While Eq. 3.27 is calculated using two measurements with different first gradient moment M_1,[11] Eq. 3.23 is calculated from a series of measurements with different first gradient moments by a least-square fit. This is the more robust approach and is chosen for the turbulence quantification presented in Chapter 7.

A different approach to the estimation of turbulence quantities using Bayesian probability theory was established by Bretthorst [12] and later successfully implemented by [8]. This approach is not covered in the context of this work.

[11] In fact, one measurement should be acquired with $M_1 = 0$ [23] to yield the best signal level possible

4 Methods and Facilities

The main facilities and devices used throughout the course of this work are presented. The manufacturing process of the experimental setups (i.e. flow model manufacturing) is described, and the process of data acquisition and data post processing is outlined.

The section starts off with a description of the *Transparent Engine Test Bench*. The author did not work on, or conduct measurements inside the transparent engine test bench. Nevertheless, the PIV-results conducted inside the test bench were crucially valuable for the validation of the MRV-measurements that were conducted in 1 : 1 scale models of the transparent engine cylinder head. For completeness, the test bench is therefore described in the following paragraphs.

4.1 Transparent Engine Test Bench

The *Transparent Engine Test Bench* (ETB) consists of a one-cylinder, direct injection spark ignition (DISI) engine with optical access at various locations. This test bench allows the investigation of internal flow and combustion processes inside the cylinder during operation, through PIV measurements. These processes include flow velocity, temperature distributions, flame propagation, flame-wall interactions and the analysis of combustion residues. Fig. 4.1 is a photo of the ETB, while the engine is running. Flame propagation during the combustion cycle is visible (see ②).

Optical Access Optical access is available through the straight piping of the intake manifold by a DN50 (56.3 mm inner diameter, 70 mm length) fused-silica cylinder (see ①, Fig. 4.1). Various flow properties can be measured at this position, including flow temperature, pressure and flow velocity. Optical access into the combustion chamber of the DISI engine is provided through the cylinder liner. It is made from a 55 mm high quartz-glass liner with a 8-mm

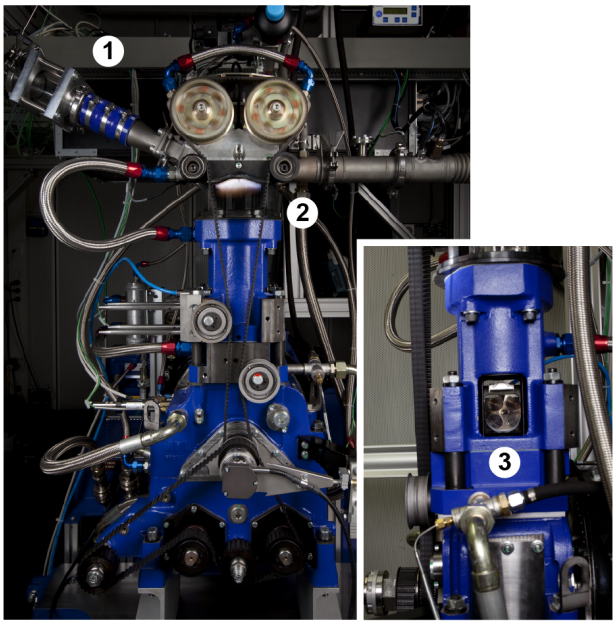

Figure 4.1: Photography of the *Transparent Engine Test Bench.*① Optical access into the straight piping to quantify the properties of the intake flow. ② Optical access into the combustion chamber through a quartz-glass liner. Fig. 4.1(right) depicts a sideview of the test bench. The optical access for laser sheet illumination is provided through a flat quartz-glass piston. The projection of the cylinder head is visible, see ③. Source of the photographs: Technische Universität Darmstadt / Katrin Binner.

window extension into the pentroof (20 mm thickness), ②. Fig. 4.1(right), is a sideview of the engine test bench. The optical access for laser sheet illumination is realized by a Bow-ditch-piston with flat quartz-glass piston-crown window (75 mm diameter), ③.

Cylinder Head Geometry The cylinder head of the transparent engine test bench can be exchanged, allowing to investigate the influence of cylinder head geometry changes on the in-cylinder flows. Two different cylinder heads were installed and the in-cylinder flow was analyzed by means of PIV-measurements.

The two cylinder head geometries utilized in this work are denoted as the *Wall-Guided Cylinder Head* and *Spray-Guided Cylinder Head*. The main geometrical difference between the WG and the SG cylinder head is the position of the fuel injector. The injector is side-mounted within the WG geometry, while it is moved into the central position, in direct proximity of the spark plug inside the cylinder camber, for the SG cylinder head. Further geometrical differences between the WG and the SG cylinder head geometry are listed in Tab. 4.1. Both cylinder heads feature a dual-port intake system designed to provide a tumble flow motion within the combustion chamber. Bore and stroke of this engine are 86 mm, which is independent of the cylinder heads used. The WG cylinder head is equipped with intake and exhaust valves, both 33 mm in diameter. The intake valves of the SG cylinder head are reduced to 29 mm in diameter to account for the central location of the fuel-injector, while the exhaust valves have equal dimensions in both configurations. The reduction in diameter of the intake valves requires an adaptation of the intake channels of the SG cylinder head. A transparent model of both cylinder head geometries is illustrated in Fig. 4.2. ① indicates the different position of the injector. It is is apparent that the intake valves of the SG cylinder head must be reduced in diameter in order to account for the new injector location (②). The geometrical changes of the SG cylinder head's intake channels are indicated by a green dashed lines.

An extensive description of the transparent engine test bench can be found in Baum [6]. Important settings of the PIV measurements are provided in [4, 5].

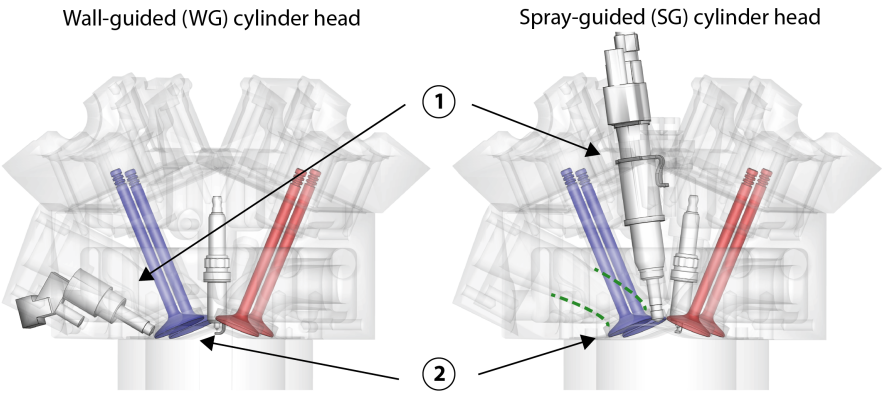

Figure 4.2: Wall-Guided (WG) and Spray-Guided (SG) cylinder head and their geometrical differences. ① illustrates the change of the injector position. Due to the central injector position for the SG cylinder head, the diameter of the intake valves is reduced, see ②. Geometrical changes of the intake channel to account for the smaller intake-valve diameter are indicated by dashed green lines. (Graphics adapted from [6]).

Table 4.1: Geometrical differences of the Wall-Guided (WG) and Spray-Guided cylinder head.

	WG	**SG**
intake valve diameter	33 mm	29 mm
exhaust valve diameter	33 mm	33 mm
injector position	side	central
geom. compression ratio	8.5	8.7

4.2 Flow supply systems for MR measurements

The main flow supply and conditioning system is a portable, custom built closed-loop system to provide the experiment with a flow rate up to $\dot{V} \approx 120\,\mathrm{L/min}$. The flow supply system is connected to the experimental setup via 25.4 mm PVC hoses, which lead the flow from the *Console room* into the *Scanner room* through guide vanes. After leaving the experimental setup, the flow is guided back into a 100 L water tank from where it is recirculated into the flow supply system. The flow rate is provided by a 1.1 kW magnetically centrifugal pump (*Sondermann, Type RM3*), and measured by two ultrasonic flow meters (*systec controls, deltawaveC*) that are positioned upstream and downstream of the flow model and thereby allow the identification of potential leakage flow. The flow meters enable a very precise measurement of the volumetric flow rate with a standard measurement uncertainty of $\approx 1\%$ of the measured value. The flow can be heated by a 2 kW heating foil, situated inside the water-tank. The pressure (*labom, ECO CB7500* pressure transmitter) and the temperature (*Pt100* temperature sensor) of the flow are measured. All flow parameters are monitored and controlled using a purpose made LabView® program.

A recirculating cooler (Julabo FC1200T) is used for the experiments that require a secondary flow supply system, as is the case for the measurements presented in Sec. 6.3. This secondary flow supply system provides a flow rate of 15 L/min and the flow can be cooled down to a temperature of $T \approx 10^\circ$ C.

A schematic of the experimental setup and photographs of the flow supply systems is depicted in Fig. 4.3. The *scanner room* and the *console room* are spatially separated, the scanner room is also designed as Faraday cage in order to prevent external radiowaves from entering the scanner room and thereby disturbing the measurements. While the flow model is positioned inside the MR scanner, the flow supply systems are placed inside the console room, from where the measurements are started and monitored. Two flow supply systems are depicted in Fig. 4.3.

Working fluid

Virtually all in-situ MR-experiments are performed with water flow as working fluid. However, other fluids, including blood-mimicking fluids and gels

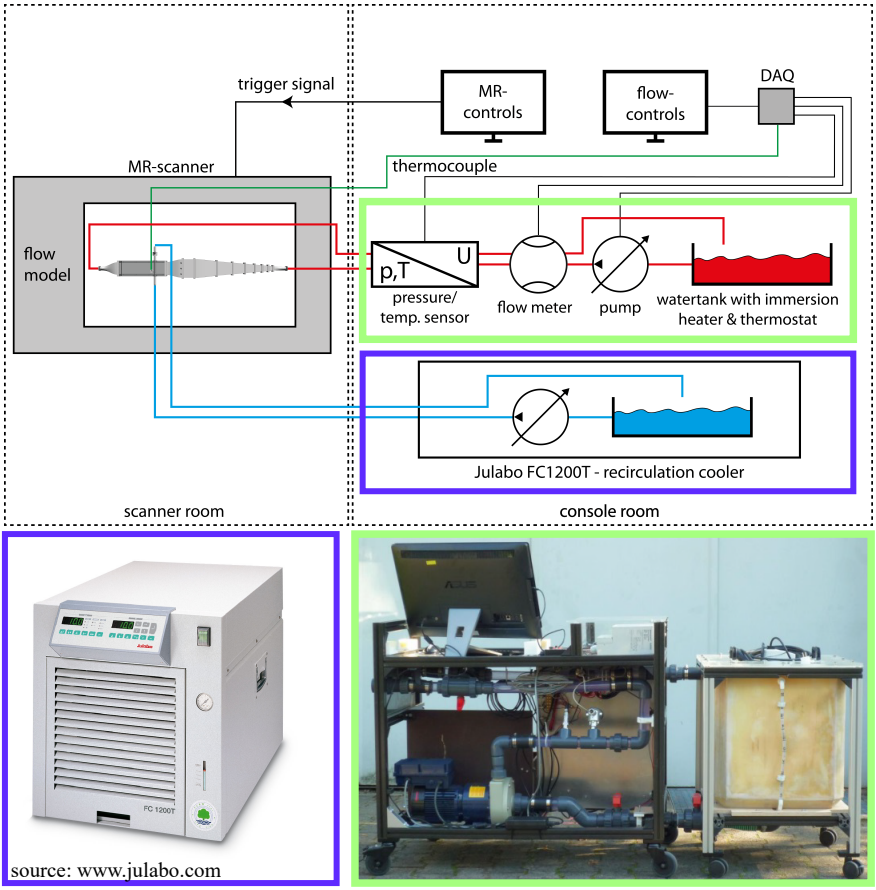

Figure 4.3: Top: Schematic of the experimental measurement setup. The setup is split up and situated in two rooms, as indicated by the black dashed lines. The MR controls, data acquisition systems and flow supply systems are situated in the console room. The measurement model is placed inside the MR scanner within the scanner room. A special shielding (Faraday cage) is built around the scanner room preventing electrical interference from radiofrequency sources outside of the scanner room. The flow is lead through guide vanes into the scanner room. Bottom: The *Julabo FC1200T* circulation cooler (left) and the custom-made flow supply system (right). (Schematic adapted from Wassermann [80]).

and even gaseous flows can be used [64, 73]. The working fluid utilized for the presented measurements is de-ionized water with added contrast agents (CA). CA are not to be confused with tracer particles used in optical measurement techniques such as PIV or LDV. The CA itself is not measured by the MR technique; it merely reduces the fluids longitudinal relaxation time T_1 without changing the properties of the water. Through the reduction of T_1, measurement time can be significantly reduced.

For the measurements presented in the context of this work, two different types of CA were used:

- Gadopentate dimeglumine (Magnevist®, Schering AG, Berlin, Germany) is a gadolinium-based CA, which is frequently used in clinical applications, where it is injected intravenously. It significantly decreases T_1 (and to some extent also the transverse relaxation times $T_2/T_2^\star$). For the measurements a concentration of 1.08 mmol/L CA was prepared with de-ionized water. No toxicological effects are expected. However, because the CA is biodegradable, the CA-water solution has to be exchanged frequently, which involves considerable costs.

- Copper(II) sulfate salt ($CuSO_4$) is not permitted in clinical (patient) use because of its toxicological effect on the human organism. For the technical applications however, $CuSO_4$ turned out to be a suitable alternative for the gadolinium CA.

4.3 MR Scanner

The MR scanners used to conduct the measurements presented in the context of this work were standard 3 Tesla MAGNETOM® Prisma MRI systems (Siemens Healthcare, Erlangen, Germany), owned by the Department of Radiology, Medical Physics, University Medical Center in Freiburg. MR systems consist of three main components:

- The main magnetic field strength $B_0 = 3\text{T}$ is produced by a helium-cooled, superconducting magnet, corresponding to about 60.000 times the strength of the earth's magnetic field.[1]

[1] 1T (Tesla) ≡ 10.000 G (gauss). Earth's magnetic field ≈0,5 G

- The radiofrequency unit (RF-unit) consists of a *transmitter coil* (also denoted *body coil*) and *receiver coils*. The transmitter coil produces the RF excitation pulses which provoke the creation of the MR-signal. The MR-signal in turn is measured by the receiver coils. Standard extremity coils and standard head coils were used for the measurements. The choice of the coil depends on the size of the flow model and of the designated field of view (FOV).

- The gradient system is capable of producing spatially and temporally varying magnetic field gradients $\vec{G}$ that are superimposed onto the main magnetic field B_0. Three sets of gradient coils are an inherent part of any MR system and allow the manipulation of the local magnetic field strength in any spatial direction. A powerful gradient system is necessary in order to produce steep magnetic field gradients and thereby enable higher spatial resolution of the MR images.

4.4 Flow models: Fabrication and measurement procedure

The flow models are designed such that they meet the preconditions deployed by the MR-environment. That is:

- No metallic components may be utilized, as they cause signal dropout and measurement artifacts. While paramagnetic (e.g. aluminum, magnesium) and diagmagnetic materials (e.g. copper, carbon) may be used, ferromagnetic components must not be introduced under any circumstances. The components would cause severe measurement artifacts and will experience strong forces, generated from the B_0 main magnetic field.

- Electrical currents should be avoided. The MR signal measured by the receiver coils is weak and sensitive to electrical interference. Electrical currents may cause erroneous measurements. Simultaneously, also the electrical currents (e.g. sensor signals) may suffer from signal degradation through the MR measurement sequence which involves repeated application of strong magnetic field gradients.

Flow models are, to a large extent, made from polyamide (PA2200) by a direct selective laser-sintering (SLS) rapid prototyping technique. Flow models can be designed using CAD software (Siemens PLM Software, NX) and produced in an easy and cost efficient way. Optical access is often provided to enable validation measurement via LDV or to observe the flow situation inside the measurement region. This is realized through perspex inserts. De-aeration of the flow models is an important aspect and is accounted for by various de-aeration cavities.

For the measurement procedure, the flow models are placed inside a perspex pan and aligned with the patient table of the MR scanner. The flow models are secured in a fixed position to prevent measurement errors through unintentional movement and receiver/ transmitter coils are installed on top of the model and tightened to the patient table of the MR scanner. Subsequently, the flow models are connected to the PVC hoses and filled with water and de-aerated.

5 Mean flow measurements inside an engine flow model

This section illustrates the potential of mean flow MRV measurements. Measurements are acquired in a steady flow 1 : 1 scale model of the Engine Test Bench (ETB) described in Sec. 4.1. This model is denoted *engine flow model* in the following. Measurements are validated with the help of PIV measurements, acquired under unsteady flow conditions of the ETB. The ability of MRV to depict volumetric changes in the flow field is demonstrated by two different cylinder head designs. The *wall-guided* (WG) and the *spray-guided* (SG) cylinder head exhibit small geometrical changes, leading to pronounced changes in the flow field.

5.1 Experimental setup

The experimental setup is visualized in Fig. 5.1. The working fluid enters the engine flow model through a diffuser with a total length of 670 mm, which expands the cross section from the supply hoses (25.4 mm) to the diameter of the intake pipe (56.3 mm). The red line in Fig. 5.1 indicates the position where the unmodified geometry of the ETB begins within the engine flow model. The flow enters the cylinder downstream of the bifurcation through two separate intake ports.

The cylinder rotation axis of the engine is tilted at an angle of $\alpha = 63\,^\circ$ towards the diffuser rotation axis (Fig. 5.1 bottom right). The intake valves are tilted at an angle of $\beta = 23\,^\circ$ towards the cylinder rotation axis (Fig. 5.2). The piston does not exist within the engine flow model; the fluid exits through the bottom of the cylinder chamber into a plenum and is then recirculated back to the flow supply system.

Fig. 5.2 shows the cross section of the engine flow model in the center plane of one intake valve ($z = 19\,\text{mm}$, $\zeta = 0\,\text{mm}$) and the intake valves which are

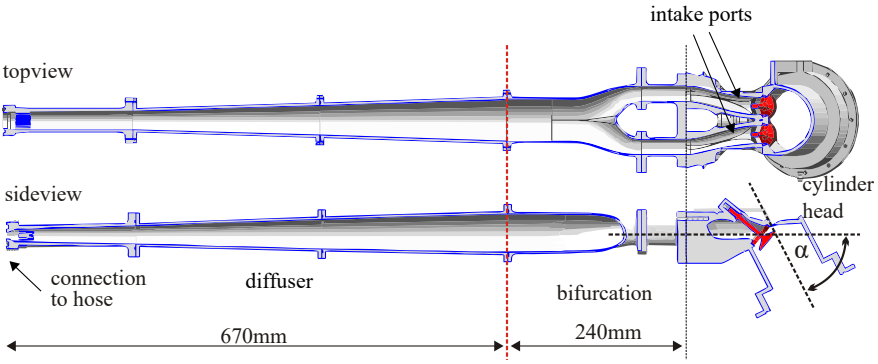

Figure 5.1: Sectional top- and sideview of the engine flow model with diffuser and bifurcation. The *Re* number was calculated using the cross section in the diffuser marked with the red dotted line. Adapted from Freudenhammer et al. [33].

opened $\eta = 9.21\,\text{mm}$ with respect to the closed position. The corresponding crank angle (CA) position is $\lambda = 270\,^\circ$ before Top Dead Center (bTDC) and is also marked via a blue circle in Fig. 6.7, page 73. See Fig. 6.6 for the definition of the crank angle λ. Two coordinate systems are defined in Fig. 5.2. (1) primary xyz-coordinate system positioned in the symmetric-axis of the cylinder and (2) $\xi\eta\zeta$-coordinate system positioned in the symmetric axis of one of the intake valves. The origin for the xyz-system lies at the cylinder axis with $y = 0\,\text{mm}$ where the cylinder geometry meets the pentroof cylinder head, while the $\xi\eta\zeta$-origin lies at the center-axis of the valve shaft with the $+\eta$ direction along the valve shaft towards the inlet port.

5.2 Measurement parameters

A 3D3C measurement volume with a FOV of $240\times140\times128\,\text{mm}^3$ and a spatial resolution of 1 mm (isotropic) is acquired within a time for data acquisition of $t_A = 9\text{min}\,15\text{sec}$. MRV experiments were acquired at a flow rate of 66 L/min. The *Re* number, $Re = 45,000$, was calculated inside the straight intake piping (diameter 56.3 mm, see red dotted line in Fig. 5.1) using the bulk flow velocity and the kinematic viscosity of water at 50 °C, $\nu_{\text{water, }50^\circ\text{C}}$. The *Re* number of the PIV-measurements was estimated to $Re \approx 37,200$. Therefore another set

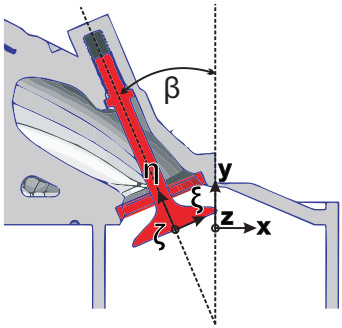

Figure 5.2: Definition of the coordinate systems. Cross-sectional view at $z = 19\,\text{mm}$ through the symmetry-plane of one intake valve.

of MRV-measurements was acquired with a halved flow rate and, consequently, halved Re number of $Re = 22,500$, to show that the Re number had no effect. Important parameters of the MRV measurements are listed in Tab. 5.1.

Fig. 5.3 visualizes the entire FOV, acquired by the MRV measurements by two orthogonal planes, $z = 19\,\text{mm}$ plane (left) and $\xi = 0\,\text{mm}$ plane (right).

Differences ETB and engine flow model Fundamental differences between the engine flow model and the real engine are obvious:

- No piston is included in the engine flow model, instead the steady flow enters the cylinder through both intake channels and leaves the engine flow model through an outlet in the plenum as depicted.
- The intake valves within the engine flow model are in a fixed position.
- No exhaust valves are modeled in the engine flow model.
- The working fluid is incompressible (water), while it is naturally compressible (air) within the ETB. Moreover, a steady flow rate is generated within the engine flow model, while the flow rate inside the ETB is unsteady.

All differences in the operating parameters between the steady flow engine flow model and the unsteady flow ETB are listed in Tab. 5.2.

Table 5.1: Parameters and settings of the MRV measurements

Measurement parameters	
Flow temperature	50 °C
Volumetric flow rate	33; 66 L/min
Re numbers	22500; 45000
Field of View	$240 \times 140 \times 128$ mm^3
Spatial resolution	$1.0 \times 1.0 \times 1.0$ mm^3
Number of vectors	4.2 e6
VENC	1; 2 m/s
Data acq. t_A	9 min 15 sec
Number of repetions (n)	3; 4

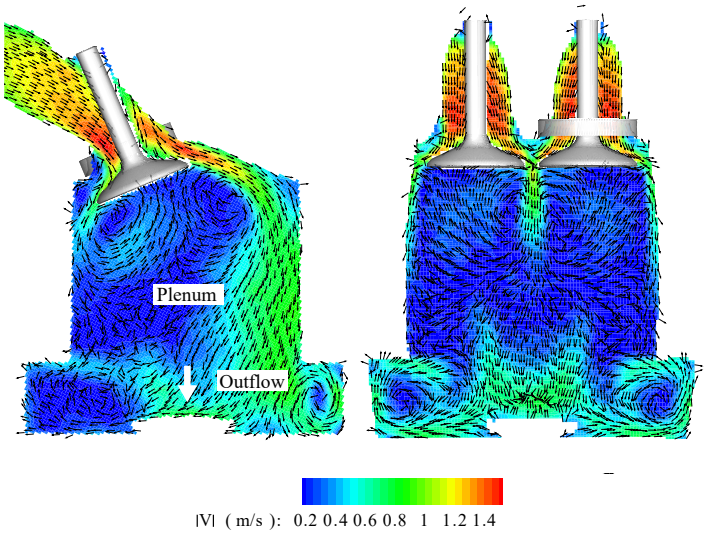

Figure 5.3: Visualization of the entire measurement volume of the MRV measurements. Not the entire measurement volume can be compared to the PIV-data acquired in the real engine flow.

Table 5.2: Differences in operating parameters between the PIV measurements acquired inside the ETB, and MRV measurements acquired within the engine flow model.

	Engine Test Bench (ETB)	Engine flow model
Working fluid	compressible	incompressible
Piston	moving	no piston
Intake valves	moving	fixed
Exhaust valves	closed	closed
Flow situation	unsteady	steady

Determination of valid region for flow comparison Due to the fundamental operating differences, the valid region of the measurement, i.e. the region, where MRV and the corresponding PIV measurements are comparable has to be identified. Therefore, the PIV and MRV data sets were quantitatively compared at different locations within the measurement volume. The grid of locations for comparison is visualized in Fig. 5.4, as well as normalized u and v velocity profiles, extracted along the horizontal line $y = -10\,\mathrm{mm}$ within the mid-valve plane ($z = 19\,\mathrm{mm}$) for both MRV and the PIV measurements. The velocities were normalized using the *Normalization Factor* (NF), which was calculated from the spatially averaged u and v velocity components along the $y = -10\,\mathrm{mm}$ line. The NFs for each of the three data sets ($\mathrm{MRV}_{Re=22,500}$, $\mathrm{MRV}_{Re=45,000}$, PIV) are listed in Tab. 5.3. The trend shows excellent agreement. All three data sets and almost collapses onto one line for both the normalized u- and v-velocity component (Fig. 5.4 solid and dashed lines, respectively).

Figure 5.5 shows the normalized u and v velocities extracted along vertical lines at different x-positions $-30\,\mathrm{mm} \leq \mathrm{x} \leq 30\,\mathrm{mm}$ within the $z = 0\,\mathrm{mm}$. The velocity profiles depicted by both MRV data sets (black and blue lines) show very good agreement, indicating Re number independence within this Re number region ($22,500 \leq Re \leq 45,000$). The agreement between PIV and MRV data sets is good for $y \geq -20\,\mathrm{mm}$. Flow velocities within the engine flow model below this region deviate from the flow velocities in the ETB due to the absence of the piston boundary within the engine flow model. For this

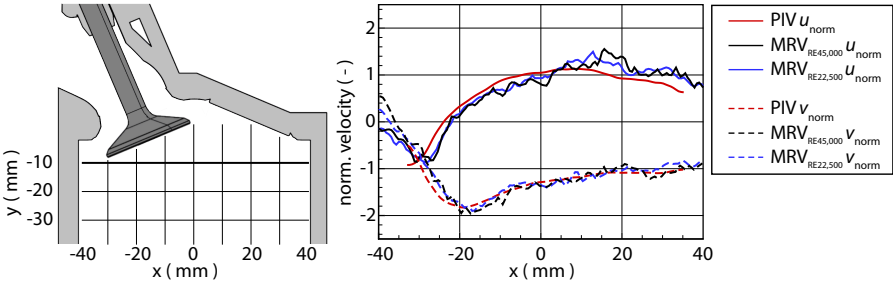

Figure 5.4: Normalized MRV (black and blue lines) and PIV (red lines) velocities for the u- (solid) and v- (dashed) velocity component, extracted along the $y = -10\,\text{mm}$ line.

region, the MRV flow field is not analyzed below $y = -20\,\text{mm}$. This region is shaded gray in Fig. 5.5.

The flow velocities of the MRV measurements can be calculated back to "real engine flow velocities" using the *Scaling Factor* (SF). SF is determined as ratio of the NFs

$$SF_{\text{MRV Re=45,000}} = \frac{NF_{PIV}}{NF_{\text{MRV Re=45,000}}} = 20.64. \tag{5.1}$$

The determined values for the SF are provided in Tab. 5.3.

5.3 Results

Volumetric flow within intake manifold

The volumetric flow is analyzed within the intake manifold to describe the annular flow as it approaches the intake region near the valve head. Figure 5.6 shows contour slices of velocity magnitude at four cross section locations ① to ④ within the intake manifold of the WG cylinder head. Perpendicular views of each contour slice are individually shown on the right side of Figure 5.6. In addition, an iso-surface representing the wake region downstream of the valve stem is shown in Figure 5.6a. This iso-surface is identified as the volume with ξ-velocity $\text{vel}_\xi \leq -0.1\,\text{m/s}$. A negative ξ-velocity within the intake manifold

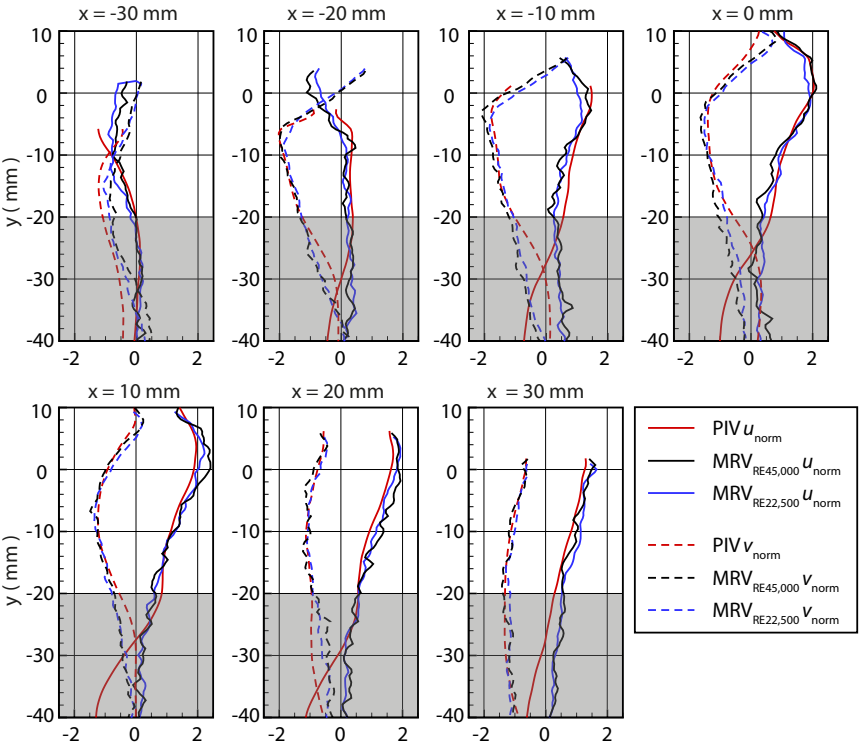

Figure 5.5: Normalized MRV (black and blue lines) and PIV (red lines) velocities for the u- (solid) and v- (dashed) velocity component, extracted along different x-locations inside the cylinder chamber.

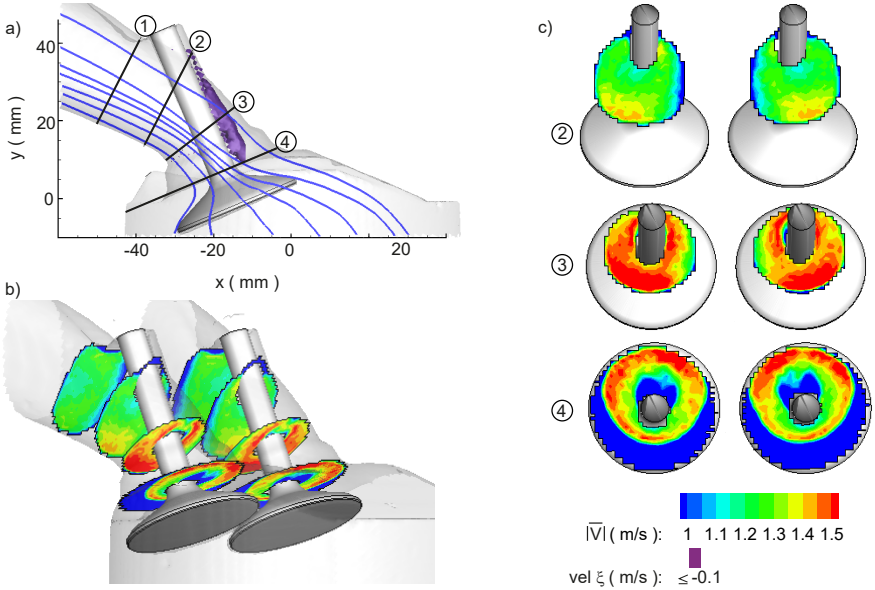

Figure 5.6: Contour slices of velocity magnitude at four cross section locations ① to ④ within the intake channel. a) Streamlines visualize the flow through the valve-gap. A zone of recirculating mass flow is identified just downstream of the valve stem (ξ-velocity ≤ -0.1 m/s). The positions of the four cross section locations are marked. Perpendicular views of each contour slice are individually shown on the right side (c). The velocity magnitude can be scaled to real engine velocity using the SF. Adapted from Freudenhammer et al. [33].

Table 5.3: Spatial-averaged u and v velocity components, averaged along a horizontal line at $y = -10\,\text{mm}$ ($x = -33\,\text{mm}$ to $35\,\text{mm}$, $z = 0\,\text{mm}$). The normalization factors (NF) are calculated from the spatial-averaged u and v velocity components and used to normalize the velocity components.

data set	spat.-avg. u (m/s)	spat.-avg. v (m/s)	NF (m/s)
PIV $_{Re\approx37,200}$	8.29	16.56	12.43
MRV $_{Re=22,500}$	0.20	0.39	0.30
MRV $_{Re=45,000}$	0.42	0.78	0.60
Scaling Factor (SF) PIV/MRV $_{Re=22,500}$			41.70
Scaling Factor (SF) PIV/MRV $_{Re=45,000}$			20.64

is identified as a wake region with a reversed flow. Streamlines are added within Fig. 5.6a to further visualize the flow within the intake manifold and over the intake valves.

Figure 5.6c reveals strikingly symmetric flows within both intake manifolds. At location ① the flow resembles a homogeneous annular velocity distribution and is not individually shown in Fig. 5.6c. At location ②, velocity increases towards the bottom of the contour slice where the flow accelerates due to the vastly approaching reduction in cross sectional area and obstruction of the valve stem. The flow on slice ③ shows the largest velocity magnitudes primarily along the bottom and outer side of the slice. The cross sectional area is the smallest due to the obstruction of the valve stem, and the dual-intake ports begin to merge towards the center cylinder axis. High velocity magnitudes are also shown to travel around the valve stem, but a recirculation zone is located directly behind the valve stem. This recirculation zone exhibits moderate velocity magnitudes (up to 1.3 m/s). At location ④, the velocity magnitude is largest in the upper region where the high velocity magnitude from slice ③ is primarily directed. The lower region exhibits a small ring-like region of high velocities (1.5 m/s) entering the cylinder, but primarily shows a large region of velocities less than 1 m/s.

Geometry Variations

The former results were presented for the WG cylinder head geometry. MRV measurements were also performed for the slightly modified SG cylinder head. The influence of the geometry variations on the volumetric flow field are covered within this section. As mentioned previously, the MRV data will be presented in regions above $y \geq -20\,\text{mm}$. Much below $y = -20\,\text{mm}$, the MRV flow field begins to deviate from the flow field within the ETB due to the absence of the piston boundary.

Flow through the mid-valve plane The flow within the mid-valve tumble plane at $z = 19\,\text{mm}$ is shown in Fig. 5.7. The mid-valve plane is defined as the central x-y plane symmetric about the valve axis (i.e. $z = \pm 19\,\text{mm}$). Fixed length velocity vectors indicate the flow direction; for clearity, every third vector is shown. The velocity magnitude is color coded, it was converted to "real engine velocities" by the SF defined on page 55. For the WG geometry, the flow in the intake manifold is uniformly distributed and aligned parallel with the port. A quasi-steady, uniform annular flow exists within the intake manifold (top-left in Fig. 5.7) which is disrupted by the valve stem and the valve head surface. The flow velocity increases in the periphery of the valve stem as the flow approaches the smaller cross sectional areas of the valve gap.

The flow is disrupted by the valve stem and is accelerated in the vicinity of the valve while approaching the smaller cross section of the valve gap. A majority of the flow is guided by the cylinder head above the valve surface and enters the cylinder at $x \approx 0\,\text{mm}$, $y \approx 5\,\text{mm}$. This flow is entering the cylinder chamber as *overflow*. Definition for the overflow: $\xi > 0\,\text{mm}$, see Fig. 5.2. The high velocity flow (see ①) follows the cylinder head surface and is redirected downwards by the opposing cylinder wall, forming a clockwise vortical motion. On the left side of the image at the back side of the valve, a smaller portion of the flow impinges onto the valve surface and enters the cylinder at $x \approx -30\,\text{mm}$. The flow within this region is identified as the *underflow*.

Upstream of the valve seat, before the underflow is redirected by the valve, the flow separates from the intake port forming a large recirculation zone, at point ②. This recirculation zone extends from the intake port into the cylinder and covers a large area within the valve gap's cross section and leads to the

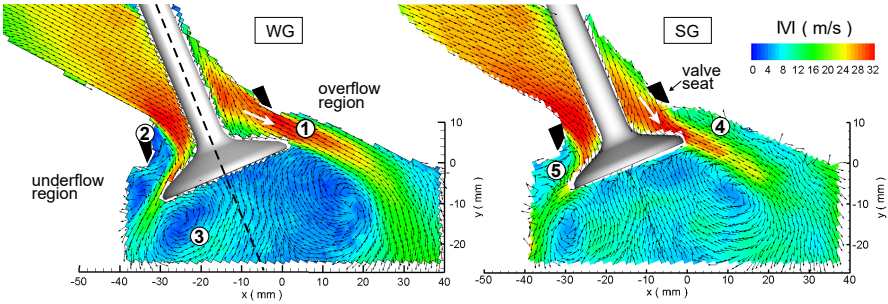

Figure 5.7: Comparison of the mid-valve plane for the SG and WG cylinder head geometry. Tumble-flow plane at mid-valve position ($z = 19\,\text{mm}$) showing the intake flow in the vicinity of the intake valve. Highest flow velocities appear in the valve curtain of the overflow region ($x = 0\,\text{mm}$, $y \approx 10\,\text{mm}$). A recirculation zone exists in the underflow region ($x \leq -25\,\text{mm}$, $y \approx 0\,\text{mm}$) where mass flow is re-entering the inlet-channel up to the valve seat. Velocity vectors (every 3rd vector shown) are displayed with a fixed vector length for better visualizing of the flow topology. The velocity magnitude can be scaled to real-engine velocity using the SF. Adapted from Freudenhammer et al. [30].

high velocity narrow channel flow entering the cylinder along the surface of the valve. The majority of the underflow is redirected by the cylinder liner and forms a counter-clockwise motion below the valve at point ③ while a small portion is redirected upwards into the recirculation zone.

Compared to the flow in the WG geometry, the annular flow in the intake port exhibits higher velocities in the SG geometry Fig. 5.7, right. The mass flow rate in the intake port is identical for both geometries, but the reduced cross-sectional area near the intake valve in the SG geometry is responsible for the higher level of velocities shown in the intake port upstream the valve stem. The overflow in the mid-valve plane is less pronounced for the SG configuration while the underflow is enhanced through higher flow velocities. Two significant flow modifications are found for the SG design directly linked to this observation: ④ The flow separation in the proximity of the valve seat on the overflow side with the corresponding recirculation zone which was not observed for the WG geometry and ⑤ the reduction in size of the recirculation zone within the underflow region. The additional flow separation in the overflow region is a direct consequence of the modified intake port

contour. In the periphery of the valve, the flow is no longer aligned with the intake port and cylinder head geometry as it was for the WG geometry. The intake port flow does not directly align perpendicular to the valve gap as for the WG configuration. Instead, the flow impinges directly onto the valve surface and is then redirected into the cylinder. This situation is illustrated by two white arrows depicting the local flow direction. The flow separates at the valve seat and forms a recirculation zone near the cylinder head at $x > -4\,\mathrm{mm}$. As a consequence, the high velocity flow through the valve gap narrows down and less mass flow enters the cylinder within the overflow region. The high velocity overflow is detached from the cylinder head and does not reach the cylinder wall on the opposite side of the cylinder due to a reduced flow momentum. The flow separation on the underflow side (identified by ⑤) occurs further downstream for the SG geometry. This modifies the flow direction at the valve seat slightly more towards the valve gap compared to the WG geometry. As a result, the recirculation zone is smaller in size.

Flow distribution through valve curtain The valve curtain is defined as the annular area between the valve head and valve seat [46]. For this analysis, the $\xi\eta\zeta$-coordinate system is used, which is positioned in the symmetry axis of the $z = 19\,\mathrm{mm}$ intake valve. Fig. 5.8 shows the radial velocity distribution through the valve curtain, projected on a 2D contour plot. Using the scaling factor SF, the radial velocities are calculated back into velocities that would occur inside the real engine flow of the ETB. The x-axis depicts the azimuth angle Θ around the perimeter of the intake valve with 17.5 mm radius for the WG valves and 15.5 mm for the SG valves. The height of the valve curtain contour is 9.21 mm (i.e. valve lift at $\lambda = 270°$) and is identical for both cylinder heads. Iso contours are shown at 1 mm distance from the valve. This was taken in order to resolve the velocities along the entire valve lift, which was not possible near solid boundaries due to limited spatial resolution.

A positive radial velocity represents a flow entering the cylinder chamber, while a negative radial velocity represents a flow re-entering the valve curtain region from the cylinder chamber (i.e. recirculation zone). A boundary (dotted line) is superimposed onto the iso-contour to identify regions of negative radial velocities. The previously defined overflow and underflow region corresponds to $|\Theta| \leq 90°$ and $|\Theta| > 90°$ respectively.

For the WG configuration, high radial velocities are found in the overflow

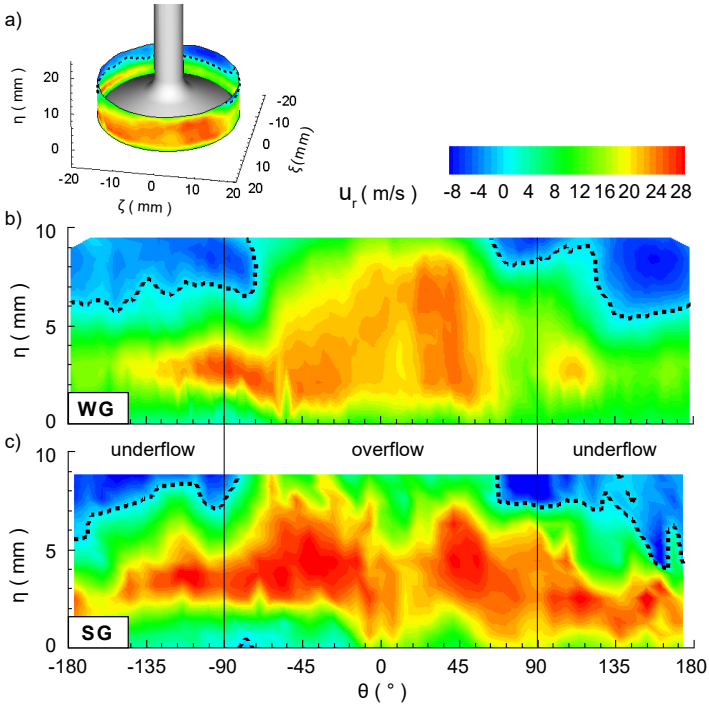

Figure 5.8: a) Annular iso-contour of the valve curtain of the intake valve at $z = 19\,\text{mm}$. The contour shows radial velocity plotted over the valve lift η and the azimuthal angle Θ. A boundary (dotted line) is superimposed onto the iso-contour to identify regions of negative radial velocity. Note distinctive areas of negative radial velocity in the underflow region that consists of flow re-entering the valve curtain region. b) WG cylinder head geometry c) SG cylinder head geometry. Adapted from Freudenhammer et al. [30].

region over the entire height of the valve gap for $-45° \leq \Theta \leq 45°$. The velocities start to decrease beyond $\Theta > 45°$ but high velocities closer to the valve head still exist towards negative Θ values until $\Theta = -130°$. Thus larger flow velocities are shown to exit toward the direction of the nearby cylinder wall (i.e., $\Theta > -90°$), than toward the direction of the adjacent intake valve. Regions of negative velocities are seen at the cylinder head, for $|\Theta| > 90°$, $\eta > 5\,\text{mm}$, identifying the recirculation zone of the underflow region that was discussed in Fig. 5.7.

For the SG configuration, the regions of high radial velocities are more homogeneously distributed over almost the entire circumference. At the same time, the regions of recirculating mass flow are reduced in size. This is expected since the same mass flow enters the cylinder for the SG through an 11.5% smaller valve curtain area. The velocities increase along the perimeter from $\Theta = 0°$ in both directions and peak at $|\Theta| = \pm 45°$. For positive Θ, the high velocity region primarily exists near the valve head together with a larger extension of the recirculation zone at the cylinder head, while for negative Θ values, maximum velocities are found closer to the middle of the valve gap.

5.4 Summary

MRV measurements of the mean flow field within a 1 : 1 scale model of the ETB are presented. Measurements are conducted for a fixed valve lift of $\eta = 9.21\,\text{mm}$ ($\lambda = 270°$), corresponding to a crank angle position during intake stroke (see Fig. 6.6 on page 72 for the defintion of the crank angle λ). Measurements are conducted in water flow, while the PIV validation measurements are acquired in the "real engine flow", i.e. in gaseous, compressible working fluid. A region within the cylinder chamber is identified, where the steady flow MRV measurements can accurately reflect the flow velocities that are present within the unsteady ETB flow during intake stroke.

The volumetric flow field is analyzed within the intake channel and in direct vicinity to the intake valves. A recirculation zone, present in the underflow region during the intake stroke, is identified. The recirculation zone is moreover identified in the valve curtain region, which is defined as the annular area between the valve head and valve seat. Moreover, the possibilities of MRV to resolve changes on the flow topology by geometrical changes of the

cylinder head geometry are presented. The analysis of the volumetric flow distribution through the valve curtain is not possible with present measurement techniques. These measurements enable new insights into the process of cylinder filling during intake stroke.

In conclusion it can be stated that presented mean flow measurements illustrate the high potential of the MR techniques for technical flow field quantification. The examined engine flow model resembles a flow field which is very challenging to quantify by means of conventional measurement techniques. The reasons are the complex flow geometry and the limited optical access. However, MRV measurements enable thorough quantification of the flow field without the need for optical access and without any flow field manipulation. The measurements offer new insights into the volumetric velocity field, unrivaled by conventional measurement techniques in terms of data quantity and data acquisition time.

6 Phase-averaged flow measurements

Phase-averaged MRV measurements of periodic flows are typically known as *4D MRV measurements*, since they enable the acquisition of 3D3C velocity-fields plus time as a fourth dimension. The working principle of 4D MRV measurements, in the following denoted *4D measurements*, is discussed in Sec. 3.3.2. It was emphasized, that no time-resolved measurements of the flow under investigation can be acquired. In fact, the phase-averaged flow data is gradually acquired, which can be conceived like an image that gains in details and precision as acquisition time proceeds. To enable 4D measurements of periodic flows, the measurements must be triggered at the onset of each new cycle. Different mechanisms for trigger generation are reviewed in Sec. 6.1.

Two test cases of 4D measurements are discussed and exemplary flow results are shown in Sec. 6.2 and Sec. 6.3. These test cases exhibit pronounced differences regarding the flow under investigation, the method of trigger generation and the amount of acquired flow data. Measurements were conducted in a modified engine flow model, equipped with periodically actuated intake valves and corresponding modulated flow rate. The secondary test case represents measurements conducted in a naturally periodic flow, i.e. Kármán vortices shedding off a confined cylinder.

6.1 Triggering mechanisms

Various triggering mechanisms are possible for the 4D measurements. A general distinction between *externally imposed trigger* and *internal trigger*, i.e. a trigger created from within the flow, can be made.

The external trigger generation can be applied in a (strictly) periodic flow with a well-known periodic cycle length. Examples for externally triggered 4D measurements can be found in Elkins et al. [25], Markl et al. [57], Wang et al. [78], and Wigström et al. [84].

Several examples for internal trigger generation regarding electrocardiog-

raphy gated (ECG-gated) 4D measurements are reported for clinical applications [11, 53, 58, 59, 84]. This trigger generation from electrical voltage signal is produced by low voltage signals arising from the patient's heartbeat. With the emergence of the MRV techniques for technical flows, trigger generation from other signal sources besides ECG promises new possibilities of flow analysis: Trigger generation from a pressure signal, extracted from within the flow, was recently reported using a PVDF pressure-transducer, positioned inside the FOV [81]. Other possible sources include trigger generation from temperature and/or photo sensors, although studies have yet to be reported in literature. The challenge regarding the internal triggering lies in the generation of a steady trigger signal from the flow under investigation. This is particularly challenging, because of the special circumstances and limitations which have to be considered in MR environment (see Sec. 4.4).

The general procedure for internal trigger generation is sketched in Fig. 6.1. The desired sensor signal (S_F) is measured within the flow model, placed inside the MR scanner during the measurements (blue line). The particular challenges of the MR environment are indicated by the dashed, black box. The received signal data is conditioned and the trigger signal is extracted (red signal train). In Fig. 6.1, the trigger is generated from a "heartbeat-like" signal. After extraction from the measured signal, the trigger is fed back into the MR scanner as a +5V TTL signal. Periodic flow and the MR scanner are now synchronized and the 4D measurements can start.

Fig. 6.1 (bottom right) visualizes a detail of the "trigger train". The phase angles are illustrated as green bins and fill up the cycle. The maximum amount of phase angles fitting into one periodic cycle lies usually in the range of one to several dozen and is, besides the cycle duration (t_D) primarily determined by three factors: Size of the FOV (matrix size, spatial resolution), measurement sequence (type of sequence, echo time TE, repetition time TR) and hardware limitations (MR scanner memory, gradient system and more).

6.2 4D engine flow model

The mean flow MRV measurements of the engine flow model presented in the previous Chapter 5 were extended by 4D measurements, with the objective of investigating the in-cylinder flow during a large portion of the intake stroke.

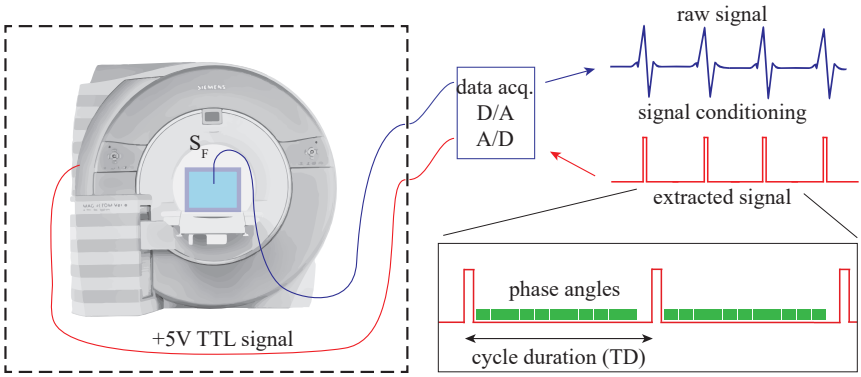

Figure 6.1: Schematic of possible ways of trigger generation to enable 4D measurements.

To enable 4D measurements, the engine flow model had to be adapted. It was equipped with moving intake valves, driven by MR-compatible actuators.

6.2.1 Modified setup

The modified engine flow model is illustrated in Fig. 6.2. The working fluid enters the model through a diffuser which expands the cross section from the supply hoses (25.4mm) to the diameter of the engine intake manifold (56.3mm). The inflow (constant volumetric flow rate of 49 L/min) passes the bypass system, consisting of a rotor-stator arrangement. This system works such that the incoming flow is split up into a radial and an axial component, depending on the rotor position. The rotor position can be altered by the *bypass-cylinder*.

The bypass is in "fully open" position, when there is no remaining flow in axial direction. The working fluid exits the engine flow model through the *bypass outflow* and is recirculated back to the flow supply system.

When the bypass is "fully closed", the entire flow rate is guided through the bifurcation into the cylinder chamber. Honeycombs, placed downstream of the bypass system, remove any swirl of the flow, induced by the rotor-stator arrangement. Any intermediate position of the rotor-stator arrangement is

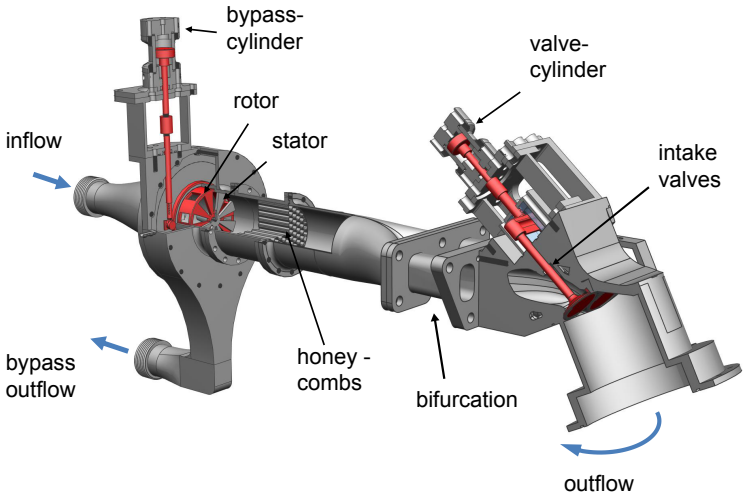

Figure 6.2: Sketch of the engine flow model for 4D flow measurements.

possible.

Downstream of the honeycombs, the geometry of the 4D engine flow model complies to the geometry of the engine flow model described in Chapter 5 (see red dashed line in Fig. 5.1, page 48). The difference lies in the support for the intake valves. These are connected to the *valve-cylinder*, enabling a translational movement of the intake valves and thereby a change in valve lift during the measurements. All moving parts in Fig. 6.2 are colored red, for a better illustration.

Hydraulic actuators The valve- and bypass-cylinder, are self-made MR-compatible hydraulic actuators. Hydraulic actuation was chosen for its versatility and unproblematic application. Fig. 6.3 shows a sectional view of one actuator, made exclusively from plastic material (rod - PMMA, body - PA, sealings - PP). The design of the actuators was adapted according to their purpose. The maximum stroke was set to 9.5 mm for the valve-cylinder[1] and

[1] corresponding to the maximum valve lift of the intake valves

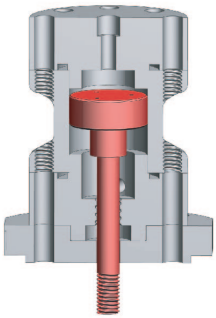

Figure 6.3: Sectional view of the hydraulic actuator made merely from plastic material.

14.7 mm for the bypass-cylinder. This is the travel between the bypass "open" and "closed" position.

Hydraulic supply system A photograph of the hydraulic supply system, used to operate the hydraulic actuators, is shown in Fig. 6.4. The system consists of two individual hydraulic circuits to operate both hydraulic actuators individually. The internal gear pumps (*IPZ1-HR-3* and *IPZ1-HR5* models, *Jung-Fluidtechnik GmbH, Germany*) are driven by brushless direct current (BLDC) motors (*ROXXY BL Outrunner 4260/06, Robbe*). The BLDC motors feature high torque output and high dynamic response and are used to directly control the flow rate of the hydraulic circuit through a modulation of the motor speed. Hydraulic oil (H*LP22, Liqui Moly*) is used as working fluid and stored in 250 ml oil tanks. The total pressure is measured by pressure sensors (*Wika EN837-1*). Pressure relief valves open, when the pressure inside the hydraulic tubes exceeds ≈ 8 bar, thereby preventing damage to the system in case of incorrect operation. The oil is guided to the 4/2 directional control valves (custom made), operated by high-voltage servo motors (*HBS 770 BB MG, Graupner*). Two hydraulic pipes (≈ 5 m in length) lead into the scanner room and connect the hydraulic system with the bypass- and valve-cylinder of the flow model. The reverse current of hydraulic oil is filtered and recirculated into the oil-tanks. Both 4/2 directional control valves and both pumps are controlled via pulse-width modulation (PWM) signals, which are gen-

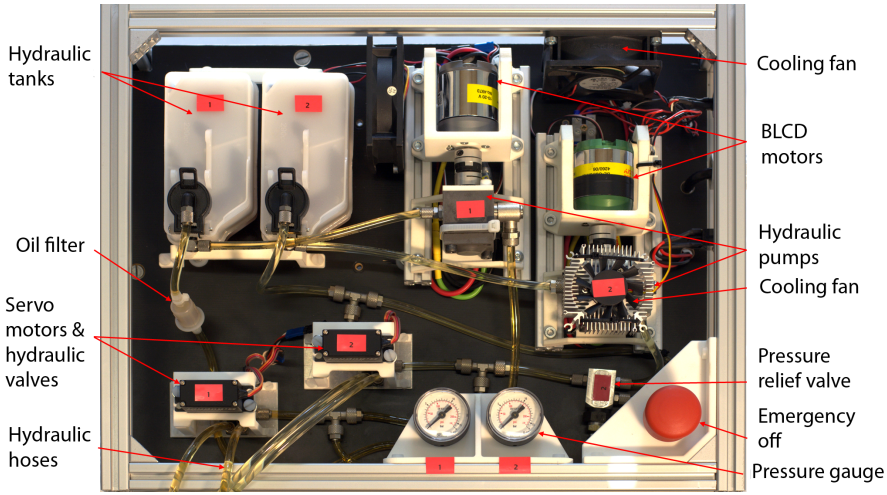

Figure 6.4: Photograph of the hydraulic supply system used to operate the hydraulic actuators. The system consists of two individual hydraulic circuits, each consisting of an oil tank, oil pump operated by brushless outrunner-motors, oil-filter and 4/2-valve operated by servo-motors. Cooling fans prevent the system from overheating during long periods of operation.

erated and controlled via a purpose-made LabView® program. The PWM signal output is produced via an *Arduino UNO* microcontroller board that enables straightforward generation of up to 6 PWM signals simultaneously. Using PWM signals, the servo-motors can realize a change in flow direction in < 80 ms. A strong increase of the working fluid temperature would influence the oil's material properties and influence the working characteristic of the hydraulic system. Therefore, a total of three cooling fans are installed in the system in order to remain the temperature of the internal gear pumps at a moderate level during longer operating periods.

A schematic of the entire experimental setup is visualized in Fig. 6.5. Blue lines indicate the water circuit. Orange lines indicate the hydraulic circuit. Flow control of both circuits is realized by a purpose made LabView® program. The 4D engine flow model and MR-compatible hydraulic actuators are placed within the measurement section inside the MR scanner. The +5V-TTL triggering signal, necessary for acquiring the 4D measurements, enters the

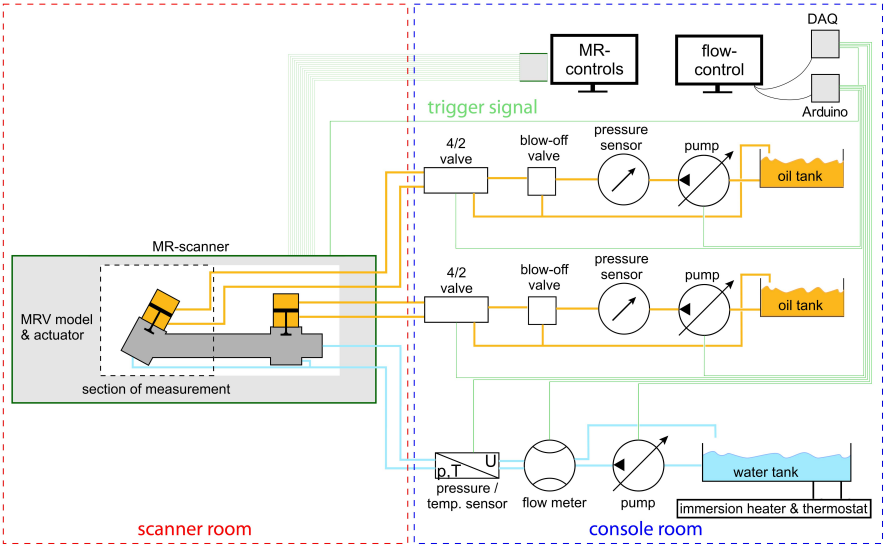

Figure 6.5: Schematic of the experimental setup for 4D measurements of the engine flow model. The two hydraulic circuits (visualized in orange lines) can be individually controlled in order to produce a modulation of the main water flow (blue lines) and thereby imitate a large portion of the intake stroke of a modern four-stroke IC engine.

scanner room as MR scanner input (green line).

6.2.2 Kinematic modeling

The objective of using the hydraulic setup and the hydraulic actuators is to imitate a large portion of the intake stroke of the four-stroke IC engine. Since the working fluids of the Engine Test Bench (ETB) (air) and the 4D engine flow model (water) differ considerably in terms of their physical characteristics, modeling of the valve lift motion has to be performed in order to ensure equivalent flow characteristics.

Valve timing

The speed of the ETB is $n = 800\,\mathrm{rpm}$. The total valve movement duration T_r of the original engine accounts for 270° of one cycle (i.e. 330°–600°, see Fig. 6.7), which corresponds to

$$t_r \approx \frac{1}{n} \times \frac{600° - 330°}{360°} = 56.3\,\mathrm{ms} \tag{6.1}$$

when assuming constant engine speed throughout the cycle.

To ensure comparability between the real engine flow and the flow inside the engine flow model, Reynolds number Re and Strouhal numbers St of both flows are kept constant:

The Re number calculated inside the real engine flow (Re_r) matches the flow model equivalent (Re_m), thus

$$Re_r = \frac{u_r \times d_r}{\nu_{\mathrm{air}}} = \frac{u_m \times d_m}{\nu_{\mathrm{water}}} = Re_m, \tag{6.2}$$

where u denotes the flow velocity, d defines a characteristic length and ν is the kinematic viscosity. The flow model is a 1 : 1 scale replica of the real engine, therefore $d_m = d_r$ applies. The kinematic viscosities for water and air (ν_{water}, ν_{air}) are listed in Tab. 6.1. The working fluid of the model was heated to 55° C, to increase the Re number.

Moreover, the Strouhal number (St) is kept constant, ensuring equivalent kinematics of the valve movement corresponding to the different flow conditions:

$$St_r = \frac{f_r \times d_r}{u_r} = \frac{f_m \times d_m}{u_m} = St_m, \tag{6.3}$$

where f is the characteristic frequency; in this case the frequency of the valve lift motion. Combination of Eq. 6.2 and Eq. 6.3 yields

$$f_m = f_r \frac{\nu_{water}}{\nu_{air}}, \tag{6.4}$$

which describes the required frequency of the models valve lift kinematics as function of the ratio of the kinematic viscosities and the frequency of the real

Table 6.1: Main Parameters of the motored engine and the 4D engine flow model.

		Engine Test Bench	4D Engine flow model
Working fluid		air	water
Fluid temp. (T_F)	(°C)	22.8	55
Kin. viscosity $\nu(T_F)$	(10^{-7}m^2/s)	153.2	5.51
Speed (n)	(min^{-1})	800	28.7
Valve duration t_r, t_m	(ms)	56.3	1563.9

engine f_r . For the engine speed of $n = 800\,\text{rpm}$, this yields a corresponding "model engine speed" of $n_{\text{model}} = 28.77\,\text{rpm}$.

The equivalent valve movement duration t_m of the engine flow model is calculated to be

$$t_m = t_r \frac{\nu_{air}}{\nu_{water}} = 1563.9\,\text{ms}. \tag{6.5}$$

The hydraulically actuated valve movement with a maximum valve lift of $\eta = 9.5\,\text{mm}$ must thus be realized within roughly 1.5 s. The secondary hydraulic circuit, actuating the *bypass cylinder*, must modulate the water flow rate such that it reflects the flow rate naturally entering the cylinder by the provoked downward-motion of the piston within the same period of time.

Interaction of valve lift motion and piston position

For a better understanding of the definition of piston crank-angle (CA) degree and the valve lift, a sketch of the ETB is provided in Fig. 6.6. Displayed is the piston within the cylinder chamber, which changes its vertical position depending on the CA-degree λ of the crank shaft. λ is counted in "degrees before Top Dead Center", which corresponds to the position of maximum piston elevation.

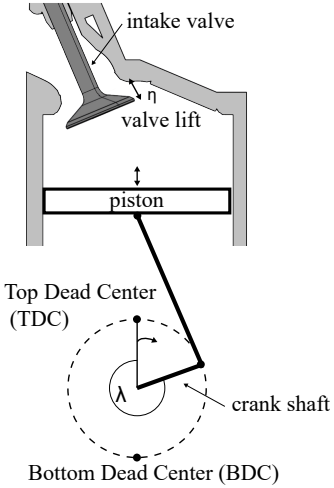

Figure 6.6: The correlation of the CA λ bTDC and the piston movement is schematically depicted. The valve lift motion is a function of the CA, as visualized in Fig. 6.7. Note: Sketch not to scale.

Fig. 6.7 demonstrates the interaction between the valve lift and the crank-angle λ of the ETB. Depicted is the lift of the intake and exhaust valves (solid and dashed line, respectively), plotted against λ. The CA position and valve lift of the mean flow measurements (Chapter 5) is depicted by the blue circle.

Exhaust stroke A section of the exhaust stroke is visualized, lasting until $\lambda = 360°$. During the exhaust stroke, the piston is in an upward motion until it reaches Top Dead Center (TDC) position, equivalent to $\lambda = 360°$. During the last portion of the exhaust stroke, the intake and exhaust valves are both partially opened, from $390° \geq \lambda \geq 330°$. The CA position of $\lambda = 360°$ also corresponds to the onset of the intake stroke.

Intake stroke The intake stroke is defined as the CA region, when the piston performs a downward motion, starting from the TDC position until it reaches Bottom Dead Center, i.e. the region $360° \geq \lambda \geq 180°$. The intake valves open at $\lambda = 390°$ while the piston is still in an upward motion, i.e. during the exhaust stroke and before the onset of the intake stroke. The

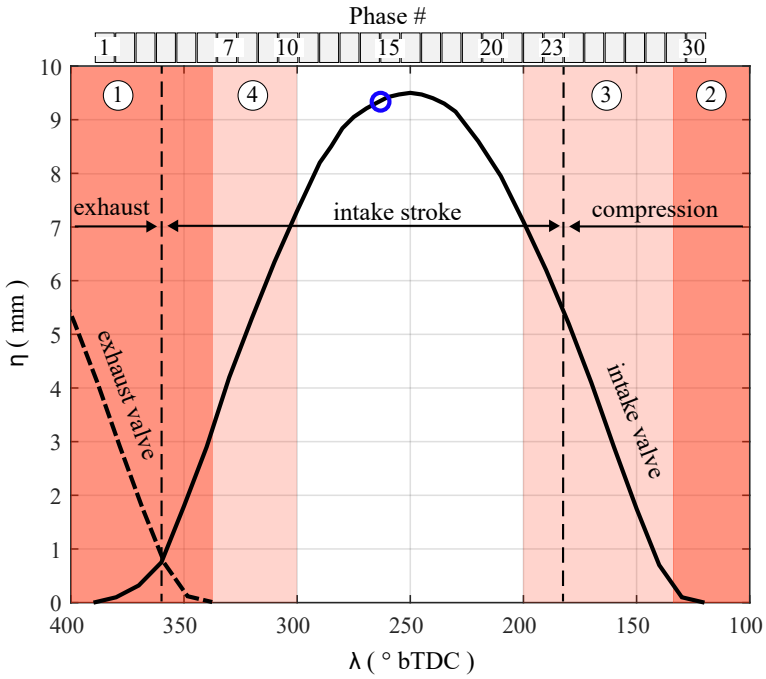

Figure 6.7: Lift of intake (solid line) and exhaust valve (dashed line) plotted against the crank angle (CA) of the four-stroke Engine Test Bench.

Table 6.2: Engine Test Bench CA positions for valve timing.

Intake valve open (IVO)	390	°bTDC
Intake valve close (IVC)	120	°bTDC
Exhaust valve close (EVC)	340	°bTDC
Maximum valve lift (IV)	9.5	mm
at position	250	°bTDC
Prior steady flow meas.	270	°bTDC
corr. valve lift	9.2	mm

valve lift of the intake valves continually grows, while the piston performs the downward motion and thereby provokes the induction flow. The intake valves reach the maximum lift of 9.5 mm at $\lambda = 250°$, then start the closing motion. At $\lambda = 180°$, inversion of the piston motion direction takes place and the intake stroke ends.

Compression stroke The intake stroke is followed by the compression stroke. During the first portion of the compression stroke, the intake valves are still partially opened, i.e. during $180° \geq \lambda \geq 120°$. Due to inertia forces, flow is still entering the cylinder chamber and contributes to increased cylinder loading, despite the fact that the compression stroke has already initiated. Exact numbers for the valve-timings are supplied in Tab. 6.2.

6.2.3 Validation of the MRV data

The MRV data is validated by means of PIV data that was acquired within the ETB. The CA region which can be represented by the 4D engine flow measurements is identified in the following section. The method for quantitative comparison of PIV and MRV data is explained starting from page 76.

Determination of valid CA region for flow comparison

The region of interest for the 4D measurements is limited to a portion of the intake stroke for the following reasons:

- No exhaust valves are modeled within the engine flow model. Therefore only those CA positions can be imitated by the engine flow model

where the exhaust valves are fully closed. With respect to Fig. 6.7, this prediction does not apply to the red shaded region ①.

- Compressibility effects occur within the ETB because of two reasons: Compression due to the Mach number (Ma) of flow $Ma > 0.3$ and compression or expansion due to the piston motion. It was shown in Freudenhammer et al. [33] that the maximum occurring Mach number during intake stroke does not exceed $Ma \approx 0.073 \ll 0.3$. The flow can therefore be assumed incompressible during the entire intake stroke. The imitation of compressibility effects that occur during compression stroke is not possible due to the incompressible working fluid water. While the onset of noteworthy compression effects cannot be related to a distinct CA position, it is assumed that these effects will emerge before the intake valves are completely closed. The red shaded area ② can therefore not be represented by the 4D engine flow model.

- No piston is modeled within the 4D engine flow model. Instead, the working fluid is guided into a plenum after entering the cylinder chamber. It is not redirected by a piston surface. The flow redirection is negligible while the piston is in a downward motion. However, the effect becomes significant, when the piston motion stops and is reversed (at $\lambda = 180°$ CA position). Moreover, quantitative comparison with time-resolved PIV data exhibited considerable flow deviations at CA positions before $\lambda = 180°$, when the downward motion of the piston as a moving boundary, is significantly reduced in speed. No hard CA threshold for valid/non-valid data can be stated either, since the validity is heavily dependent on the considered location within the cylinder chamber. That is why the flow in direct vicinity of the intake valves is less influenced by reversed piston motion than regions further downstream within the cylinder chamber (see light red shaded region ③ in Fig. 6.7).

- The piston of the ETB causes considerable flow redirection during the initial phase of the intake stroke due to the CA position close to Top Dead Center. As no piston is modeled in the engine flow model, deviations in flow topology are expected and must be considered for the flow data within the light red shaded region ④ in Fig. 6.7.

The mentioned restrictions highlight the simplifications of the 4D engine flow model in contrast to the real engine flow, as they diminish the prospective CA region for comparison of MRV and PIV data. While the red shaded regions within Fig. 6.7 are definite constraints, the constraints of validity indicated by the light red shaded regions mainly depend on the position location within the flow regime (i.e. the cylinder chamber) that is observed.

Quantitative comparison of the MRV data

Scaling of flow velocities The Normalization Factor (NF) and Scaling Factor (SF), used in order to bring MRV- and PIV flow data to a common ground for comparison, were introduced in the former section (see page 51). For the 4D measurements the SF was determined to

$$SF_{\,\text{4D MRV}} = 59.61. \tag{6.6}$$

Using the SF, the velocities within the MRV flow model can be converted to velocities that would occur inside a real engine flow. The *normalized velocity* fields are the basis for the following comparison.

Fig. 6.8,(left) shows the locations within the cylinder along which PIV and MRV data sets were quantitatively compared. Fig. 6.8,(right) depicts, exemplary, the velocity components u_{norm} and v_{norm} extracted along $y = -20\,\text{mm}$.

Correlation Coefficient $\gamma_{\text{MRV,PIV}}$ The velocities are extracted from both data sets in order to compare the flow topology and verify whether the behavior of the phase-averaged MRV data is similar to the behavior of the ensemble averaged PIV data along the specified line. This is done by calculating the *Pearson's correlation coefficient*, which is defined as

$$\gamma_{\text{XY}} = \frac{\sum(x_i - \bar{x}) \times (y_i - \bar{y})}{\sqrt{\sum(x_i - \bar{x})^2} \times \sqrt{\sum(y_i - \bar{y})^2}}, \tag{6.7}$$

for the exemplary two different data sets "x" and "y" [76]. A perfect correlation of both data sets would yield $\gamma_{\text{XY}} = 1$, whereas uncorrelated data would yield $\gamma_{\text{XY}} = 0$ and a perfectly negative correlation yields $\gamma_{\text{XY}} = -1$. The correlation coefficients are calculated using the normalized u and v velocities of

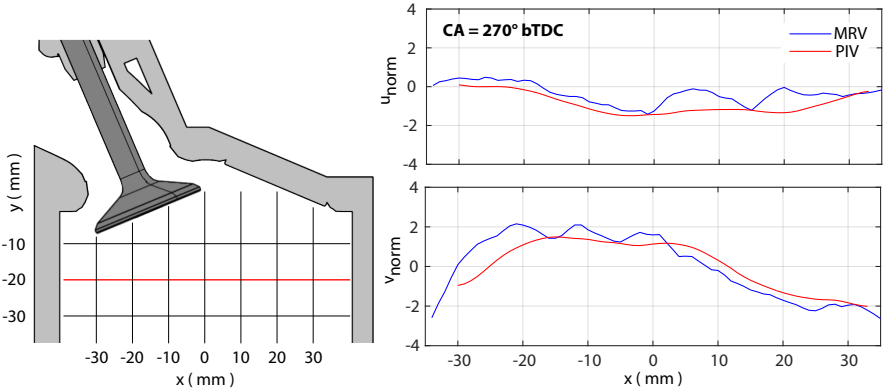

Figure 6.8: Left: Visualization of the locations along which MRV and PIV data sets were compared within the cylinder chamber. Right: Plot of normalized u- (top) and v-velocities (bottom) for the MRV and PIV data set. The velocities were extracted along the $y = -20\,\text{mm}$ line, indicated by a red line color within the cylinder grid.

the MRV and PIV data set. For the normalized u- and v-velocities depicted in Fig. 6.8(right), the coefficients are calculated to be $\gamma_{\text{MRV,PIV}} = 0.82$ and $\gamma_{\text{MRV,PIV}} = 0.98$, respectively.

Despite a high correlation factor $\gamma_{\text{MRV,PIV}}$, i.e. similar flow behavior, flows can depict considerably different trends. Fig. 6.9 illustrates such a situation. Visualized is u_{norm} at $\lambda = 330°$, extracted along the line $x = -30\,\text{mm}$ within the cylinder chamber. Blue and red lines depict the extracted normalized velocities of the PIV and MRV data sets, respectively. The normalized velocities are almost perfectly correlated, but have opposite flow directions.[2] The correlation coefficient ($\gamma_{\text{MRV,PIV}}$) by itself would indicate an erroneous, almost perfect correlation.

The *Directional Correlation Coefficient* (γ_D) is introduced in order to identify regions of opposing flow directions and, in that case, correct the correlation coefficient γ_{xy} accordingly. γ_D is determined as the fraction of MRV and PIV data points along an extracted line with the same algebraic sign

[2]This situation can for example occur for flow, impinging onto the piston surface within the ETB, while the flow within the 4D engine flow model enters the plenum without any piston surface present.

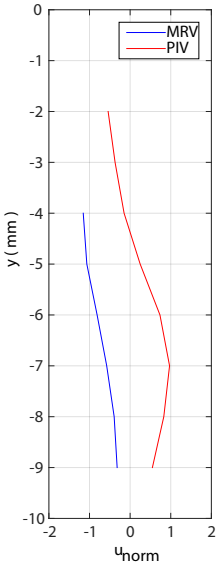

Figure 6.9: Normalized u velocities at $x = -30\,\text{mm}$, crank angle $-330°$ bTDC for the MRV (blue line) and PIV (red line) data set.

compared to the total number of datapoints. $\gamma_D = 1$ indicates matching flow directions from PIV and MRV measurements for all points along the line of extracted velocities. $\gamma_D = 0$ indicates opposing flow velocity directions along the entire extracted line. The Pearson's correlation coefficient is multiplied by the directional correlation coefficent, yielding the expression for the new correlation coefficient $\gamma'_{\mathrm{MRV,PIV}}$:

$$\gamma'_{\mathrm{MRV,PIV}} = \gamma_{\mathrm{MRV,PIV}} \times \gamma_D. \tag{6.8}$$

The such calculated correlation coefficient $\gamma'_{\mathrm{MRV,PIV}}$ for the flow profiles visualized in Fig. 6.8, is provided in Tab. 6.3.

Root Mean Square Deviation Moreover, it is possible to quantify the relative deviation in magnitudes between both normalized data sets by calculating the *Root Mean Square Deviation* (*RMSD*) Sclove [75]:

$$RMSD, \hat{\sigma}(x) = \sqrt{\frac{\sum_{i=1}^{n} \left((x_t)_i - x_i\right)^2}{n}}, \tag{6.9}$$

where, x_t denotes the elements of the PIV data set (true data) and x the elements of the MRV data set (test data). A higher value signifies a larger deviation of the data from the true value. The calculated RMSD value for the flow profiles visualized in Fig. 6.8, is provided in Tab. 6.3.

Preconditions for validity The MRV data is considered valid only if the following two conditions are met:[3]

$\gamma'_{\mathrm{MRV,PIV}}$	>0.4
$\hat{\sigma}$	<1

$\gamma'_{\mathrm{MRV,PIV}}$ and $\hat{\sigma}$ were calculated for the velocities extracted along the lines indicated by Fig. 6.8 and for the 16 phase angles (#7 to #23) that were

[3] Note, that these conditions do not reflect physical limits. The conditions were set up after calculation of $\gamma'_{\mathrm{MRV,PIV}}$ and $\hat{\sigma}$ for the velocities extracted along the lines indicated by Fig. 6.8 and for all 30 phase angles. The values given here are "best guess" assumptions.

Table 6.3: Comparison of correlation coefficients for the normalized velocities extracted along $y = -20\,\text{mm}$, see Fig. 6.8.

	$\gamma_{\text{MRV,PIV}}$	γ_D	$\gamma'_{\text{MRV,PIV}}$	$\hat{\sigma}$
u_{norm}	0.82	0.96	0.78	0.46
v_{norm}	0.98	0.97	0.95	0.64

previously identified valid. The normalized velocity profiles, extracted along the line at $y = -20\,\text{mm}$ for $\lambda = 270°$ are shown in Fig. 6.8. MRV and PIV profiles show general good agreement, which is also represented by the values for $\gamma'_{\text{MRV,PIV}}$ and $\hat{\sigma}$ (Tab. 6.3). The two conditions stated above are met.

Predicting a valid flow region within cylinder chamber The calculated values $\gamma'_{\text{MRV,PIV}}$ and $\hat{\sigma}$ can be used to identify a region of valid field data for every phase angle of the 4D measurements.

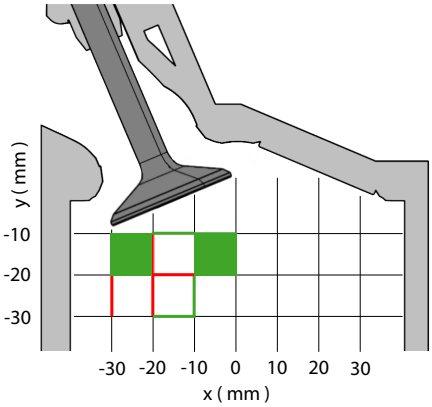

Figure 6.10: Demonstration of the identification of valid flow regions. Green lines represent sections where the acceptability condition is met. Red lines represent regions where it is not met. Colored areas represent valid regions of flow data.

Fig. 6.10 displays an exemplary result for the determination of a valid flow region for every phase angle of the 4D measurements. The flow field is subdivided using grid with 10 mm edge length. Each edge is separately analyzed

Table 6.4: Parameters and settings of the 4D MRV engine flow model measurements.

Flow parameters		Imaging parameters	
Main flow rate (V_m)	19.5 L/min	VENC	1.5 m/s
Main flow temp. (T_m)	50°C	Echo Time (TE)	3.715 ms
Re	45,000	Flip angle	15°
		Matrix size	$100 \times 160 \times 196$
		Voxel size	$1.56 \times 1.56 \times 1.6\,\text{mm}^3$
Flow model parameters		No. of phase angles	30
Cylinder head	SG	Phase resolution (t_{res})	52.0 ms
Valve diameter	29 mm	Cycle duration (t_D)	1566 ms
		Data acquisition (t_A)	54 min 05 sec
		No. of acquisitions (N)	2

with respect to the validity condition by calculating $\gamma'_{\text{MRV,PIV}}$ and $\hat{\sigma}$. Each region, surrounded by at least three valid edges is considered valid. This is depicted in Fig. 6.10 by the green shaded area. All other areas are considered invalid.

6.2.4 Results

4D measurements were acquired with a phase resolution of 30 phases per cycle, corresponding to a temporal resolution of 52.0 ms (cycle duration $t_D = 1566\,\text{ms} \equiv$ valve duration t_m). One flow-on and one flow-off measurement was acquired and subsequently subtracted. Data acquisition for each measurement took roughly 55 min for the acquisition of a volume with matrix size of $100 \times 160 \times 196$ data points, a spatial resolution of 1.6 mm (isotropic) and a resulting total number of $\approx 282 \times 10^6$ velocity vectors. Important measurement and flow parameters are also listed in Tab. 6.4.

Evolution of the flow in mid-valve plane

The evolution of the intake flow within the mid-valve plane ($z = 19\,\text{mm}$) is depicted in Fig. 6.11. Visualized is the velocity magnitude of the in-cylinder

flow for six phase angles. The valid flow region within the cylinder chamber, determined with the validity condition defined above, is exemplary depicted for the 269.1° bTDC CA position, Fig. 6.11c.

Fig. 6.11a depicts the intake flow at a CA position of 334.2°bTDC (phase #7), which was previously defined as one of the first "valid" phase angles. The valve is performing the opening-motion (valve lift $\eta \approx 3.5\,\mathrm{mm}$). The grey shaded area illustrates the position of the piston within the ETB. Due to the close proximity of the piston to the pent-roof of the cylinder, the flow in the ETB is deflected by the cylinder surface shortly after entering into the cylinder chamber. However, the flow into the cylinder through the valve curtain (following section) might not be affected by this issue. The flow within the intake channel is homogeneously distributed with moderate flow velocities of velocity magnitude $|V| \approx 0.3\,\mathrm{m/s}$.

The valve lift is increased to $\approx 7\,\mathrm{mm}$. and the piston location has changed for the $\lambda = 297.0°$ CA position (Fig. 6.11b, phase #11). Both valve movement and piston movement are in the region of maximum displacement-velocities, such that no influence of the piston on the flow field is expected. The flow within the intake channel is still homogeneous. Smaller regions of higher flow velocities ($|V| \approx 0.5\,\mathrm{m/s}$) are depicted in the overflow region ① and in the underflow region close to the valve seat ②. Moreover, a small recirculation region of visible in the underflow region ③.

Fig. 6.11c depicts phase #14 for $\lambda = 269.1°$. This CA position almost corresponds to the location, where the mean flow measurements were acquired (270°bTDC CA position). Comparison of the flow field topology with the corresponding situation for the mean flow measurements (Fig. 5.7, bottom on page 57) shows good agreement between both data sets.

At phase #16, the maximum valve lift ($\eta = 9.5\,\mathrm{mm}$) is reached and the closing of the intake valves starts, while the piston is still in the downward motion ($\lambda = 250.5°$). Maximum flow velocities in the order of $|V| \approx 0.7\,\mathrm{m/s}$ are present in the overflow region and within the intake channel. The recirculating mass flow already identified for phase #11 is pronounced.

The overall level of intake flow velocities is reduced in Fig. 6.11e (phase #20 , $\lambda = 213.3°$) and the valve lift is reduced to ($\eta \approx 8\,\mathrm{mm}$). The closing of the intake valves is apparent for the representation in phase #23 with a remaining valve lift of $\eta \approx 6\,\mathrm{mm}$. The corresponding CA position in the real engine flow is $\lambda = 185.4°$ CA position, i.e. the intake stroke has almost ended

(Fig. 6.11f). Flow velocites are clearly reduced and the recirculation zone in the underflow region is no longer present.

Evolution of the flow through the valve curtain during intake stroke

The volumetric flow distribution within the valve curtain region measured by the MRV mean flow measurements [33, 34] was considered a valuable finding, since no other measurement technique is able to resolve the flow within this region. The recirculation regions identified (see Sec. 5.3) were suspected but have not been visualized before. Within this section the valve curtain flow is presented for the 4D measurements.

Fig. 6.12 depicts the evolution of the flow through the valve curtain region via four distinct time-steps during the valve lift motion, similar to Fig. 5.8, page 59. Visualized are radial flow velocities u_r, red color indicates high radial velocities (i.e. flow entering into the cylinder chamber) while blue colors indicates a recirculating flow with negative radial velocities (i.e. mass flow re-entering the intake channel during the intake stroke).

Fig. 6.12a displays the flow condition during phase #7 for a CA position of $\lambda = 334.2°$ bTDC. The valve is performing the opening-motion (valve lift $\eta \approx 3.5\,mm$). An overall uniform distribution of radial velocities is depicted.

At phase #11 ($\lambda = 297°$) the flow is still characterized by an almost homogeneous distribution of the radial velocity over the valve curtain. Regions of slightly increased radial velocities are indicated for $|\theta| \approx 50°$, ①. The contour plot moreover visualizes regions of negative radial velocities in the upper region for $|\theta| \geq 100°$, which depict the onset of the recirculation zone identified before within the mid-valve plane (Fig. 6.11b).

The recirculation zone ④ has clearly grown in phase #16. Also the high speed regions are much more pronounced, as they reach radial velocities of $u_r \approx 0.5\,\mathrm{m/s}$, ②. A region of lower radial velocities at $\theta \approx 0°$, ③ was identified before and is caused by the wake of the cylinder stem. The general flow topology remains similar between phases #16 and #23. However, regions of high radial velocity are visible over almost the entire circumference ($\eta = 5\,\mathrm{mm}$) with radial velocities in the order of $u_r = 0.5\,\mathrm{m/s}$ in phase #16, while these regions are significantly reduced in size at phase #23 and merely two isolated regions of high radial velocities can be identified at $\eta \approx 7\,\mathrm{mm}$, $\theta =$

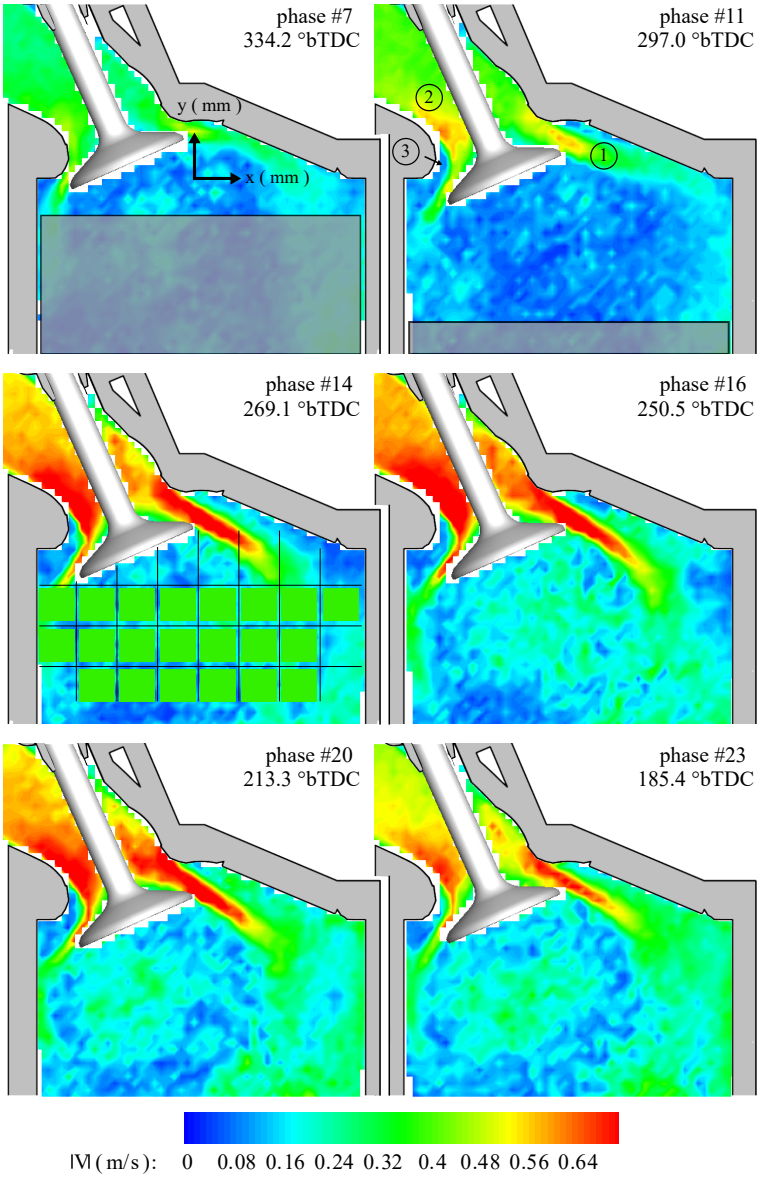

Figure 6.11: Contour plot of the flow velocity magnitude $|V|$ during intake stroke, displayed for six distinct phase angles. The position of the piston within the "real engine flow" is depicted as gray shaded area.

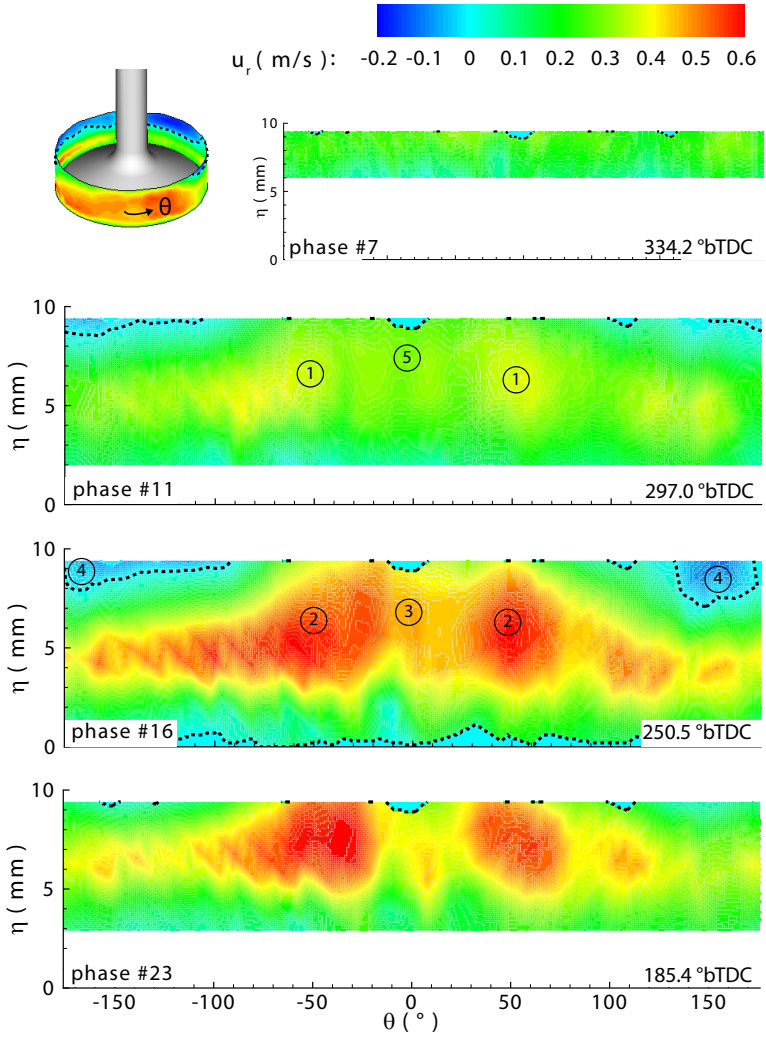

Figure 6.12: Radial velocities through the valve curtain region, displayed for four different phase angles throughout the valve lift motion.

$-50°$ and $\eta \approx 7\,\text{mm}$, $\theta = 50°$, respectively. No regions of recirculating flow are present in phase #23 as was already identified from the mid-valve plane flow field. The small region of apparent zero flow velocity ⑤ ($\theta = 0°$, $\eta \approx 9\,\text{mm}$) present in every phase throughout the valve lift sequence is considered presumably erroneous flow data and therefore neglected.[4]

Via the previously defined Scaling Factor (SF= 59.61), these velocities can be calculated back into "real engine velocities". The corresponding maximum "real engine velocities lie in the order of $u_{r,real} = 29.8\,\text{m/s}$. These velocities lie in the same order of magnitude as the corresponding determined radial velocities for the mean-flow engine testcase (see page 59) and are therefore considered reasonable.

6.3 Von Kármán Vortex Street

4D measurements of a Kármán Vortex Street (KVS), which resembles a naturally periodic flow of vortices shedding from a cylinder were acquired. The KVS is well-known and well documented. An overview about important effects and parameters over a large *Re* number range is given in Zdravkovich [87]. The uniform shedding frequency, made dimensionless by using the Strouhal number, is exploited in technical devices, such as vortex flow meters. The measurements presented in the following exploit the secondary introduced triggering principle, i.e. the *internal triggering* principle.

6.3.1 Experimental setup

A schematic of the experimental setup is shown in Fig. 6.13. The flow model is placed within the MR scanner and connected to two individual flow supply systems with 25.4mm flexible PVC hoses.

The main flow supply system provides a flow rate of $V_m = 19.5\,\text{L/min}$ at a temperature of $T_m = 55°\,\text{C}$, denoted *heated main flow*. The flow enters the test section through the diffuser section and passes by the measurement section (dashed frame) from where it is recirculated back to the flow supply system. A secondary flow rate of $V_c = 15\,\text{L/min}$ is supplied by a recirculating cooler (*Julabo FC1200T*) which maintains the temperature of this circuit at

[4] This flow pattern can not be physically explained and is rather caused by a conversion error when projecting the cylindrical valve curtain region onto a 2D plane.

$T_c = 10°$ C. The flow is directed through a cylinder which is placed horizontally inside the measurement section and is therefore denoted *cooled cylinder flow*.

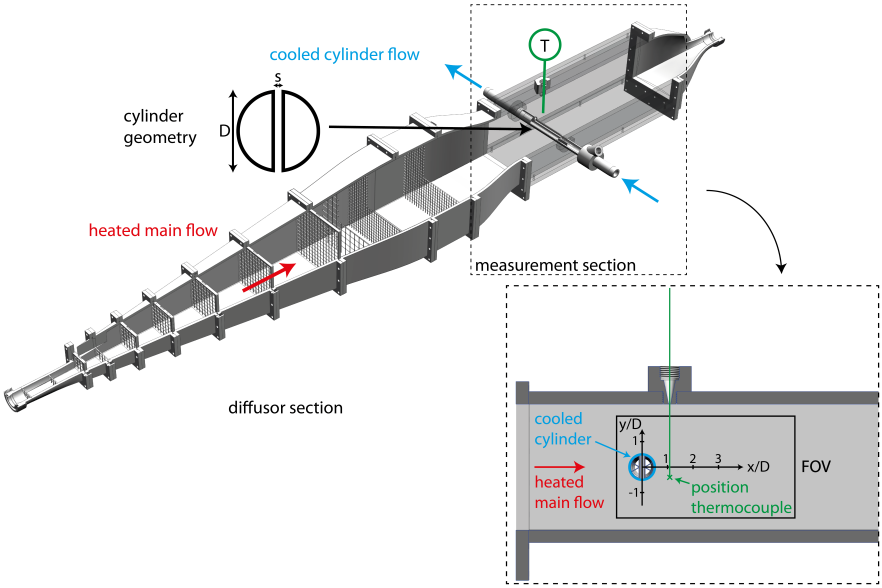

Figure 6.13: Experimental setup for the 4D measurements of a von Kármán Vortex Street (KVS). The heated main ($T_m = 55°$ C) flow (flow direction from left to right) is flowing through the diffusor section and into the measurement section. Vortices are shedding from the cylinder, which is cooled by $T_c = 10°$ C cold water. The cylinder is slotted (slot width $s/D = 0.15$) enabling a more homogeneous shedding frequency.

The cross section of the flow supply hoses (25.4 mm in diameter) is expanded within the 1050 mm total length diffuser section to a rectangular cross section of 100 mm × 100 mm and a uniform flow profile with negligible secondary flow effects enters the measurements section. The measurement section itself consists of a rectangular channel (100 mm × 100 mm, 450 mm length in flow direction) made from acrylic glass. Acrylic glass offers optical access and allows the detection of any air residing in the measurement section after deaeration. Air bubbles result in measurement artifacts and therefore have to

be completely removed.

A cylinder (diameter $D = 20\,\text{mm}$) made from polyamide is placed horizontally inside the measurement section as indicated in Fig. 6.13. By adding a slot to the cylinder (slot width $s/D = 0.15$), the shedding process can be improved in terms of a more uniform vortex detachment frequency [47, 68]. Moreover, an improved two-dimensional character of the shedding process can be achieved.

The cylinder is hollow and the cooled cylinder current flows through. Hence, a temperature difference of roughly 45K between the heated main flow and the flow inside the cylinder is created resulting in a temperature difference between vortices created in the wake and the main flow in the test section.

The "cooler" vortices in the wake of the cylinder can be detected by a thermocouple (TC) of type "K" which is placed downstream ($x/D = 1.1$) and off-center ($y/D = -0.4$) of the cylinder (position, see Fig. 6.13 bottom right). The z-position of the TC is $z/D = 1$, this way keeping the TC out of the measured FOV while at the same time maintaining a central position inside the flow channel in order to minimize potential wall-effects. Important parameters of the Kármán 4D MRV measurements are listed in Tab. 6.5. The Re number, calculated using the main flow bulk velocity, $\text{u}_{\text{bulk}} = 0.0325\,\text{m/s}$, the kinematic viscosity of water at 55° C ($\nu_{\text{water},55°C} = 0,5109 \times 10^{-6}\text{m}^2/\text{s}$) and with respect to the cylinder diameter D is $Re_D = 1272$. The Strouhal number is calculated to $St = 0.242$ [85], vortex shedding is thus expected at a frequency of $f_{\text{est}} = 0.39\,\text{Hz}$.

6.3.2 Trigger generation

The measured temperature signal of the TC is used to identify the periodic behavior of the flow and is, moreover, intended to be used for the creation of a trigger signal. The TC is placed within the pathline of the cold vortices shedding from the cylinder bottom and is thus capable of identifying the vortices from the varying temperature signal.

Figure 6.14 shows an example of the temperature signal, acquired with the settings described in Tab. 6.5. The blue line shows the temperature signal measured by the TC over a duration of 10 sec. The line clearly indicates the periodic behavior of the "cold" vortices passing by. The uniform, constant vortex detachment frequency is demonstrated from the temperature signal

Table 6.5: Parameters and settings of the 4D MRV measurements of the von Kármán vortex street.

Flow parameters		Imaging parameters	
Main flow rate (V_m)	19.5 L/min	VENC	0.1m/s
Main flow temp. (T_m)	55°C	Echo Time (TE)	5.935 ms
Bulk vel. (u_{bulk})	0.0325 m/s	Rep. time (TR)	52.2 ms
cyl. flow rate (V_c)	15 L/min	Flip angle	7°
cyl. flow temp (T_c)	10°	Matrix size	$128 \times 128 \times 1$
cyl. diameter (D)	20 mm	Voxel size	$1.25 \times 1.25 \times 5\text{mm}^3$
cyl. slot width (s/D)	0.15	no. of phase angles	43
Re number (Re_D)	1272	Temp. resolution (t_{res})	52.2 ms
Strouhal number (St)	0.242	Cycle duration (t_D)	2440 ms
Shedding frequency (f)	0.41 Hz	Data acquisition (t_A)	2min 30sec
		no. of acquisitions (N)	2

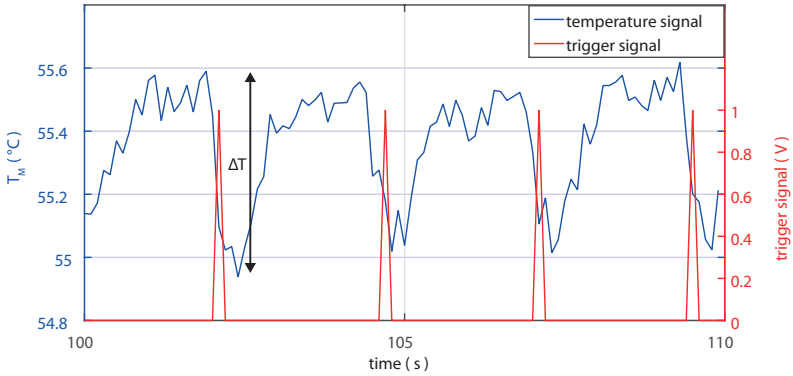

Figure 6.14: The temperature-signal of the main flow as measured by the thermocouple over a period of 20 s clearly indicates the periodic behavior of the cold vortices passing by (blue line). The falling edge of the temperature signal is used to produce the trigger-signal (red line).

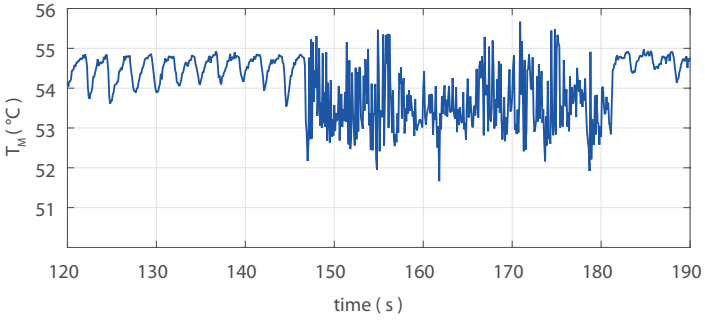

Figure 6.15: The temperature signal acquired by the TC is highly degraded during the measurement procedure.

which was acquired over $t \approx 100\,\text{min}$. A standard deviation of 4.77% of the average cycle length was calculated. This low standard deviation is beneficial for the phase averaging, resulting in low smearing of the velocity data due to phase jitter. A trigger signal can be generated using a simple amplitude threshold on the falling edge of the temperature trace (red line, Fig. 6.14), which is then fed into the MR scanner as a trigger signal to be used for subsequent phase averaging of the MRV measurements. Note the relatively low temperature drop provoked by the bypass of the cold vortices that lies in the order of $\Delta T < 1^\circ\,\text{C}$. Long-term temperature changes in the heated main flow arise and cause temperature variations in the order of $\pm 1^\circ\,\text{C}$. The simple amplitude threshold is therefore extended by a moving average mean value to account for these temperature-changes.

Application in MR environment Fig. 6.15 graphically illustrates the difficulties that arise when applying the trigger mechanism in MR environment during data acquisition. The temperature signal is highly degraded as soon as the MRV measurement procedure starts. The cause of this signal failure lies in the fast development of temporary magnetic field gradients and the RF excitation pulses, that are an inherent component of the MR data acquisition procedure. The TC thereby acts as an antenna, and the magnetic field gradients induce faulty voltages, which are superimposed onto the TC temperature signal, provoked by electromagnetic induction. A TC location

outside of the scanner bore would decrease the effect of the changing magnetic fields and thus improve the temperature measurements. Due to the fast decay of the shedding vortices (and simultaneously the decay in ΔT), the temperature signal must however be acquired in direct proximity of the cylinder. It is presumed, that a shielded TC would not be affected to this extent by the magnetic field gradients; however, this could not be tested in the scope of the present study. Instead, the TC was replaced by a gallium arsenide based fiber-optic temperature sensor (*Optocon, TS2 sensor* and *Optocon Fotemp-19" signal conditioner*). The sensor does not contain any ferrite metal parts and is completely non-conductive. Yet, the generated temperature difference ΔT can not be adequately resolved due to insufficient temperature-resolution of the sensor.

As a workaround to this issue, the temperature signal, provided by the TC, was used to determine the average cycle duration (t_D) of the periodic vortex shedding. The cycle duration was calculated to be $t_D = 2440\,\text{ms}$, corresponding to a shedding frequency $f = 0.41\,\text{Hz}$. The slight increase with respect to the estimated shedding frequency ($f_{\text{est}} = 0.39\,\text{Hz}$) is expected to originate from the slotted cylinder geometry, which is known to provoke slightly higher shedding frequencies Zdravkovich [87]. An external trigger, included in any medical MR scanner, is set to t_D and the phase-averaged measurements are started. The approach of determining the trigger frequency until measurements are started and setting the determined frequency to the external trigger generator was denoted *hybdrid trigger* generation. Even though the standard deviation of the cycle length (<5%) is low, and the slotted cylinder in combination with the flow settings enables a very constant shedding frequency, potential outliers in cycle length can not be excluded. Herein lies the drawback of the external trigger mechanism compared to the proposed approach of generating the trigger directly off the measured temperature signal, where outliers in cycle length will be identified and omitted. Outliers in cycle length will cause phase-blending and velocity smearing. In order to minimize the probability of occurring outliers, the time of data acquisition (t_A) was kept as short as possible. The phase-resolved 2D2C velocity field of this setup was acquired in $t_A = 2$ min 30sec.

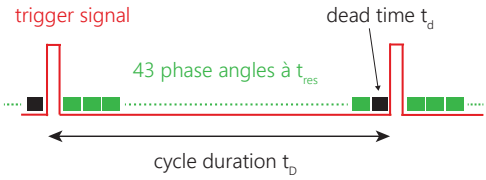

Figure 6.16: Schematic of the 4D MRV sequence that enable phase-resolved measurements. The periodic flow (cycle duration t_D) is divided into 43 phases per trigger cycle. The flow is not acquired during the dead time t_d, which remains at the end of each cycle.

6.3.3 Data processing und experimental results

A coordinate system, made dimensionsless by the cylinder diameter D is defined, with the origin being the central axis of the cylinder and the x-axis pointing in flow direction (see Fig. 6.13, bottom right). The z-origin of the coordinate system lies in the central xy-plane of the 100 mm wide measurement section.

A 2D-slice was acquired in the central xy-plane using the 4D sequence. The covered FOV measures $(160 \times 160)\text{mm}^2$ with an imaging matrix of 128×128 pixels, resulting in an in-plane resolution of (1.25×1.25) mm^2. The slice-thickness was 5 mm. A phase-resolution of 43 phases per trigger cycle was realized. Two k-space lines per phase were filled at once, resulting in a total time of data acquisition $t_A = 2\text{min } 30\,\text{sec}$ per measurement.

Figure 6.16 schematically illustrates the 4D MRV measurement principle for the phase-resolved acquisition of a periodic flow. Between the trigger signals which indicate the onset of a new cycle (cycle duration t_D), the phases are partially acquired. This procedure is repeated until the data set is entirely acquired. Due to measurement restrictions, the periodic flow cannot be thoroughly resolved. A remaining dead time (t_d) is always present. The periodic flow ($t_D = 2440\,\text{ms}$) is resolved into 43 phases per trigger cycle, which were acquired with a temporal resolution of $t_{\text{res}} = 52.2\,\text{ms}$, yielding a dead time

$$t_d = t_D - (\#PA \times t_{\text{res}}) = 195.4\text{ ms}, \tag{6.10}$$

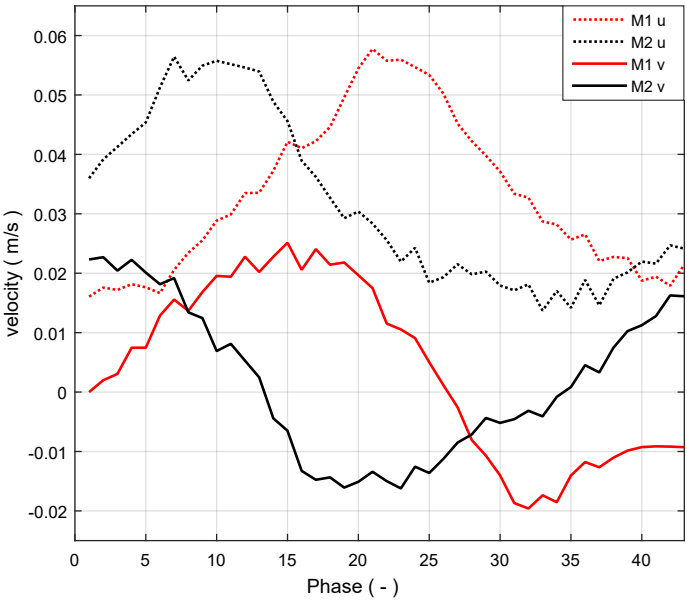

Figure 6.17: Streamwise u velocity component (dotted line) and cross-streamwise v velocity component (continuous line) of the flow, extracted for measurements M1 and M2 at the location ($x/D = 1.1$, $y/D = 0.4$, $z/D = 0$). A distinct phase-offset between both measurements is visible.

equivalent to 3.74 phases. Moreover, both measurements can be combined such that the dead time t_d is removed.

Fig. 6.17 depicts the u and v velocities extracted from both independent MRV-measurements at the location ($x/D = 1.1$, $y/D = -0.4$, $z/D = 0$). Dotted and continuous lines depict the u velocity and the v velocity component, respectively. The red and black lines indicate measurement M1 and M2, respectively. An apparent offset in phase between M1 and M2 is visible in both velocities. A cross-correlation was employed to detect the phase-shift and enable averaging of M1 and M2. The result is visualized in Fig. 6.18, where the average of M1 and M2 is represented in blue. Again, dotted and continuous lines represent the u and v velocities. Note, that in the two shaded areas, measurement data was only available from measurement M1 (first shaded area,

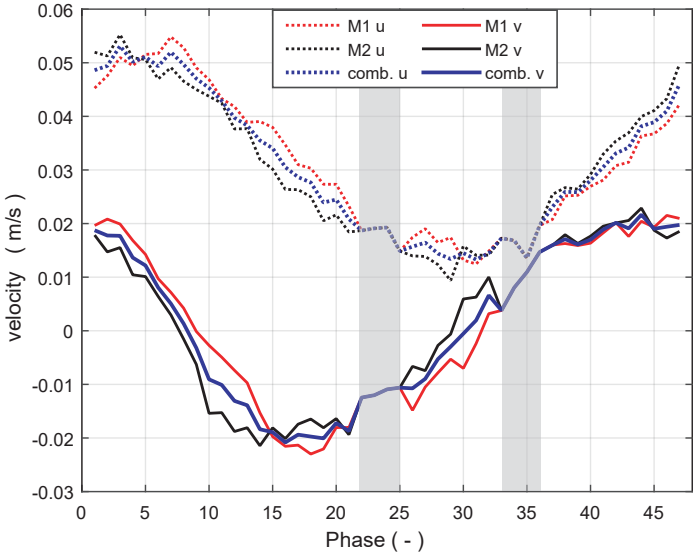

Figure 6.18: Streamwise u velocity component (dotted line) and cross-streamwise v velocity component (continuous line) of the flow, extracted for measurements M1 and M2 at the location ($x/D = 1.14$, $y/D = 0.4$, $z/D = 0$). Velocity profiles after data processing.

Phases 22-25) or from measurement M2 (second shaded area, Phases 33-36), respectively, due to the dead time t_d of each individual measurement. The combined data set then consists of a total of 47 phases, without any dead time present, adding up to an artificial cycle duration $t_D^\star = \#PA \times t_{\text{res}} = 2453.4\,\text{ms}$. The difference in cycle duration $t_D^\star - t_D = 13.4\text{ms} \approx 0.25 t_{\text{res}}$ is assumed to be reasonably small. Moreover, the maximum error due to phase-offset between the individual measurements will not exceed $t_{\text{res}}/2$.

The z vorticity of the flow regime at 6 selected phases is visualized in Fig. 6.19 a-f. The phases are approximately evenly distributed over the cycle duration t_D, the corresponding times in the vortex shedding cycle are plotted in the bottom right corner. The flow direction is from left to right, as indicated in Fig. 6.19a. The uv-vector layer, every 10th vector displayed, is superimposed onto the z-vorticity contour and is displayed with a uniform vector length in order to better represent the flow direction. The creation

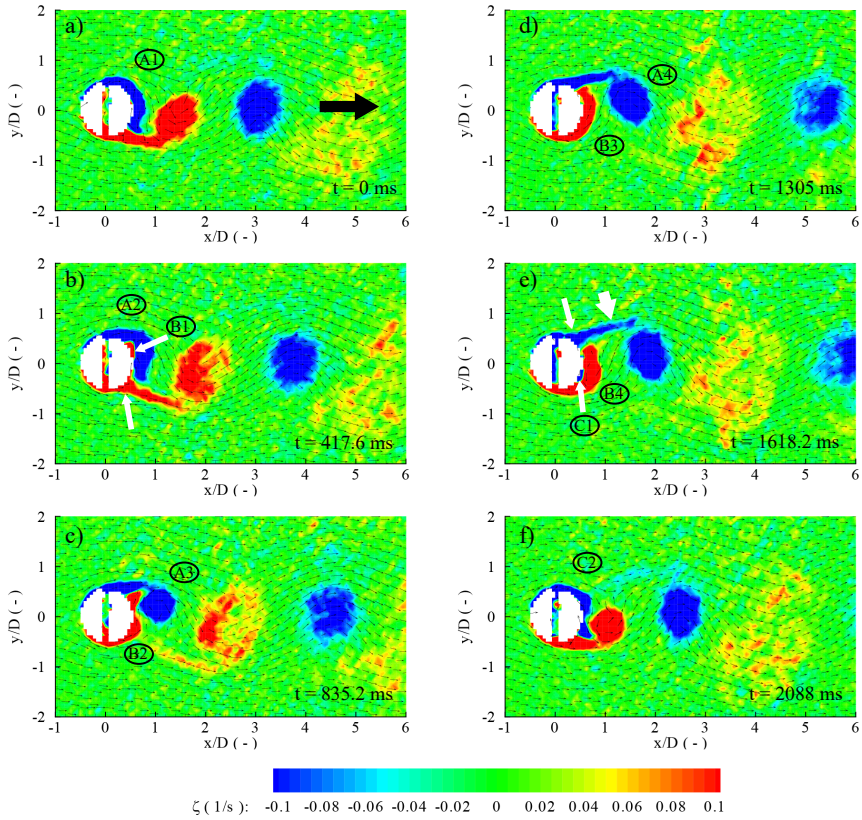

Figure 6.19: The vortex shedding procedure of the KVS, displayed at 6 distinct points in time. Displayed is the z vorticity ζ of the flow. Flow direction is from left to right. The superposed vector-layer, every 10th vector visualized, has a uniform length to better visualize the flow direction. The blue region of negative vorticity (A1) grows in size up to a point, when a region of opposite vorticity emerges (B1), causing the total detachment (A3) and the shedding (A4) of the vortex from the upper edge of the cylinder.

of the KVS can be clarified: The onset of a vortex with negative vorticity (vortex A) at the beginning of the cycle is displayed in Fig. 6.19a, where a layer of fluid with negative vorticity is spread over nearly half the slotted cylinder circumference (A1). The thickness of the layer increases with time, until the emerge of a new vortex (vortex B) of positive vorticity (upper white arrow, B1). The emergence of this new vorticity region results in a partial detachment of vortex A from the cylinder surface (A2). The further growth of the vorticity region eventually leads to complete detachment from the cylinder surface. The vortex is shed from the cylinder top and flows off (A3-A4). The negative vorticity of the fluid still connected to vortex A (wide arrow in Fig. 6.19e) rapidly dissipates. As a result of the detached vortex A, both regions of positive vorticity (white arrows Fig. 6.19b) unite (B2) and develop a continuous layer which grows in size (B3-B4). The onset of yet another vortex C is visualized in Fig. 6.19e (C1). The same mechanism as before leads to the detachment of vortex B and the growth of the vortex region C (C2, Fig. 6.19f) and the cycle is repeated.

6.4 Summary

4D measurements are presented for two test case configurations: The flow inside an engine flow model featuring actuated movable intake valves, and the flow of Kármán vortices shedding from a confined cylinder.

4D engine flow model Convincing results of the volumetric flow inside the engine flow model were presented for the mean flow measurements in section Chapter 5. These were performed for a steady valve lift of $\eta = 9.2\,\mathrm{mm}$, corresponding to a CA position of $\lambda = 270°$. The motivation for the 4D measurements inside this geometry is, to imitate a large portion of the intake stroke of the ETB and, by doing so, being able to analyze the evolution of the volumetric in-cylinder flow. Therefore the flow model was modified and equipped with hydraulically actuated moving intake valves and a bypass-system, likewise operated by hydraulic actuators. The valve motion and the modulation of the water flow were modeled such that they correspond to the real engine intake flow, operated at 800 rpm.

A FOV with the dimensions $(160 \times 256 \times 310)\mathrm{mm}^3$ and a spatial resolution

of 1.6 mm (isotropic) is acquired. The 4D measurements feature a phase resolution of 30 phases per cycle, corresponding to a "temporal resolution" of $t_{\mathrm{res}} = 52.0\,\mathrm{ms}$ (cycle duration $t_D = 1566\,\mathrm{ms}$). A resulting total number of $\approx 282 \times 10^6$ velocity vectors is acquired in roughly 55 min. The flow data is thoroughly validated by means of PIV data. The parameters $\gamma'_{\mathrm{MRV,PIV}}$ and $\hat{\sigma}$ are introduced enabling the determination of a temporally changing valid flow region within the MRV data set.

The flow evolution within the *mid-valve plane* is presented for six distinct phase angles during the valve opening process. The development of a noticeable high-speed intake-jet is depicted, as is the development of a recirculation zone, present throughout a large portion of the intake stroke within the identified underflow region. This recirculation zone is moreover identified within the figure depicting the flow evolution through the valve curtain region. The visualization of this flow region is not feasible by means of any other current measurement technique.
To the author's best knowledge, these presented measurements represent the first 4D MRV measurements for technical flows, where the flow is forced to be periodic by moving geometrical boundaries during data acquisition.

KVS 4D measurements of Kármán vortices, shedding of a confined, slotted cylinder were acquired to address the field of "internal trigger generation". Internal trigger generation is, in medical context, applied for the ECG-triggered investigation of blood flows. Although the online internal trigger generation from a temperature signal did not succeed for the present case due to the harsh MR environment, this approach ought to be pursued as it promises new possibilities in quantification of periodic flows without the need for external triggering. Internal trigger signals, extracted from the flow under consideration, can react to potential deviations in cycle length and thus prevent phase jitter.

Data acquisition of the KVS was thus enabled by using the built-in trigger generator of the MR scanner, which provided the cycle duration determined beforehand. Due to the constant shedding frequency, ensured by the cylinder-geometry (diameter $D = 20\,\mathrm{mm}$, slot width $s/D = 0.15$), as well as the flow settings ($Re_D = 1272$, $St = 0.242$) phase-shifts during the measurements, caused by non-uniform vortex shedding, could be prevented. The chance of phase jitter arising due to outliers in cycle length was reduced by minimizing

the time of data acquisition. A 2D2C flow field with a phase resolution of 43 phases (cycle duration $t_D = 2440\,\text{ms}$) was acquired in $t_A = 2\text{min}\ 30\text{sec}$ per measurement.

A combination of two subsequently acquired measurements allowed the elimination of the dead time t_d, characteristic for the utilized 4D MRV sequence. This enabled the analysis of the entire periodic cycle resolved in 47 phases. The vortex shedding process is descriptively analyzed, assuming two-dimensional flow around the cylinder and neglecting potential three-dimensional flow effects in the vortex generation process. It is emphasized that the acquisition of a fully volumetric 4D data set is possible with the described measurement procedure. Similar measurements with conventional optical measurement technique are possible [62], yet very complex.

Both presented test cases depict the great potential of the phase averaged MRV measurement technique for the analysis of unsteady, periodic flows. The large amount of flow data acquired per time is unrivaled by other measurement techniques. The validation by means of conventional measurement techniques showed excellent conformity.

7 Turbulence measurements

Turbulent flows are omnipresent in technical applications. A characteristic of turbulent flows are chaotic, unsteady vortices of many time scales that cause fluctuations of the local flow velocity. These velocity fluctuations can be quantified by means of various suitable measurement techniques (see Chapter 2). Moreover, the velocity fluctuations are used for the calculation of Reynolds stresses, which are an important feature for flow characterization.

In the context of this section, turbulence measurements are presented within a backward-facing step (BFS) geometry and within the engine flow model. The BFS geometry is a simple geometry with well-defined production of turbulence downstream of the step and enables convenient optical access for LDV validation measurements. Turbulence measurements within the engine flow model depict the capability of this technique to be applied in more complex flow geometries. The measurement results are compared to PIV measurements acquired in the ETB.

7.1 Measurement procedure

The general procedure for the measurement of turbulence quantities deviates from the MRV measurements. It is therefore outlined within this section. To recall: For the MRV flow measurements, the *VENC* value, introduced on page 30, is set corresponding to the maximum expected flow velocities within the flow under consideration. The amplitude of the "velocity encoding" bipolar gradient is directly influenced by the VENC value, according to Eq. 3.14 (page 30). The flow velocity is encoded in the phase of the received signal, see Sec. 3.3.

The working principle of the turbulence measurements is based on the concept of *turbulent diffusion*, see Sec. 3.4. Turbulent diffusion directly influences the magnitude of the received MR signal. The amplitude and direction of the bipolar gradients, now denoted "turbulence encoding" gradients, is set man-

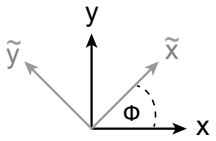

Figure 7.1: Transformation of the coordinate system under the angle ϕ.

ually and is independent of any present flow velocities within the flow under consideration. The turbulence encoding gradient strength is rather adapted accordingly to the present turbulence level.

It can be noted, that the utilized measurement sequence for the MR turbulence measurements is very similar to the one used for regular flow measurements. The main difference between both measurement techniques is the utilized information of the MR signal: Flow is encoded in the signal phase, while turbulence is encoded in the signal magnitude. More precisely: Flow is encoded in the phase difference between two measurements with different first gradient moments in encoding direction; turbulence is encoded in the magnitude difference between measurements with different first gradient moments in the encoding direction. Thus, a "turbulence data set" consists of a specific number of measurements with different gradient amplitudes.

Acquisition of velocity standard deviations For the determination of the standard deviation (SD) of the flow velocity in x direction, σ_u, measurements with different amplitudes of the turbulence encoding gradients are applied in x direction. σ_u can be determined from the loss of signal magnitude, according to Eq. 3.23. The analogue procedure is performed for the acquisition of the velocity standard deviation in y direction, σ_v.

Acquisition of shear stresses For the determination of shear stresses, the velocity SD must be acquired in three directions. After the application of the turbulence encoding gradients in x and y direction, the gradient is applied along $\tilde{x}$-direction which is the bisecting angle between the x- and y-direction. The $\tilde{x}$ gradient is generated through simultaneous application of the x- and y-gradients with equal gradient strengths. A resulting gradient at

an angle of $\phi = 45°$ is produced, see Fig. 7.1, the SD $\sigma_{\tilde{u}}$ is determined. After the determination of the SD σ_u,σ_v and $\sigma_{\tilde{u}}$, these parameters can be used to calculate τ_{uv}. Eq. 7.1 describes the equation of the Mohr circle [39], for a transformation of a second order tensor. For the Reynolds stress tensor, the equation reads

$$\sigma_{\tilde{u}}^2 = \frac{1}{2}\left(\sigma_u^2 + \sigma_v^2\right) + \frac{1}{2}\left(\sigma_u^2 - \sigma_v^2\right)\cos\left(2\phi\right) + \tau_{uv}\sin\left(2\phi\right). \tag{7.1}$$

From Eq. 7.1, the shear stress τ_{uv} can be calculated if σ_u, σ_v and $\sigma_{\tilde{u}}(\phi)$ are known. In the special case of $\phi = 45°$, this expression can be further simplified to

$$\sigma_{\tilde{u}}^2 = \frac{1}{2}\left(\sigma_u^2 + \sigma_v^2\right) + \tau_{uv}. \tag{7.2}$$

Rearranging yields the expression for the shear stress τ_{uv}

$$\tau_{uv} = \sigma_{\tilde{u}}^2 - \frac{1}{2}\left(\sigma_u^2 + \sigma_v^2\right). \tag{7.3}$$

The applied gradients for the turbulence measurements within the BFS geometry and the engine flow model (see following sections) are listed in Tab. 7.1. Eight different gradient strengths were applied in the x and y direction, six different gradient strengths were applied in the "$\tilde{x}$ direction" which is the bisecting angle between the x and y direction. The number of six gradient strengths in the $\tilde{x}$ direction is explained by the maximum possible gradient strength of $G_{\max} \approx 45\text{mT/m}$ that can be generated within the MR scanner.[1] The gradients in $\tilde{x}$ direction were generated by simultaneous application of the gradients in x- and y direction. Therefore the amplitude of the gradient in $\tilde{x}$ direction corresponds to $\tilde{G} = \sqrt{2}G$ of the individual gradients. The procedure for the generation of the $\tilde{x}$-gradient was adapted for the measurements inside the engine flow model, yielding equal gradient-strengths in all three spatial directions. Additionally, one acquisition is conducted with zero gradient amplitude applied. This measurement yields the reference signal magnitude, denoted S_0.

[1] This limitation does not represent physical limitations by the gradient unit, but rather an artificially applied limitation to prevent unintended excessive gradient strengths during patient examinations.

Table 7.1: Applied gradient strengths for the turbulence measurements inside the BFS and engine flow model.

Applied gradient strengths G (mT/m)								
Backward facing step								
x	5	10	15	20	25	30	35	40
y	5	10	15	20	25	30	35	40
$\tilde{x}$	7.07	14.1	21.2	28.3	35.4	42.2		
Engine flow model								
x	5	8	13	19	21	28	33	40
y	5	8	13	19	21	28	33	40
$\tilde{x}$	5	8	13	19	21	28	33	40

The effect of applied gradients on a turbulent flow is visualized and discussed in Fig. 3.9 (page 32). The decay in signal magnitude far downstream of the step (see ④ in S_0, Fig. 3.9) is a result of the spatially limited coverage of the receiver coil. The coil is placed on top of the setup and oriented such that the highest signal is achieved near the step. The measurements are, therefore, presented in the range of $-1 \leq x/h \leq 3$, where homogeneous and sufficiently strong signal is provided.

7.2 Backward facing step measurements

7.2.1 Experimental setup

The experimental setup, illustrated in Fig. 7.2 consists of a diffuser for flow preparation and the backward-facing step (BFS) measurement section. The cross section $W \times H = 50\,\text{mm} \times 50\,\text{mm}$ with a length $l = 600\,\text{mm}$. The step consist of a 90° sector of a circle, step height $h = 30\,\text{mm}$. The relatively low aspect ratio $AR = W/h = 5/3$ does not provide a purely two-dimensional flow-situation inside the measurement section. Instead, three-dimensional secondary flows, generated by corner vortices, are generated. Yet, an almost two-dimensional flow situation within the central plane ($z = 0\,\text{mm}$), where the measurements were conducted, is assumed.

Table 7.2: Parameters and settings of BFS Turbulence measurements.

BFS geometry		Flow imaging parameters	
Cross section ($W \times H$)	50×50 mm^2	Matrix size	224×140
Length (l)	600 mm	FOV	220×137 mm^2
Step height (h)	30 mm	Voxel size	0.98×0.98 mm^2
Aspect ratio (AR)	5/3	Slice thickness	6 mm
Flow parameters		N_{rep}	50
Vol. flow rate (V)	65.3 L/min	TE / TR	5.98 / 8.7 ms
Temperature (T)	21.5° C	Acq. time/rep. (t_r)	2.4 s
Reynolds number (Re_h)	47,000	Total acq. time (t_T)	50 min

The fluid enters the channel from the top right as indicated by the blue arrow (Fig. 7.2) at a volume-rate of 65.3 L/min (flow temperature 21.5°C), resulting in a Reynolds number based on the step height of $Re_h \approx 47,000$. The step is designed hollow and fills up with water during the measurements, which minimizes measurement errors due to susceptibility effects [74].

The BFS geometry is particularly well suited for the turbulence measurements because of its simple geometry, well defined production of turbulence and easy optical access. MR turbulence measurements have previously been reported inside this geometry, see Elkins et al. [27]. LDV measurements, that serve as validation for the MR turbulence measurements, were acquired using an optical access via a perspex insert in the measurement region.

The turbulence measurements for the determination of σ_u, σ_v and $\sigma_{\bar{u}}$ were acquired consecutively, followed by a set of MRV velocity measurements in order to obtain mean flow velocities (Fig. 7.3). No flow components were acquired for the z direction. Instead, measurement time was spent in order to enable a number of $N_{\text{rep}} = 50$ acquisitions and thereby increase the SNR of the measurements by a factor of $\sqrt{N_{\text{rep}}}$, Haacke et al. [40]. Important imaging parameters for the BFS turbulence measurements are listed in Tab. 7.2.

The established coordinate system for the measurements is depicted in Fig. 7.3. The origin lies at the height of the step, with the x-axis pointing in the streamwise direction and the y-axis towards the top of the channel. The coordinate system is made dimensionless using the step height h.

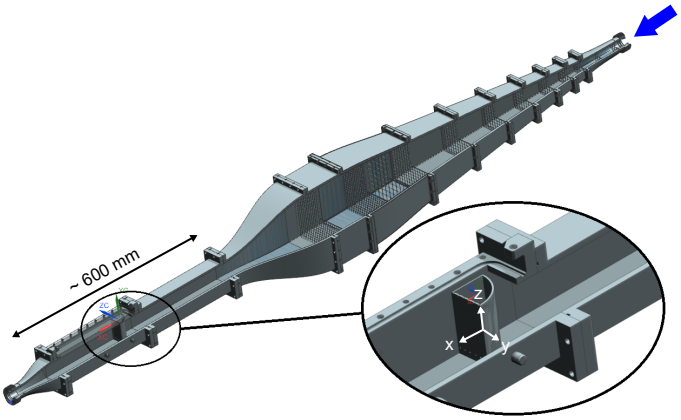

Figure 7.2: Backward facing step experimental setup for the MR turbulence measurements.

For the validation of the MRV results, LDV measurements are acquired and a quantitative comparison between both data sets is conducted at different x/h-locations within the channel. Black dashed lines indicate the locations for the comparison of MRV and LDV velocity profiles.

7.2.2 Results

The time for data acquisition per measurement repetition was $t_r = 2.4\,\mathrm{s}$. This is the acquisition time for a slice with 224×140 matrix size and a single gradient strength applied. A number of $N_{rep} = 50$ repetitions were acquired, adding up to an acquisition time of 120 s per applied gradient strength. This yields an acquisition time of 18 min per gradient direction, and thus a total time of data acquisition of $t_T \approx 52\,\mathrm{min}$ for the acquisition of the entire "2D turbulence set".

Fig. 7.3 shows a contour plot of the flow velocity in main flow direction u within the central plane ($z = 0\,\mathrm{mm}$) of the BFS channel. The flow direction is from left to right as indicated by the blue arrow. Maximum flow velocities $u \approx 1.3$ m/s are reached in the high-speed jet, situated in the upper part of the channel ($y/h > 0$). A recirculation zone is visible downstream of the step

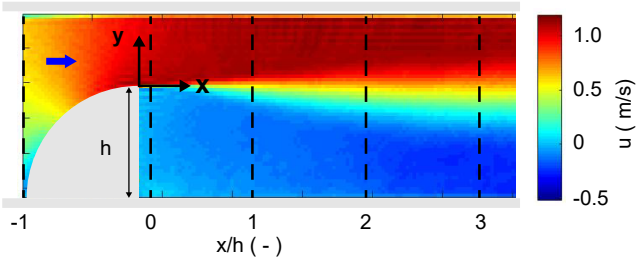

Figure 7.3: Contour plot of the main velocity component $\vec{u}$ measured by means of MRV flow measurements. Red color indicates large streamwise velocity, while blue color indicates zero, or slightly negative flow velocities. Moreover, the location of the coordinate system is depicted. The origin of the x-axis lies at the height of the step, pointing in streamwise direction. The y-origin lies at the top of the step, directing towards the topside of the channel, the z-origin lies in the center plane of the $W = 50\,\text{mm}$ wide channel. The axes are made dimensionless using the step height h. Flow profiles were extracted along different x/h-locations, as indicated by the dotted lines.

for $y/h < 0$. This region is characterized by negative u-velocities in the order of $u \approx -0.2\,\text{m/s}$. High-speed and recirculation zones are separated by a shear layer ($y/h \approx 0$). This shear layer is characterized by steep velocity gradients and high turbulence intensity.

Contour plots of turbulence quantities are visualized in Fig. 7.4. Illustrated is (a) the standard deviation (SD) of the streamwise flow velocity u, σ_u (b) SD of the cross flow velocity v, σ_v and (c) the calculated shear stress τ_{uv} values.

The contour plot values for σ_u and σ_v were determined according to Eq. 3.23 on page 35. The contours show a very similar trend, with a distinct cone-shaped region of high flow SD, visible in the shear layer downstream and at height of the step ($0.1 \leq x/h \leq 3, y/h \approx 0$). Maximum values for σ_v lie in the order of $\sigma_v \approx 0.2\text{m/s}$, while σ_u lies considerably higher with levels of up to $\sigma_u = 0.3\,\text{m/s}$ and $\frac{\sigma_u}{u} \approx 60\%$ (local main flow velocity $u \approx 0.5\,\text{m/s}$). Fig. 7.4 (c) illustrates the values for the shear stress τ_{uv}, that was calculated from the measurements of σ_u, σ_v and $\sigma_{\tilde{x}}$ according to Eq. 7.3. Only a very small region of considerable shear stress is visible ($x/h \approx 0.5$, $y/h = 0$), with maximum

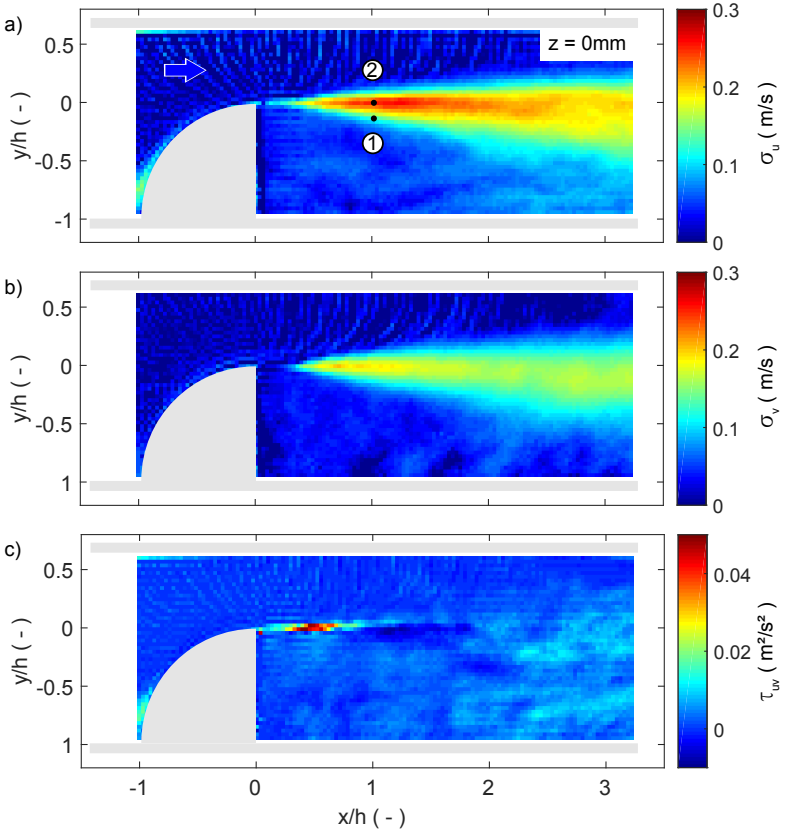

Figure 7.4: Contour plots of turbulence quantities within the BFS flow geometry ($z = 0\,\text{mm}$), acquired using MR turbulence measurements. Depicted is a) the standard deviation of the flow in streamwise direction, σ_u b) SD in cross-streamwise direction, σ_v and c) calculated values for the shear stress τ_{uv}.

values of $\tau_{uv} \approx 0.05\,\mathrm{m}^2/\mathrm{s}^2$.

Quantitative validation MR turbulence measurements were validated with LDV measurements, acquired in the same measurement region and under equal flow conditions in 0.5 mm steps. Fig. 7.5 shows flow profiles, extracted at the previously defined locations within the central plane ($z = 0\,\mathrm{mm}$) of the BFS. The blue lines indicate the MRV data set while the red lines are acquired via LDV.

Fig. 7.5 (a) shows the main flow velocity u. The agreement between LDV and MRV is excellent, both measurement sets nearly coincide onto one line at all five x/h-locations.

The SD of the flow in main flow direction, σ_u, and cross-flow direction, σ_v, are visualized in Fig. 7.5 b) and c), respectively. The agreement between LDV and MRV is good, especially for the first three streamwise locations ($x/h = -1;\ 0.1;\ 1$) in σ_u. Outliers, depicted by MRV are visible at $x/h = -1$, $y/h \approx -0.7$ in σ_u. The maximum MR-determined values are in accordance with the values determined by LDV and lie in the order of $\sigma_u \approx 0.25\,\mathrm{m/s}$. For the locations $x/h = 2$ and $x/h = 3$ however, the MR-determined values are underestimated, compared to the LDV determined values.

The comparison between MRV and LDV for σ_v again shows a relatively good agreement. Yet, in contrast to σ_u, the values for σ_v are somewhat overestimated by the MRV turbulence measurements, when compared to the LDV measurements. This is especially the case for the locations $x/h = 1;\ 2;\ 3$.

Lineplots of the calculated shear stress τ_{uv} are visualized in Fig. 7.5d. The measurement results agree regarding the magnitude of the determined shear stress, yet the overall agreement between MRV and LDV is poor. The smooth trend of τ_{uv} values in the turbulent zones for the LDV measurements (especially for the locations $x/h = 2$ and 3) can not be reproduced by the MR measurements. Instead, distinct peak values of τ_{uv} are identified by the MR measurements (Fig. 7.5d, $x/h = 0.1$ and $x/h = 1$).

7.3 Engine flow model measurements

One main advantage of the MR-techniques is the possible data acquisition in arbitrarily complex geometries. This also holds true for the turbulence mea-

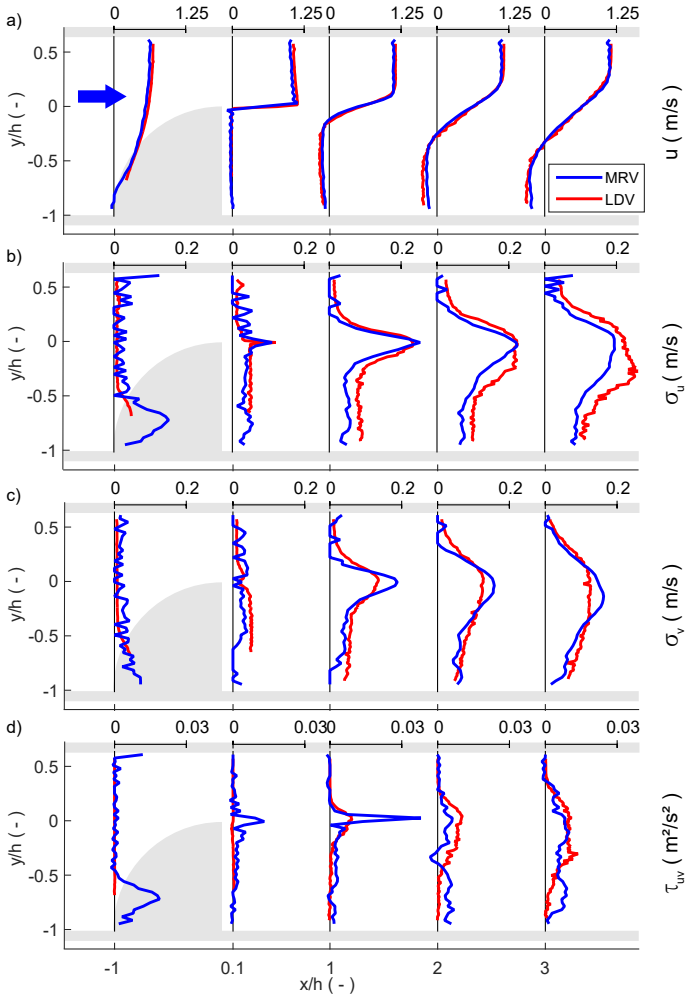

Figure 7.5: Lineplots comparing the LDV and MRV measurements conducted inside the BFS within the central plane ($z = 0\,\text{mm}$). a) The main flow velocity u b) SD of the flow in streamwise direction, σ_u c) SD in cross streamwise direction, σ_v and d) calculated values for the shear stress τ_{uv}.

Table 7.3: Parameters and settings of the engine turbulence measurements.

Engine geometry		Flow imaging parameters	
Cylinder head	SG	Matrix size	224×224
Valve lift	9.2 mm	FOV	$230 \times 230\,\mathrm{mm}^2$
$\equiv$ CA position	270° bTDC	Voxel size	$1.02 \times 1.02\ \mathrm{mm}^2$
Flow parameters		Slice thickness	4 mm
Vol. flow rate	50 L/min	N_{rep}	40
Temperature	21.0° C	TE / TR	6.3 / 9 ms
		Acq.time/rep. (t_r)	3.3 s

surements. For this reason, this section gives an impression of the possible turbulence quantification without optical access in such a complex flow geometry as the optical engine geometry, discussed in Sec. 4.1. To enable optical validation measurements within this geometry, the engine model was adapted such that the quartz-glass cylinder of the ETB could be inserted during the measurements. This way optical access into the cylinder chamber was granted and LDV measurements could be acquired. A detailed description of these measurements can be found in Feldmann [29]. PIV measurements acquired inside the ETB were also used for data validation. These measurements were provided by the *Department of Reactive Flows and Diagnostics* (RSM) at Technische Universität Darmstadt.

As in the case of the BFS measurements, 2D slices were acquired inside the engine model instead of the volumetric turbulence field. The acquisition of an entire 3D turbulence volume is possible with the existing MR-sequences. However, with respect to the limited measurement time, it was preferred to remain with 2D turbulence acquisitions. Turbulence measurements were performed in the cylinder symmetry plane ($z = 0\,\mathrm{mm}$) as well as in the mid-valve plane ($z = 19\,\mathrm{mm}$). The locations are depicted in Fig. 7.6. All important measurement parameters and information regarding the flow settings are listed in Tab. 7.3. The strengths of the "turbulence-encoding gradient" used for the measurements are listed in Tab. 7.1.

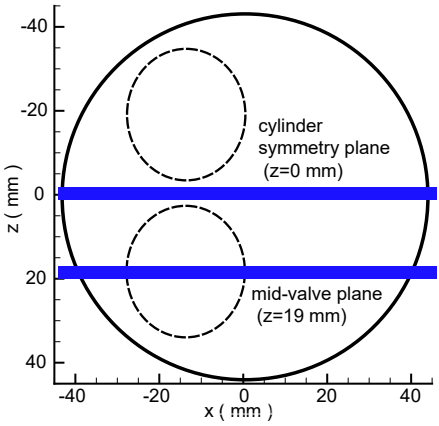

Figure 7.6: Schematic topview on the engine flow model. The intake valves are sketched via dashed lines. Both acquired planes are shaded blue.

Comparison of MRV, LDV and PIV data

Mid-valve plane Fig. 7.7 (left) visualizes the SD of the flow velocity within the mid-valve plane ($z = 19\,\text{mm}$) as a 2D contour plot. Depicted is the SD σ_u of the flow velocity in the x direction (top) and the SD σ_v of the flow velocity in y direction (bottom). The corresponding flow velocities are visualized in Fig. 5.7 on page 57.

A quantitative comparison between the MRV, LDV and PIV measurement data is given in Fig. 7.7 (right). Illustrated is in b) the mean velocity u (red lines) and σ_u (black lines) and in c) the mean velocity v (red lines) and σ_v (black lines). The profiles were extracted along $z = 19\,\text{mm}$, $-38 \leq x \leq 38$, 2 mm below the valve, corresponding to a y-position of $y = -8\,\text{mm}$ (black dotted line Fig. 7.7 left). The x-range of the LDV (dashed lines) and PIV (dotted lines) flow profiles are limited to $|x| < 30\,\text{mm}$ due to optical reflections towards the outer cylinder borders, Fig. 7.7(right).

A region of high σ lies near to the high-speed intake jet for both velocity components (① in Fig. 7.7). This is the region where the flow experiences a strong change in direction and strong velocity gradients are present in the shear layer of the intake jet. A secondary distinct region of high σ_u is present in the wake of the valve stem, ②, where a recirculation region was previously

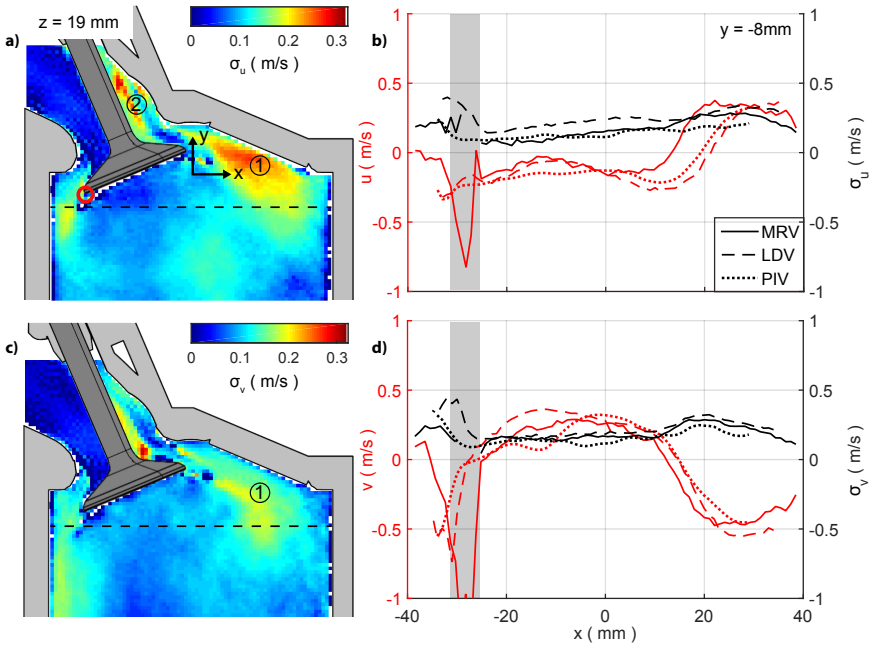

Figure 7.7: The SD of the flow velocity inside the transparent engine model, within the mid-valve plane ($z = 19\,\text{mm}$). Left: Contour plots of the velocity SD acquired by MRV Right: Quantitative comparison of b) velocity u and SD σ_u and c) velocity v and SD σ_v.

identified (Sec. 5.3, page 54).

The extracted profiles show generally good agreement and a similar trend for the mean flow velocities u and v and for the velocity standard deviations in both spatial directions, σ_u and σ_v, respectively.

Contaminations Contamination of the intake valves by ferromagnetic dust led to corrupt MRV flow data in direct vicinity of the intake valves. The contamination covers the entire circumference of the intake valve. The shaded region in the flow profiles highlights the corrupt MRV flow data by depicting outliers in the flow velocity. No SD was calculated for this region for the MRV

data set. The red circle in Fig. 7.7a marks the region of the contamination which led to the region of corrupt flow data.

Mid-cylinder plane The contour plots of the standard deviations σ_u and σ_v within the symmetry plane of the cylinder ($z = 0\,\text{mm}$) are depicted in Fig. 7.8. The flow profiles, extracted along $y \approx -8\,\text{mm}$, again show an overall good agreement of the flow velocity of all three measurement techniques. The agreement regarding σ_u and σ_v, however, is only moderate: The PIV and LDV data sets for σ_u and σ_v exhibit the same trend, yet with a constant offset. This offset may be caused by the normalization of the PIV data, which was necessary in order to compare the PIV measurements, conducted in air flow with the LDV and MRV measurements, conducted in water flow.[2] The MRV turbulence data set, however, shows a considerably different trend over a large range.

As depicted by the gray shaded area, considerable differences appear in the region for $x < 0\,\text{mm}$ for both, σ_u and σ_v. This is the region between both intake valves, which is most affected by the contamination. The signal magnitude in this region is manipulated by the presence of the ferromagnetic material, thus preventing a reasonable determination of the SD. In contrast to the MR turbulence measurements, the MRV flow measurements are hardly impaired by these contaminants.

One conclusion is, that the MR signal phase is less influenced by the presence of the ferromagnetic material than the signal magnitude. As consequence the flow measurements, encoded in the signals phase, are not as sensitive to these impurities.

7.4 Discussion

MR turbulence measurements were presented within a BFS geometry and within the engine flow model, presented in Chapter 5.

The BFS setup reflects a geometrically simple setup which enables convenient acquisition of validation data by means of optical measurement techniques. LDV measurements were acquired within this geometry, these mea-

[2] This normalization was also carried out for the mean flow measurements and is discussed at length in Chapter 5.

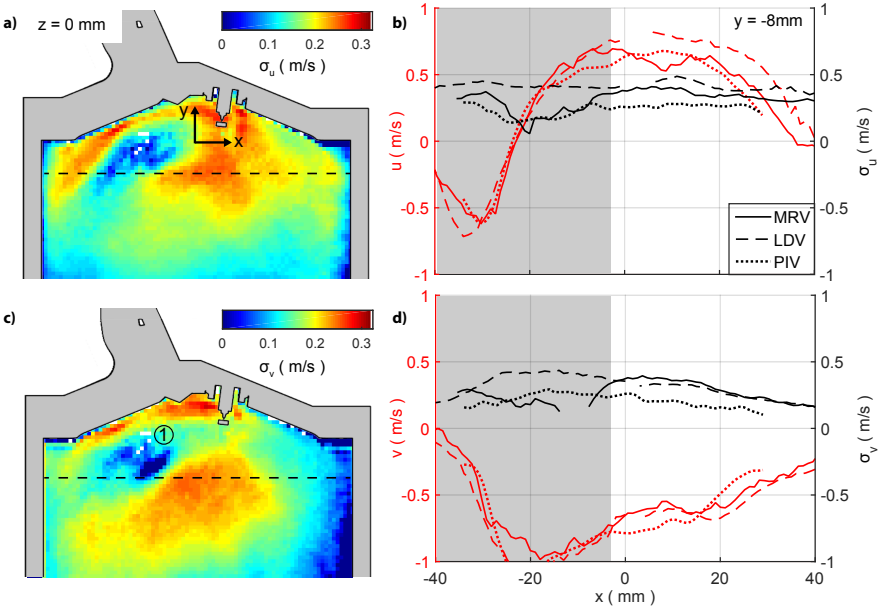

Figure 7.8: The SD of the flow velocity inside the transparent engine model, within the symmetry plane of the cylinder ($z = 0\,\text{mm}$) Left: Contour plots of the velocity SD acquired by MRV Right: Quantitative comparison of b) velocity u and SD σ_u and c) velocity v and SD σ_v.

surements are considered ground truth. Comparison between both data sets is realized at five different locations within the central plane of the BFS channel.

The comparison of both data sets depicts excellent agreement regarding the main flow velocity u, Fig. 7.5. The measurements of the main components of the Reynolds stress tensor, σ_u and σ_v, show overall good agreement with the reference LDV data set. The magnitude of the determined SD is in accordance with the LDV data set, as well as the general trend of the plots. Some deviations are apparent: A slight underestimation of σ_u by the MR turbulence technique is visible Fig. 7.5b. In contrast to that, an overestimation of σ_v is visible, Fig. 7.5c.

Fig. 7.9 illustrates the decrease of the received signal magnitude against the amplitude of the applied "turbulence encoding" bipolar gradient. The abscissa depicts the squared applied gradient strength G. The ratio of the signal magnitude with applied gradient, S(G) to the received signal magnitude without applied gradient, S_0 is depicted on the ordinate. The dashed line at $\ln(S_0/S) \approx 0.7$ indicates a 50% decrease in signal magnitude. Two trends are illustrated, ① and ②. These trends correspond to locations identified in Fig. 7.4.

① indicates a position with moderate turbulence within the shear layer. The signal loss vs. gradient strength is illustrated with a black line in Fig. 7.9. The dashed red line is the corresponding least squares fit. The solid red line denotes the slope of the least squares fit. The trend is properly represented by the least square fit and σ_u can be calculated according to Eq. 3.23. In contrast, ② depicts the trend within a region of very high turbulence, see Fig. 7.4. The calculated slope of the least squares fit does not perfectly represent the actual trend, depicted as black line Fig. 7.9, ②, which demonstrates a higher slope over a large portion, until the slope suddenly decreases and no more decline in signal magnitude can be observed, starting from $G^2 \approx 1.2 \times 10^{-3}$. As a result the calculated SD is underestimated. This approach explains a general underestimation in σ_u within regions of high turbulence, as depicted in Fig. 7.5b at $y/h \approx 0$. However, within the same plot, also regions of low turbulence seem underestimated which cannot be explained by the observation described above.

With respect to Fig. 3.10 it is obvious, that the decay in signal magnitude is evoked by turbulence, i.e. many velocities present within one voxel. As described before, the shear layer of the BFS flow is characterized by steep

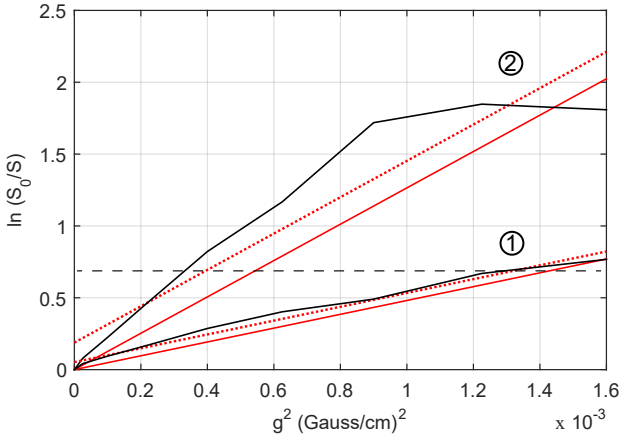

Figure 7.9: The signal drop at two distinct points inside the BFS geometry $\ln(S_0/S)$ is plotted against the squared gradient strengths. Black lines depict the MRV data and the red dotted lines the cooresponding least square fit. The dashed line at $\ln(S_0/S) \approx 0.7$ indicates a 50% signal drop.

velocity gradients. A signal loss is therefore also induced by these velocity gradients, leading to an overestimation of the calculated SD. This effect may explain the overestimation of σ_v by the MR turbulence measurement, Fig. 7.5c.

The calculated lineplots for the shear stress, τ_{uv}, depicted in Fig. 7.5d reveal larger deviations between the trend of both measurement techniques. While the magnitude of the determined shear stress lies in the same order, the trend deviates considerably and cannot be reproduced by the MR measurements. Instead, distinct peak values of τ_{uv} are identified by the MR measurements (Fig. 7.5d), $x/h = 1$, $y/h = 0.1$. The reasons for poor conformity is assumed to be located in the calculation for τ_{uv}. According to Eq. 7.3, τ_{uv} is calculated from the determined SD σ_u, σ_v and $\sigma_{\tilde{u}}$. Accordingly, the measurement uncertainties for the determination of all three SD are introduced into the calculation of the shear stress τ_{uv}. The measurement $\sigma_{\tilde{u}}$ is realized by simultaneous application of two gradients with equal gradient strength, generating a resulting gradient under the angle of $\theta = 45°$ between both applied gradients, see Fig. 7.1. A small nonuniformity of these applied gradients changes

the direction of the resulting gradient. The resulting erroneous $\sigma_{\tilde{u}}$ directly influences the calculation of τ_{uv}. It is therefore assumed that, among others, the calculation of τ_{uv} is particularly sensitive to the determination of $\sigma_{\tilde{u}}$.

MR turbulence measurements are acquired within the engine flow model, resembling a complex flow geometry with limited optical access. The measurements present contour fields of the velocity SD within the intake channel and in direct proximity of the intake valves. These measurements are, due to restricted optical access and complex geometry, hardly feasible by means of other measurement techniques. PIV validation measurements were provided. These were acquired in real engine flow within the ETB. For comparison with the MR turbulence measurements, the PIV data set first had to be normalized. This procedure was discussed and established in Chapter 5. LDV measurements for validation were additionally acquired within the cylinder chamber of the engine flow model, which was therefore equipped with the quartz-glass liner of the ETB.

The overall agreement regarding the determined flow velocities and normal stresses between the three measurement techniques is good within the acquired mid-valve plane ($z = 19\,\mathrm{mm}$). All three measurement techniques depict a very similar trend for both flow directions. A small region of deviation occurs due to contamination of the intake valve with ferromagnetic particles. This contamination results in locally isolated erroneous measurement data and was identified by a gray shaded area. The influence of the contamination is increased within the mid-cylinder plane, where a larger portion of the flow field was corrupted, resulting in larger deviations of the acquired turbulence quantities from the validation data sets.

8 Conclusions

The present study deals with the possibility of acquiring steady and unsteady flow measurements by means of Magnetic Resonance Velocimetry (MRV). MRV is an established tool for clinical diagnostics and has also found increasing consideration in the field of fluid mechanics during the last decade, where it is valued for its unique capabilities: Measurements are non-invasive and no optical access is needed. Three-dimensional flow fields and velocity components in all three spatial directions (3D3C) can be acquired without the need for tracer particles. The time for data acquisition lies in the order of minutes and no time-consuming post processing of the measurement data is required.

Natural limitations of the MRV technique exist. These limitations include the inability to acquire time-resolved measurements. MRV does not allow the direct measure of velocity fluctuations due to its underlying measurement principle. However, velocity fluctuations are a characteristic of turbulent flows that are found in most technical flows. Different approaches for the possible quantification of mean flows, unsteady periodic flows and turbulent flows are presented within this thesis.

Mean flow MRV measurements were conducted inside a 1 : 1 scale model of a modern IC engine, denoted *Engine Test Bench* (ETB). The measurements were validated with PIV flow data acquired in the ETB flow during intake stroke. To account for the different working fluids, water within the engine flow model, gas within the ETB, normalization of the flow velocities was necessary. Excellent agreement between the normalized PIV and MRV data sets was found. Mean flow measurements of the entire intake channel region provided new insights into the in-cylinder flow. The volumetric distribution of the in-cylinder flow was shown and the existence of a dominant recirculation zone in direct valve proximity was revealed. It was demonstrated that the influence of geometrical changes onto the volumetric flow distribution can conveniently be analyzed in the three-dimensional measurement domain. These measurements demonstrate the high potential of MRV for technical

flows. Flow models can be produced with arbitrary complexity, the amount of acquired data per time is unrivaled by other measurement techniques.

Nevertheless, the presented mean flow measurements only reflect one distinct flow condition within the periodic cycle of the intake stroke. To obtain a better insight of the cyclic behavior, the *unsteady, periodic flow* can be studied by using a phase-averaging MR measurement technique. This technique allows the fully volumetric acquisition of a phase-resolved, periodic flow and is denoted *4D MRV*, Elkins et al. [25] and Markl et al. [60]. 4D MRV measurements are presented in two flow models demonstrating the different possible fields of application. The engine flow model, introduced for the mean flow measurements, is modified in order to imitate the flow during intake stroke within the ETB. The flow model is equipped with periodically actuated intake valves. The frequency of the periodic motion corresponds to the Strouhal number (St) of the flow within the ETB. The volumetric flow rate is appropriately modulated. Different working fluids and the geometrical simplifications of the 4D engine model in comparison to the ETB, prevent the imitation of the entire intake stroke. Instead, a specified valid "crank angle region" within the intake stroke is identified analytically and by means of PIV validation measurements. Measurements were conducted, enabling the analysis of the in-cylinder flow during intake stroke to be resolved into 30 phase angles. The volumetric flow field was analyzed and the emergence of pronounced regions of high velocities in the overflow region was visualized. The evolution of the previously identified distinct recirculation zone in the underflow region near the valve gap was discussed. This experiment moreover represents, to the author's knowledge, the first 4D MRV measurements that include moving boundaries through forced actuation inside an MR scanner.

The second presented 4D MRV measurements observe the flow of a Kármán Vortex Street (KVS), shedding from a confined cylinder. Internal trigger generation from a temperature signal extracted within the flow was intended for these measurements. However, applied RF-pulses and magnetic field gradients during the MR measurements led to signal failure and made internal trigger generation impossible. Instead, a *hybrid trigger* generation was established: The trigger frequency is determined from the flow fluctuations in time. Just before the measurements start, the external trigger is set to the determined frequency. A 2D flow field with two velocity components were acquired, resolved into 43 phase angles. A combination of two subsequently acquired

measurements allowed the elimination of the dead time t_d, characteristic for the utilized 4D MRV measurement procedure. This enabled the analysis of the entire periodic cycle, resolved into 47 phases. The vortex growth and shedding process was demonstratively visualized. Both presented test cases illustrate the wide range of possible application for the phase-averaged measurements of unsteady, periodic flows.

Problems in the field of fluid mechanics are often dominated by turbulent flows. *MR turbulence measurements* were acquired inside a backward-facing step (BFS) geometry, in order to quantify normal and shear stresses that are used to describe turbulent flows. The measurements were compared to LDV data acquired in the same experimental setup. The experimental approach of Elkins et al. [27] was used, which is based on the working principle first described by Gao and Gore [36]. Relatively good agreement was found regarding the determination of normal stresses. Existing discrepancies between both data sets were discussed. The acquisition of shear stresses revealed existing limitations of the technique, as the agreement with the LDV validation measurements was poor. A possible explanation of these discrepancies were also provided in the discussion. The clear advantages of the MRV techniques in comparison to other measurement techniques are valid also for the MR turbulence measurements. As a demonstration of the capabilities, turbulence measurements were also acquired in the engine flow model. The measurements were quantitatively compared to LDV and PIV measurements for different locations within the cylinder chamber and relatively good agreement regarding velocities and normal sheer stresses was found. However, the MR turbulence measurements provide information about the normal stresses within the intake channel. These measurements are virtually impossible to achieve by other means.

These presented measurements prove the suitability of the MRV measurement techniques for the acquisition of both steady and unsteady flows. Turbulence measurements have just recently received increased attention and are not yet fully worked out. Despite large uncertainties that still exist regarding the quantification in general, and the quantification of shear stresses in particular, the presented measurement results demonstrate the general suitability of this technique for turbulent flows. The benefit of the MR turbulence measurement technique was demonstrated by providing contour plots of normal shear stresses within the optically inaccessible intake channel. It is expected

that the technique has significant room for improvement. The comparison of existing fluctuation frequency limits between the MR and other measurement techniques is proposed, since it enables a more precise validation.

Measurements of unsteady, periodic flows yield convincing results. Advances regarding possibilities for the generation of internal trigger signals will contribute to a further development of this technique for the analysis of unsteady, periodic flows. Mean flow measurement of steady flows can conveniently be acquired and show excellent agreement with conventional measurement techniques.

Nomenclature

Latin Letters

Symbol	SI unit	Description
A_{bulk}	m^2	bulk channel area
B	Vs/m^2	magnetic field strength
B_0	Vs/m^2	main magnetic field
B_1	Vs/m^2	radio-frequency field
$\vec{e}$	-	unit vector
$\vec{F}$	N	force
g	m/s^2	gravitational force
$\vec{G}$	$V\ s/m^3$	magnetic gradient vector
h	m	step height
I	-	quantum mechanical spin number
$\vec{J}$	Nms/rad	spin angular momentum
m	kg	mass
N	-	number of spins
N_{acq}	-	number of acquisitions
n	1/min	engine speed
r_c	m	crank radius
S	J	magnetic resonance signal
t	s	time, time step
δt	s	duration
t_{acq}	s	acquisition time
t_r, t_m	s	valve timing in real engine and model
t_r	s	acquisition time per repetition
t_T	s	total acquisition time
T	K	temperature
T_1	s	spin-lattice relaxation time
T_2	s	spin-spin relaxation time
T_2^*	s	apparent spin-spin relaxation time
u	m/s	velocity component

u_R, u_Φ	m/s	radial & angular velocity components
V	m^3	volume, integration region, control volume
V_{voxel}	m^3	voxel volume
$\dot{V}$	m^3/s	volume flow rate
x, y, z	m	coordinate

Greek letters

Symbol	SI unit	Description
α	$^\circ$	angle, flip angle
γ	rad$s$ T	gyromagnetic constant
γ_D	$-$	directional correlation coefficient
γ_{xy}	$-$	pearson's correlation coefficient
ζ	m	coordinate axis along valve stem direction
η	kg$m$ s	dynamic viscosity
η	mm	coordinate axis along valve stem direction
θ	$^\circ$	azimuth angle
λ	$^\circ$	crank angle of IC engine
ν	m^2/s	kinematic viscosity
ξ	mm	coordinate axis along valve stem direction
ρ	kg/m^3	density
σ_u,σ_v	m/s	velocity standard deviation
σ_u	N/m^2	stress tensor
τ_{ji}		
Φ	$^\circ$	magnetic resonance signal phase angle
$\Delta\Phi$	$^\circ$	phase angle difference
χ	-	magnetic susceptibility
ω	s^{-1}	angular crank angle velocity
ω_L	s^{-1}	Larmor frequency

Abbreviations

Abbreviation	Description
4D	Phase-locked, Cine or Four-dimensional
AR	Aspect Ratio of the Backward Facing Step
BFS	Backward Facing Step
CA	Crank Angle
CA	Contrast Agent
CAD	Computer-Aided Design
CFD	Computational Fluid Dynamics
CTA	Constant Temperature Anemometry
DC	Duty Cycle
ETB	Engine Test Bench
FE	Frequency Encoding
FID	Free Induction Decay
FOV	Field of View
FT	Fourier Transformation
GE	Gradient Echo
HWA	Hot Wire Anemometry
iFT	inverse Fourier Transformation
LDV	Laser Doppler Velocimetry
LpP	Lines per Phase
MHP	Multi-hole Probe
MR	Magnetic Resonance
MRI	Magnetic Resonance Imaging
MRT	Magnetic Resonance Thermometry
MRV	Magnetic Resonance Velocimetry
NF	Normalization Factor
NMR	Nuclear Magnetic Resonance
PA	Polyamide
PA	Phase angles
PC	Phase Contrast
PE	Phase Encoding
PIV	Particle Image Velocimetry
PMMA	Poly(methyl methacrylate)
PS	Phase Steps
PWM	Pulse width modulation
RF	Radio Frequency

RMS	Root Mean Square
RMSD	Root Mean Square Deviation
ROI	Region-of-Interest
SD	Standard Deviation
SE	Spin Echo
SF	Scaling Factor
SNR	Signal-to-Noise Ratio
SS	Slice Selection
TC	Thermocouple
TE	Echo Time
TR	Repetition Time
VENC	Velocity Encoding Value

List of Figures

List of Tables

Bibliography

[1] R. J. Adrian and J. Westerweel. *Particle Image Velocimetry*. Vol. 30. Cambridge Aerospace series. Cambridge and New York: Cambridge University Press, 2011, ©2011.

[2] H.-E. Albrecht, M. Borys, N. Damaschke, and C. Tropea. *Laser Doppler and Phase Doppler Measurement Techniques*. Experimental Fluid Mechanics. Berlin, Heidelberg: Springer Berlin Heidelberg, 2003.

[3] G. K. Batchelor. "Diffusion in a Field of Homogeneous Turbulence. I. Eulerian Analysis". In: *Australian Journal of Chemistry* 2.4 (1949), p. 437.

[4] E. Baum, B. Peterson, B. Böhm, and A. Dreizler. "On The Validation of LES Applied to Internal Combustion Engine Flows: Part 1: Comprehensive Experimental Database". In: *Flow, Turbulence and Combustion* 92.1-2 (2014), pp. 269–297.

[5] E. Baum, B. Peterson, C. Surmann, D. Michaelis, B. Böhm, and A. Dreizler. "Investigation of the 3D Flow Field in an IC Engine using Tomographic PIV". In: *Proceeding of the Combustion Institute* 2013.34 (2013), pp. 2903–2910.

[6] E. Baum. "Laserbasierte Untersuchung innermotorischer Prozesse". Dissertation. Darmstadt: Technische Universität Darmstadt, 2013.

[7] M. J. Benson, C. J. Elkins, P. D. Mobley, M. T. Alley, and J. K. Eaton. "Three-dimensional Concentration Field Measurements in a Mixing Layer using Magnetic Resonance Imaging". In: *Experiments in Fluids* 49.1 (2010), pp. 43–55.

[8] C. Binter, V. Knobloch, R. Manka, A. Sigfridsson, and S. Kozerke. "Bayesian Multipoint Velocity Encoding for Concurrent Flow and Turbulence Mapping". In: *Magnetic Resonance in Medicine* 69.5 (2013), pp. 1337–1345.

[9] F. Bloch. "Nuclear Induction". In: *Physical Review* 70.7 (1946), pp. 460–474.

[10] P. Boesiger, S. E. Maier, L. Kecheng, M. B. Scheidegger, and D. Meier. "Visualization and Quantification of the Human Blood Flow by Magnetic Resonance Imaging". In: *Journal of Biomechanics* 25.1 (1992), pp. 55–67.

[11] H. G. Bogren, M. H. Buonocore, and R. J. Valente. "Four-dimensional Magnetic Resonance Velocity Mapping of Blood Flow Patterns in the Aorta in Patients with Atherosclerotic Coronary Artery Disease compared to Age-matched Normal Subjects". In: *Journal of Magnetic Resonance Imaging* 19.4 (2004), pp. 417–427.

[12] G. Bretthorst. "Bayesian Analysis. I. Parameter Estimation using Quadrature NMR Models". In: *Journal of Magnetic Resonance* 88.3 (1990), pp. 533–551.

[13] H. H. Bruun. *Hot-wire anemometry: Principles and signal analysis*. Reprinted. Oxford science publications. Oxford: Oxford Univ. Press, 1996.

[14] D. J. Bryant, J. A. Payne, D. N. Firmin, and D. B. Longmore. "Measurement of Flow with NMR Imaging Using a Gradient Pulse and Phase Difference Technique". In: *Journal of Computer Assisted Tomography* 8.4 (1984), pp. 588–593.

[15] W. B. Buchenberg, F. Wassermann, S. Grundmann, B. Jung, and R. Simpson. "Acquisition of 3D Temperature Distributions in Fluid Flow using Proton Resonance Frequency Thermometry". In: *Magnetic Resonance in Medicine* 76.1 (2015), pp. 145–155.

[16] A. Caprihan and E. Fukushima. "Flow Measurements by NMR". In: *Physics Reports* 198.4 (1990), pp. 195–235.

[17] H. Y. Carr and E. M. Purcell. "Effects of Diffusion on Free Precession in Nuclear Magnetic Resonance Experiments". In: *Physical Review* 94.3 (1954), pp. 630–638.

[18] J. C. Carr and T. J. Carroll. *Magnetic Resonance Angiography: Principles and Applications*. New York: Springer Science+Business Media, LLC, 2012.

[19] F. Coletti, D. Borup, C. J. Elkins, and J. K. Eaton, eds. *Measuring Fluid, Scalar, and Particle Transport in Internal Flows Using Medical Imaging*. 2014.

[20] P. Dyverfeldt, R. Gårdhagen, A. Sigfridsson, M. Karlsson, and T. Ebbers. "On MRI Turbulence Quantification". In: *Journal of Magnetic Resonance Imaging* 27.7 (2009), pp. 913–922.

[21] P. Dyverfeldt, M. D. Hope, E. E. Tseng, and D. Saloner. “Magnetic Resonance Measurement of Turbulent Kinetic Energy for the Estimation of Irreversible Pressure Loss in Aortic Stenosis”. In: *Journal of the American College of Cardiology* 6.1 (2013), pp. 64–71.

[22] P. Dyverfeldt, J.-P. E. Kvitting, A. Sigfridsson, J. Engvall, A. F. Bolger, and T. Ebbers. “Assessment of Fluctuating Velocities in Disturbed Cardiovascular Blood Flow: In Vivo Feasibility of generalized Phase-contrast MRI”. In: *Journal of Magnetic Resonance Imaging* 28.3 (2008), pp. 655–663.

[23] P. Dyverfeldt, A. Sigfridsson, J.-P. E. Kvitting, and T. Ebbers. “Quantification of Intravoxel Velocity Standard Deviation and Turbulence Intensity by Generalizing Phase-contrast MRI”. In: *Magnetic Resonance in Medicine* 56.4 (2006), pp. 850–858.

[24] C. . Elkins, M. Markl, A. Iyengar, R. Wicker, and J. Eaton. “Full-field Velocity and Temperature Measurements using Magnetic Resonance Imaging in Turbulent Complex Internal Flows”. In: *International Journal of Heat and Fluid Flow* 25.5 (2004), pp. 702–710.

[25] C. J. Elkins, M. Markl, N. Pelc, and J. K. Eaton. “4D Magnetic Resonance Velocimetry for Mean Velocity Measurements in Complex Turbulent Flows”. In: *Experiments in Fluids* 34.4 (2003), pp. 494–503.

[26] C. J. Elkins and M. T. Alley. “Magnetic Resonance Velocimetry: Applications of Magnetic Resonance Imaging in the Measurement of Fluid Motion”. In: *Experiments in Fluids* 43.6 (2007), pp. 823–858.

[27] C. J. Elkins, M. T. Alley, L. Saetran, and J. K. Eaton. “Three-dimensional Magnetic Resonance Velocimetry Measurements of Turbulence Quantities in Complex Flow”. In: *Experiments in Fluids* 46.2 (2009), pp. 285–296.

[28] A. J. Evans, J. Avery, R. Blinder, Herfkens R.J., J. M. Robert, C. E. Spritzer, D. Kuethe, E. Fram, Evan K.M., and L. Hedlund. “Effects of Turbulence on Signal Intensity in Gradient Echo Images”. In: *Investigative Radiology* 7.23 (1988), pp. 512–518.

[29] J. Feldmann. “Experimental Approach for the Determination of the Turbulence Intensity using MR Techniques”. Master-Thesis. Darmstadt: Technische Universität Darmstadt, 2016.

[30] D. Freudenhammer, E. Baum, B. Peterson, B. Böhm, and S. Grundmann. “Magnetic Resonance Velocimetry - Capabilities for measuring IC engine intake flows”. In: *10th International ERCOFTAC Symposium on “Engineering Turbulence Modelling and Measurements”, 17-19 September, Marbella, Spain* (2014).

[31] D. Freudenhammer, E. Baum, B. Peterson, B. Böhm, and S. Grundmann. “Towards time-resolved Magnetic Resonance Velocimetry for IC-Engine Intake Flows”. In: *17th International Symposium on Applications of Laser Techniques to Fluid Mechanics, 07-10 July, Lisbon, Portugal* (2014).

[32] D. Freudenhammer, G. Rehs, W. B. Buchenberg, J. Hennig, C. Tropea, and S. Grundmann. “Phase-Averaged MRV Measurements of the von Kármán Vortex of a Confined Cylinder”. In: *18th International Symposium on Applications of Laser Techniques to Fluid Mechanics, 04-07 July, Lisbon, Portugal* (2016).

[33] D. Freudenhammer, E. Baum, B. Peterson, B. Böhm, B. Jung, and S. Grundmann. “Volumetric Intake Flow Measurements of an IC Engine using Magnetic Resonance Velocimetry”. In: *Experiments in Fluids* 55.5 (2014).

[34] D. Freudenhammer, B. Peterson, C.-P. Ding, B. Boehm, and S. Grundmann. “The Influence of Cylinder Head Geometry Variations on the Volumetric Intake Flow Captured by Magnetic Resonance Velocimetry”. In: *SAE International Journal of Engines* 8.4 (2015).

[35] E. Fukushima. “Nuclear Magnetic Resonance as as Tool to study Flow”. In: *Annual Review of Fluid Mechanics* 31.1 (1999), pp. 95–123.

[36] J.-H. Gao and J. C. Gore. “Turbulent Flow Effects on NMR Imaging: Measurement of Turbulent Intensity”. In: *Medical Physics* 18.5 (1991), pp. 1045–1051.

[37] J.-H. Gao and H.-L. Liu. “Inflow Effects on Functional MRI”. In: *NeuroImage* 62.2 (2012), pp. 1035–1039.

[38] L. F. Gladden and A. J. Sederman. “Recent Advances in Flow MRI”. In: *Journal of Magnetic Resonance* 229 (2013), pp. 2–11.

[39] D. Gross, W. Hauger, and J. Schröder. *Technische Mechanik 2: Elastostatik*. 12., aktualisierte Aufl. 2014. Springer-Lehrbuch. Berlin Heidelberg: Springer Berlin Heidelberg, 2014.

[40] M. Haacke, R. Brown, M. Thompson, and R. Venkatesan. *Magnetic Resonance Imaging*. New York, 1999.

[41] E. L. Hahn. “Detection of Sea-Water Motion by Nuclear Precession”. In: *Journal of Geophysical Research* 2.65 (1960), pp. 776–777.

[42] L. G. Hanson. “A Graphical Simulator for Teaching Basic and Advanced MR Imaging Techniques”. In: *Radiographics : a review publication of the Radiological Society of North America, Inc* 27.6 (2007), e27.

[43] L. G. Hanson. “Is Quantum Mechanics Necessary for Understanding Magnetic Resonance?” In: *Concepts in Magnetic Resonance Part A* 32A.5 (2008), pp. 329–340.

[44] A. Hendrix. *Magnets, Spins, and Resonances: An Introduction to the Basics of Magnetic Resonance*. Erlangen, 2003.

[45] J. Hennig, M. Müri, P. Brunner, and H. Friedburg. “Quantitative Flow Measurement with the Fast Fourier Flow Technique”. In: *Radiology* 166.1 (1988), pp. 237–240.

[46] J. B. Heywood. *Internal Combustion Engine Fundamentals*. New York, 1988.

[47] T. Igarashi. “Flow Resistance and Strouhal Number of a Vortex Shedder in a Circular Pipe”. In: *JSME International Journal Series B* 42.4 (1999), pp. 586–595.

[48] K. M. Johnson and M. Markl. “Improved SNR in Phase Contrast Velocimetry with Five-point Balanced Flow Encoding”. In: *Magnetic Resonance in Medicine* 63.2 (2010), pp. 349–355.

[49] A. A. Joseph, K.-D. Merboldt, D. Voit, S. Zhang, M. Uecker, J. Lotz, and J. Frahm. “Real-time Phase-contrast MRI of Cardiovascular Blood Flow using Undersampled Radial Fast Low-angle Shot and Nonlinear Inverse Reconstruction”. In: *NMR in biomedicine* 25.7 (2012), pp. 917–924.

[50] L. Jou. “Magnetic Resonance Signal Loss in Turbulent Shear Flow”. In: *Biomedical Engineering: Applications, Basis and Communications* 14.01 (2002), pp. 1–11.

[51] B. Jung and M. Markl. *Magnetic Resonance Angiography: Principles and Applications. Phase Contrast MRI and Flow Quantification*. 2010.

[52] D. O. Kuethe and J.-H. Gao. “NMR Signal Loss from Turbulence: Models of Time Dependence Compared with Data”. In: *Physical Review E* 51.4 (1995), pp. 3252–3262.

[53] J.-P. E. Kvitting, T. Ebbers, L. Wigstrom, J. Engvall, C. L. Olin, and A. F. Bolger. “Flow Patterns in the Aortic Root and the Aorta studied with Time-Resolved, 3-dimensional, Phase-Contrast Magnetic Resonance Imaging: Implications for Aortic Valve-Sparing Surgery”. In: *The Journal of thoracic and cardiovascular surgery* 127.6 (2004), pp. 1602–1607.

[54] P. C. Lauterbur. “Image Formation by Induced Local Interactions: Examples Employing Nuclear Magnetic Resonance”. In: *Nature* 242 (1973), pp. 190–191.

[55] A. T. Lee, G. Bruce Pike, and N. J. Pelc. “Three-Point Phase-Contrast Velocity Measurements with Increased Velocity-to-Noise Ratio”. In: *Magnetic Resonance in Medicine* 33.1 (1995), pp. 122–126.

[56] M. Markl. “Techniques in the Assessment of Cardiovascular Blood Flow and Velocity”. In: *Cardiovascular Magnetic Resonance Imaging*. Ed. by R. Y. Kwong. Contemporary Cardiology. Totowa, NJ: Humana Press Inc, 2008, pp. 195–210.

[57] M. Markl, M. T. Draney, M. D. Hope, J. M. Levin, F. P. Chan, M. T. Alley, N. J. Pelc, and Herfkens R.J. “Time-Resolved 3-Dimensional Velocity Mapping in the Thoracic Aorta: Visualization of 3-Directional Blood Flow Patterns in Healthy Volunteers and Patients”. In: *Journal of Computer Assisted Tomography* 28.4 (2004), pp. 459–468.

[58] M. Markl, F. P. Chan, M. T. Alley, K. L. Wedding, M. T. Draney, C. J. Elkins, D. W. Parker, R. Wicker, C. A. Taylor, R. J. Herfkens, and N. J. Pelc. “Time-Resolved Three-dimensional Phase-Contrast MRI”. In: *Journal of Magnetic Resonance Imaging* 17.4 (2003), pp. 499–506.

[59] M. Markl, A. Harloff, T. A. Bley, M. Zaitsev, B. Jung, E. Weigang, M. Langer, J. Hennig, and A. Frydrychowicz. “Time-resolved 3D MR velocity Mapping at 3T: Improved navigator-gated Assessment of vascular Anatomy and Blood Flow”. In: *Journal of Magnetic Resonance Imaging* 25.4 (2007), pp. 824–831.

[60] M. Markl, P. J. Kilner, and T. Ebbers. “Comprehensive 4D Velocity Mapping of the Heart and great Vessels by Cardiovascular Magnetic Resonance”. In: *Journal of Cardiovascular Magnetic Resonance* 13.1 (2011), p. 7.

[61] McRobbie D.W., Moore E.A., Graves M.J., and M. R. Prince. *MRI From Picture to Proton, Second edition*. Cambridge, 2006.

[62] D. Michaelis, C. Poelma, F. Scarano, J. Westerweel, and B. Wieneke. *A 3D Time-Resolved Cylinder Wake Survey by Tomographic PIV*. Ed. by 12th Int. Symp. on Flow Visualization. 2006.

[63] P. R. Moran, R. A. Moran, and N. Karstaedt. "Verification and Evaluation of Internal Flow and Motion. True Magnetic Resonance Imaging by the Phase Gradient Modulation Method". In: *Radiology* 154.2 (1985), pp. 433–441.

[64] B. Newling, C. C. Poirier, Y. Zhi, J. A. Rioux, A. J. Coristine, D. Roach, and B. J. Balcom. "Velocity Imaging of Highly Turbulent Gas Flow". In: *Physical review letters* 93.15 (2004), p. 154503.

[65] W. Nitsche and A. Brunn. *Strömungsmesstechnik*. 2., aktualisierte und bearbeitete Aufl. VDI-Buch. Berlin, Heidelberg: Springer-Verlag Berlin Heidelberg, 2006.

[66] N. J. Pelc, M. A. Bernstein, A. Shimakawa, and Glover G.H. "Encoding Strategies for Three-direction Phase-Contrast MR Imaging of Flow". In: *Journal of Magnetic Resonance Imaging* 1.4 (1991), pp. 405–413.

[67] N. J. Pelc, Sommer F.G., Li K.C., Brosnan T.J., Herfkens R.J., and D. R. Enzmann. "Quantitative Magnetic Resonance Flow Imaging". In: *Magnetic Resonance Quarterly* 10.3 (1994), pp. 125–147.

[68] B. H. Peng, J. J. Miau, F. Bao, L. D. Weng, C. C. Chao, and C. C. Hsu. "Performance of Vortex Shedding from a Circular Cylinder with a Slit Normal to the Stream". In: *Flow Measurement and Instrumentation* 25 (2012), pp. 54–62.

[69] M. Piro, F. Wassermann, S. Grundmann, B. W. Leitch, and C. Tropea. "Progress in on-going Experimental and Computational Fluid Dynamic Investigations within a CANDU Fuel Channel". In: *Nuclear Engineering and Design* 299.1 (2015), pp. 184–200.

[70] K. P. Pruessmann, M. Weiger, M. B. Scheidegger, and P. Boesiger. "SENSE: Sensitivity Encoding for Fast MRI". In: *Magnetic Resonance in Medicine* 42.5 (1999), pp. 952–962.

[71] E. M. Purcell, H. C. Torrey, and R. V. Pound. "Resonance Absorption by Nuclear Magnetic Moments in a Solid". In: *Physical Review* 69.1-2 (1946), pp. 37–38.

[72] M. Raffel, C. E. Willert, and J. Kompenhans. *Particle Image Velocimetry: A practical guide*. Experimental Fluid Mechanics. Berlin and New York: Springer, 1998.

[73] L. de Rochefort, L. Vial, R. Fodil, X. Maitre, B. Louis, D. Isabey, G. Caillibotte, M. Thiriet, J. Bittoun, E. Durand, and G. Sbirlea-Apiou. "In Vitro Validation of Computational Fluid Dynamic Simulation in Human Proximal Airways with Hyperpolarized 3He Magnetic Resonance Phase-Contrast Velocimetry". In: *Journal of Applied Physiology* 102.5 (2007), pp. 2012–2023.

[74] J. F. Schenck. "The Role of Magnetic Susceptibility in Magnetic Resonance Imaging: MRI Magnetic Compatibility of the First and Second Kinds". In: *Medical physics* 23.6 (1996), pp. 815–850.

[75] S. L. Sclove. *A Course on Statistics for Finance*. Boca Raton, Fla and London: CRC Press, 2013.

[76] J. H. Steiger. "Tests for Comparing Elements of a Correlation Matrix". In: *Psychological Bulletin* 87.2 (1980), pp. 245–251.

[77] S. N. Urchuk and D. B. Plewes. "Mechanisms of Flow-Induced Signal Loss in MR Angiography". In: *Journal of Magnetic Resonance Imaging* 2.4 (1992), pp. 453–462.

[78] Y. Wang, R. C. Grimm, P. J. Rossman, J. P. Debbins, S. J. Riederer, and R. L. Ehman. "3D Coronary MR Angiography in Multiple Breath-holds Using a Respiratory Feedback Monitor". In: *Magnetic Resonance in Medicine* 34.1 (1995), pp. 11–16.

[79] Y. Wang, T. M. Grist, F. R. Korosec, P. S. Christy, M. T. Alley, J. A. Polzin, and C. A. Mistretta. "Respiratory Blur in 3D Coronary MR Imaging". In: *Magnetic Resonance in Medicine* 33.4 (1995), pp. 541–548.

[80] F. Wassermann. "Magnetic Resonance Imaging Techniques for Thermofluid Applications". Dissertation. Darmstadt: Technische Universität Darmstadt, 2015.

[81] F. Wassermann, D. Hecker, B. Jung, M. Markl, A. Seifert, and S. Grundmann. "Phase-locked 3D3C-MRV Measurements in a Bi-stable Fluidic Oscillator". In: *Experiments in Fluids* 54.3 (2013).

[82] D. Weishaupt, V. D. Köchli, and B. Marincek. *Wie funktioniert MRI? Eine Einführung in Physik und Funktionsweise der Magnetresonanzbildgebung ; mit 9 Tabellen*. 6. Aufl. Heidelberg: Springer, 2009.

[83] A. L. Wentland, O. Wieben, F. R. Korosec, and V. M. Haughton. "Accuracy and Reproducibility of Phase-Contrast MR Imaging Measurements for CSF Flow". In: *American Journal of Neuroradiology* 31.7 (2010), pp. 1331–1336.

[84] L. Wigström, L. Sjöqvist, and B. Wranne. “Temporally Resolved 3D Phase-Contrast Imaging”. In: *Magnetic Resonance in Medicine* 36.5 (1996), pp. 800–803.

[85] C. Williamson and G. Brown. “A series in $1/\sqrt{\text{Re}}$ to represent the Strouhal-Reynolds Number Relationship of the Cylinder Wake”. In: *Journal of Fluids and Structures* 12.8 (1998), pp. 1073–1085.

[86] D. Xing, S. J. Gibbs, J. A. Derbyshire, E. J. Fordham, T. A. Carpenter, and L. D. Hall. “Bayesian Analysis for Quantitative NMR Flow and Diffusion Imaging”. In: *Journal of Magnetic Resonance, Series B* 106.1 (1995), pp. 1–9.

[87] M. M. Zdravkovich. *Flow around Circular Cylinders: A comprehensive Guide through Flow Phenomena, Experiments, Applications, Mathematical Models, and Computer Simulations*. Repr. Oxford science publications. Oxford: Oxford Univ. Press, 2007.